Alpha-decay Spectroscopy and Beta-delayed Fission of Neutron Deficient Isotopes ^{194,196}At

Victoria Louise Truesdale

Doctor of Philosophy

University of York
Physics

September 2015

Abstract

A detailed nuclear-decay spectroscopy and the β-delayed fission of the neutron deficient isotopes ^{194,196}At are presented in this work. An isotopic beam was produced using the selective Resonance Ionization Laser Ion Source (RILIS) and ISOLDE mass separator (CERN). The fine-structure α decay of ^{196}At allowed the low-energy excited states in the daughter nucleus ^{192}Bi to be investigated with new states being discovered. The β-decay branch was also derived with a value of $b_\beta(^{196}\text{At}) = 2.6(1)$ %. Further to this, the half-lives of ^{196}At and ^{196}Po were deduced, with values of 0.358(5) ms and 5.8(1) s respectively. Additionally, multipolarities were assigned to some of the γ transitions that were observed in ^{192}Bi. A preliminary α-decay study of ^{194}At was also carried out.

A β-delayed fission study of ^{196}At, and a preliminary βDF study of ^{194}At were also performed. A mixture of symmetric and asymmetric fission fragments of mass distributions of the daughter isotope ^{196}Po (populated by β decay of ^{196}At) were deduced, based on the measured fission fragment energies. A βDF probability $P_{\beta DF}(^{196}\text{At}) = 9(1)\times10^{-5}$ was determined.

Contents

List of Figures

List of Tables

Acknowledgements

I would firstly like to thank my supervisor, Prof. Andrei Andreyev for his help and guidance over the past four years. I would also like to thank him for the travel opportunities made available for both experiments and conferences.

I would also like to thank Lars Ghys at KU Leuven for his help in explaining how certain parts of the analysis code worked. I would also like to thank the collaboration at KU Leuven who provide the detector system that is used in the experimental work (and for keeping it working).

A big thank you needs to go to my fellow students at York, both past and present. You all helped make my move to York much easier and made me feel part of the group. To all those who were at the Bristol summer school, never mind the Gromits, I found all 120 Shaun the Sheep that were in London and Bristol!

I should also say thank you to my team leader at work Donna Moor (and current acting team leader) Dr Stephen Smith for being very understanding about my thesis and allowing me to work flexibly so that I was able to get the time I needed to finish it (I will make up the hours I promise).

To those at UWS, I had an enjoyable year while there. Special thanks must go to Valentina whose code I inherited and was able to reply to my queries, especially the "I broke the code again" one.

A mention goes to the officials for hockey at the Commonwealth Games who put up with me typing and working away in the officials lounge (and also doing some proof reading for me - Iain McKay).

Finally, I would like to thank my parents, Richard and Catherine, who have not only supported me throughout this PhD, but also through the numerous degrees that went before it. All I can say is that I am no longer a perpetual student and have a job!

Author Declaration

This thesis has been submitted for the degree of Doctor of Philosophy in accordance with the regulations of the University of York.

The experimental work was performed at ISOLDE, CERN in collaboration with KU Leuven. The work (including other nuclides) that examined β-delayed fission in greater detail was studied by L. Ghys of KU Leuven. The work was published in,

- L. Ghys *et al.* , Evolution of fission-fragment mass distributions in the neutron-deficient lead region, Phys. Rev. C 041301, 2014

in which the author of this thesis is also a co-author. All results presented in this thesis have been carried out independently of the work presented in that paper. The work in this thesis will soon be submitted for publication,

- V. L. Truesdale *et al.*, β-delayed fission and α decay of ^{196}At, *In preparation* (2015)

This work has not previously been presented for an award at this, or any other, University.

I therefore declare that the work here is my own, and where other sources of information have been used, they are clearly marked and referenced.

Chapter 1

Introduction

The work in this thesis focusses on the astatine isotopes ^{194,196}At, indicated by the red squares in Figure 1.1. These nuclei are situated close to the proton drip line and lie ∼18 neutrons away from the β stability line. Specifically, it will investigate their decay properties, in particular, α decay and the rare decay process of beta-delayed fission (βDF). The astatine nuclei for the experiments were produced artificially at the ISOLDE facility in CERN.

Astatine is one of the rarest elements on Earth and has no stable isotopes. The rarity of this element is reflected in its Greek name '$\alpha\sigma\tau\alpha\tau o\zeta$' (astatos), which means unstable. There is a small amount of astatine present naturally on Earth, but this is primarily from the decay of radioactive elements in the Earth's crust [1]. The element astatine was first discovered in 1940, using the bombardment of a bismuth target with alpha particles produced in the Crocker Radiation Laboratory which was situated in Berkeley at the time [2] (it is now in UC Davis [3]).

1.1 Physics Background

1.1.1 α Decay

Alpha radiation was first discovered in 1899 by Rutherford [5] and shown to be the emission of doubly-charged helium. Along with Rutherford, it was also investigated by Geiger and Nuttall and in a quantum mechanical formulation by Gamow and, Guerney and Condon in 1928 [6] The α-decay systematics for the Z = 82 region have been previously explored in a paper by Andreyev *et al.* [7]. Further details on α decay are discussed in Section 2.4.

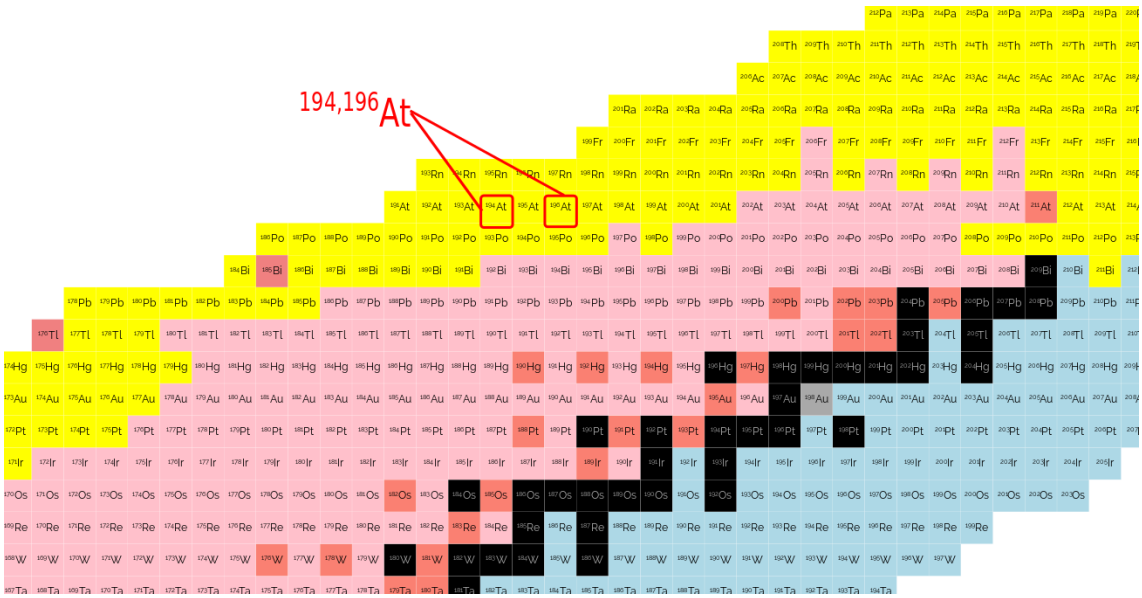

Figure 1.1: Nuclei of interest highlighted in red on the chart of the nuclides. Stable nuclei are shown in black. The nuclei decaying predominantly by α decay are shown in yellow, those by β^+/EC in pink and those by β^- in blue. Adapted from [4].

1.1.2 Fission

Seventy-seven years ago, Hahn and Strassmann published their paper "Über den Nachweis und das Verhalten der bei der Bestrahlung des Urans mittels Neutronen entstehenden Erdalkalimetalle" [8], in English "Concerning the Existence of Alkaline Earth Metals Resulting from Neutron Irradiation of Uranium"[9]. This paper presents the discovery of fission. The name fission however was not coined by Hahn and Strassmann, but by Meitner and Frisch, who used the phrase in their paper "Disintegration of Uranium by Neutrons: a New Type of Nuclear Reaction" [10]. It is in this paper by Meitner and Frisch that the first understanding of the fission process was put forward, with the authors comparing it to a liquid drop and as such "If the movement is made sufficiently violent by adding energy, such a drop may divide itself into two smaller drops."[10]. The discovery of fission however, could have been made anytime between 1934 and its actual discovery, were it not for errors made by various groups of scientists and the belief that it was impossible to split heavy nuclei into lighter fragments [11]. In 1934, when the first experiments were made in Rome by Fermi and his group, an article appeared by Ida Noddack, "Über das Element 93", [12] in which she questioned Fermi's discovery of element 93 [13]. In her paper, she says that Fermi should "have compared his new radioelement with all known

elements." (english translation [14]) and therefore exclude all other possible nuclei. Noddack then continues in her paper to say that it is possible that a "distinctly new nuclear reaction" could have taken place that had not been observed and if heavy nuclei are bombarded by neutrons then it is possible that "the nucleus breaks up into several large fragments"[12, 14]. The process of fission is being described, but although the various groups were likely to have seen it, at the time it was not thought possible that a nucleus could behave in this manner. The partnership of Curie and Savitch could have been the first to discover fission in 1938, if they had correctly identified the 3.5 hour half-life activity as lanthanum instead of originally as an isotope of actinium. Possibly, due to contaminants, they were not able to identify it as lanthanum, even though it exhibited all the correct properties [15].

Since then, different types of fission have been identified. These are particle-induced fission discovered in 1939 [8], spontaneous fission in 1941 by Pertzhak *et al.* [16], spontaneously fissioning isomers by Polikanov *et al.* in 1962 [17], beta-delayed fission (βDF) by Kuznetsov *et al.* [18, 19], Coulomb excitation/Coulex fission in 2000 by Schmidt *et al.* [20, 21], photofission see e.g. Csige *et al.* [22] and a surrogate type of fission, see review by Escher *et al.* [23].

1.2 Motivations

Generally, most experimental information about the mechanism of nuclear fission can be discovered at low excitation energies. This is because in low-energy fission the interactions between macroscopic and microscopic effects can be studied, in contrast to high energy fission where the microscopic effects are washed out [24]. Previously, low-energy fission was studied by spontaneous fission of the nuclides for which this is possible (limited to heavy actinides and transactinides), and through particle induced fission with thermal neutrons and light projectiles such as protons, deuterons and α particles. These methods only accessed a limited number of nuclei, mainly those beside the valley of β-stability from thorium to rutherfordium and above [24]. Through the use of Coulex-induced fission using relativistic radioactive beams, the area of nuclei studied could be extended to the very neutron-deficient isotopes of At-Rn [20, 21].

Beta-delayed fission is a two-step process in which the parent β decays followed by the fission of the excited daughter nuclide. It is important in the study of low-energy fission ($E^* \sim B_f$) as it allows access to fission data for exotic nuclei that otherwise do not fission from their ground state. By the end of the 1990's less than

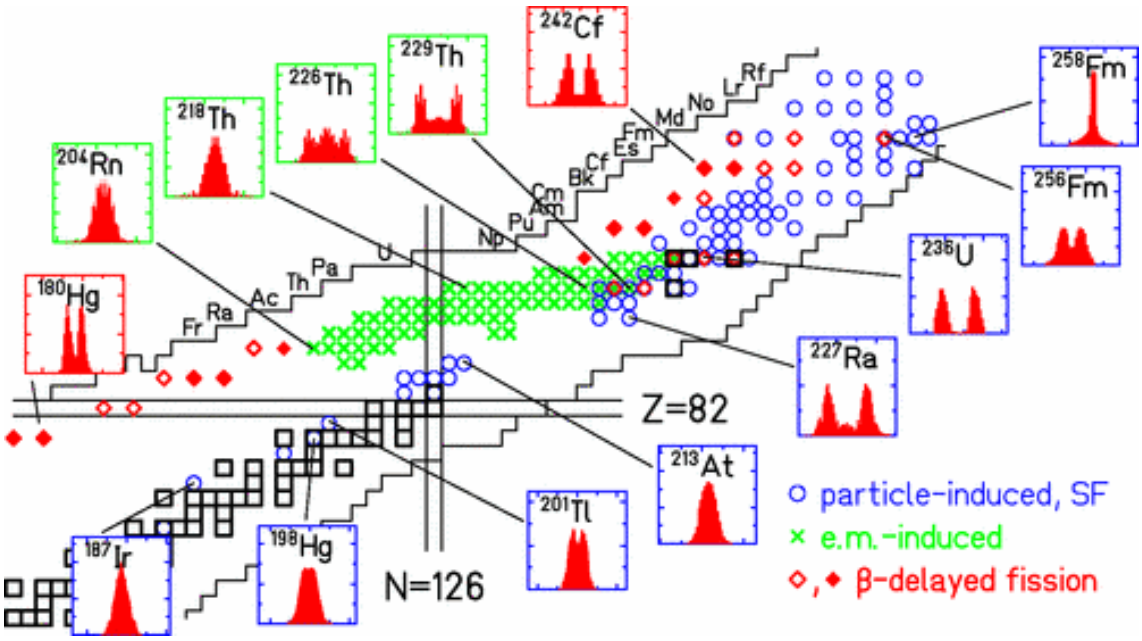

Figure 1.2: Mass distributions of selected nuclei in different regions of low-energy fission. The diamonds in particular relate to βDF with the filled diamonds representing cases where the mass distribution has been measured [24].

20 cases of βDF had been found, all of them in the heavy actinides. Reviews of the data found in these cases have previously been done by Hall and Hoffman [25] in 1992 and by Kuznetsov and Skobelev [26]. In his paper from 1987, Lazarev *et al.* [27] note that the conditions for βDF to occur can be found in the preactinide region, in particular for the neutron-deficient nuclei from Tl to Bi. In this paper he took the example of ^{180}Tl as being a potential candidate for βDF. Experimental data were then obtained (this has been further studied in references [28, 29, 30]) and from the analysis in the paper, it was concluded that some of the odd-odd nuclei in the region of ^{180}Tl to ^{196}At would be likely to decay by βDF. Further motivations are discussed in the following section, the fission fragment mass distributions and relevance to the r-process in astrophysics.

Although βDF is one of the main goals of this work, data on the α-decay properties of ^{194,196}At were also obtained. α decay is the dominant mode of decay for these nuclei and as such the properties of the α decay were investigated.

1.2.1 Mass Distributions

An area of fission studies of particular interest is the mass distribution of the fission fragments (FFs). The calculated mass distributions (MDs) for a selection of nuclides which decay by low-energy fission in the region of interest are shown in Fig. 1.2. It is only by studying low-energy fission, and therefore the microscopic effects, that it is possible to explain asymmetric mass distributions [30]. The plot shown in Fig. 1.2 can be split into two main areas, the transuranium and the lead regions, the former demonstrating mostly the asymmetric mass split (e.g. uranium isotopes) while the latter predominantly symmetric, especially in the vicinity of ^{208}Pb.

Predictions of the fission fragment mass distributions expected in the lead region used in the analysis of the βDF of ^{180}Tl were taken from the five dimensional (5D) macroscopic-microscopic model by Möller *et al.* [31], see Fig. 1.3. In this case, as will be seen in Section 2.6.2, the experimentally obtained asymmetric mass distribution was not expected before the experiment, but in the latter analysis was found to be explained by all theories. After the publication by Andreyev *et al.* [30], a follow up theoretical study was published by Ichikawa *et al.* [32]. This study compared the potential energy surfaces (PES) of ^{180}Hg against ^{236}U. Since ^{180}Hg fissions asymmetrically, which is in agreement with the calculations, and nuclei which are found in the ^{208}Rn region fission symmetrically, see Fig. 1.3, it is therefore of interest to study the nuclei that lie between these nuclei. In this study, the nuclei investigated were ^{194,196}At.

1.2.2 Nuclear Astrophysics

The work in this thesis concentrates on the proton-rich portion of the Segre Chart. If attention is turned to the neutron-rich nuclei of the chart, then the process of βDF is expected to have an impact on the astrophysical r-process. In the r-process, heavier nuclei are formed through successive neutron captures and β decays. βDF affects this by creating fission recycling, which changes the distribution of elements of the r-process path, or even terminating it [34]. This means that not only can it influence the abundances of nuclei which are in the region of A $\sim$ 90 - 130, but by also terminating the r-process, it can affect the production of the super-heavy elements [35].

The degree to which βDF influences the r-process is important if the age of the Galaxy is to be calculated using actinide chronometers. A method to calculate the age of the Galaxy is to use the production ratio of r-process nuclides, especially of

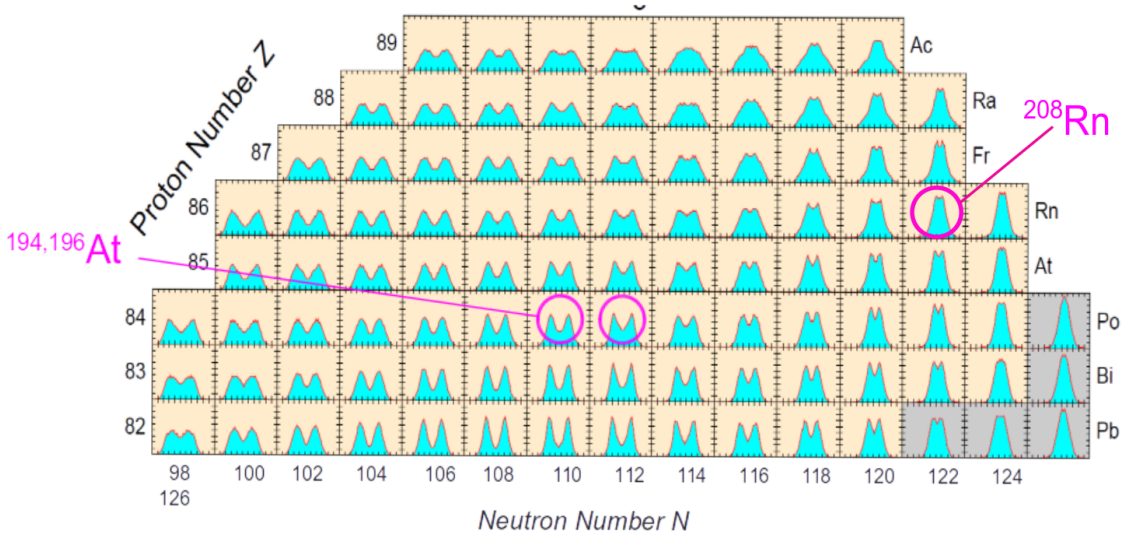

Figure 1.3: The predicted fission fragment mass distributions for the region of interest taken from [33]. The particular nuclei studied are marked on the plot. Although the nuclei are marked as ^{194,196}At the MD shown relates to the fission of the daughter nuclide, ^{194,196}Po which are produced via the β decay of the precursors.

the long-lived trans-bismuth nuclei, and compare them with the observed ratio at the time the Solar System formed. This gives the nucleosynthesis duration, which in turn can be used to calculate the age of the Galaxy. To produce an accurate answer for the age of the Galaxy, reliable information is required on how βDF affects the r-process [34]. By improving understanding of the mechanism of βDF, this knowledge can be applied to models, which in turn, can be used to improve understanding of the r-process.

1.3 Previous Studies of ^{194,196}At

1.3.1 Previous studies of ^{194}At

^{194}At was first seen by S. Yashita using the SASSY gas-filled magnetic separator at California University Berkeley [36]. The results from Yashita's 1984 PhD thesis gave the α-decay energy as 7.20(2) MeV and a half-life value of 180(80) ms [36]. In 1995, Leino *et. al* [37], performed experiments at the gas-filled separator RITU, JYFL, University of Jyväsklä, Finland, where they proposed the existence of two isomers. The α-decay energies of these isomers were 7.14 MeV and 7.19 MeV, with half-lives of 40 ms and 250 ms respectively. The most recent paper is by Andreyev *et al.* [38]

from an experiment carried out at SHIP in GSI (Darmstadt, Germany). Using the reaction ^{141}Pr(^{56}Fe,3n)^{194}At, two isomers were seen with the most intense α-decay energies for each being 7178(15) keV and 7190(15) keV. The half-lives of the parent states of these α decays are 310(8) ms and 253(10) ms respectively. The recent paper by Nyman *et. al* [39], describes an experiment in which ^{194,196}At were produced in the 2n and 4n evaporation channels of the ^{51}V + ^{147}Sm reaction, respectively. They saw a low and high spin component for ^{194}At also. The energies and half-lives that they deduced were 7174(8) keV and 240^{+40}_{-30} ms for the low spin isomer, and 7156(5) keV and 300^{+50}_{-40} ms for the high spin isomer.

There has only been one published paper on the βDF of ^{194}At, which was in 2009 by Andreyev *et. al* [40]. The data originated from the same study at SHIP (GSI) as for the α decay.

1.3.2 Previous studies of ^{196}At

Previous studies mainly used complete fusion reactions with heavy ions to produce the ^{196}At nuclei. The first identification of ^{196}At was made by Treytl *et al.*, in 1967 using the Heavy Ion Linear Accelerator at Berkeley [41]. The reactions used by this group were ^{185}Re(^{20}Ne,xn)$^{205-x}$At and ^{187}Re(^{20}Ne,xn)$^{207-x}$At. The reaction products that recoiled from the thin target were thermalised in helium gas and collected on a silver foil. This foil was then placed in front of a Si(Au) surface barrier detector. They detected a single α decay with an energy of E_α = 7055(7) keV with a total number of counts for ^{196}At of 60×10^3. A study by Morita *et al.* [42], at RIKEN (Tokyo, Japan) used the gas-filled recoil separator GARIS and a position sensitive silicon detector. The energy found was reported to be 7053(30) keV, with a half-life of 320^{+220}_{-90} ms. The statistics for their experiment however, are low with only six position and time correlated events being observed. Enqvist *et al.* [43] carried out a study using the RITU gas-filled separator, and the complete-fusion reaction ^{170}Yb(^{35}Cl,xn)$^{205-x}$Fr. The ^{196}At was produced as a daughter of ^{200}Fr, its α-decay energy and half-life values were determined as 7044(7) keV and 390^{+270}_{-120} ms, respectively. At RIKEN using GARIS, Pu *et al.* [44] in a continuation of the experiment by Morita *et al.* [42], ^{196}At was also produced via the pxn channel. They found an energy for ^{196}At of 7065(30) keV and a half-life of 253(9) ms. An experiment by Smith *et al.*, [45] was carried out by using the recoil decay tagging (RDT) technique and the RITU gas-filled separator. They determined the energy of the ^{196}At peak to be 7048(5) keV with a total number $60(1)\times10^3$ α decays. The

half-life value that they measured was 0.388(7) s. The study of ^{196}At by De Witte *et al.* [46] at ISOLDE (CERN, Geneva) , reported an α-decay energy of 7055(12) keV, with a half-life of 389(54) ms. A more recent study at RITU by Uusitalo *et al.* [47], also reported seeing ^{196}At in the fusion-evaporation reaction ^{141}Pr(^{60}Ni,xn)$^{201-x}$Fr with an α-decay energy of 7048(12) keV and a half-life of 350^{+290}_{-110} ms. The recently published paper by Nyman *et al.*,[39] (mentioned above), gives an α-decay energy of 7047(5) keV and a half-life of 350^{+50}_{-40} ms. A paper published by Kalaninová *et al.* [48] reported two α decays of ^{196}At with α-decay energies of 7045(5) keV and 6732(8) keV. A half-life of 350(90) ms was deduced for the much stronger 7045(5) keV α decay.

The first βDF study of ^{196}At was performed by Lazarev *et al.* [49] in 1987. He used a fusion-evaporation reaction ^{159}Tb(^{40}Ca, 3n)^{196}At and mica detectors. The use of mica foil detectors did not allow the measurements of α decay. However, they did see 148 fission events with a half-life of $0.23^{+0.05}_{-0.03}$ s.

1.4 Thesis Outline

In this present thesis, the data obtained for ^{194,196}At from two experiments, in 2011 and 2012 are discussed. The theory relating to the work carried out in this thesis is explained in Chapter 2. Here, the relevant models and information pertinent to the processes studied in this work are discussed. In Chapter 3 a detailed overview is given of the experimental techniques and methods used. Also included in this chapter is information about the detectors that were utilised. The analysis techniques that were used to deal with the different data sets is given in Chapter 4 and Chapter 5. The analysis techniques that were used for the 2011 data set and in particular the α-decay analysis, are detailed in Chapter 4. The 2012 data set with the fission analysis is in Chapter 5. Following these Chapters, is Chapter 6 the first of the results Chapters. Contained within this Chapter are all the results pertaining to the α decay ^{196}At and its related daughters. Chapter 7 examines the βDF of ^{196}At. Chapter 8 is a preliminary analysis and results Chapter for the α decay ^{194}At data that were collected during the 2011 and 2012 experimental runs, while Chapter 9 is the βDF results. The thesis then finishes with Chapter 10, the conclusions drawn from the work.

Chapter 2

Theory

2.1 Liquid Drop Model (LDM)

The idea of comparing a nucleus to a liquid drop was first proposed by Gamow in 1929 [50]. The formation of this idea into a model, however, lies in the semi-empirical mass formula developed by von Weizsäcker [51] in 1935 and Bethe and Bacher in 1936 [52]. It was further developed by Bohr and Wheeler in relation to fission in 1939 [53]. The liquid drop model is also an example of a macroscopic model.

By assuming that the nucleus can be compared to a liquid drop, then this analogy can be used to calculate the binding energy of a nucleus. This was realised by Weizsäcker and defined in what is known as the semi-empirical mass formula. The form of this formula is [54]:

$$M(Z,A) = Zm_p + Nm_n - B(Z,A)/c^2 \tag{2.1}$$

, where M, Z, A are the mass, atomic number, mass number respectively, m_p is the mass of a proton, m_n is the mass of a neutron, B is the binding energy and c is the speed of light. The last term, the binding energy can further be defined as:

$$B = a_v A - a_s A^{\frac{2}{3}} - a_c \frac{Z^2}{A^{\frac{1}{3}}} - a_A \frac{(A-2Z)^2}{A} + \delta \tag{2.2}$$

, where $a_v = 15.85$ MeV, $a_s = 18.34$ MeV, $a_c = 0.71$ MeV and $a_A = 23.21$ MeV [55]. These parameters are in fact adjusted to a fit of known properties of some masses of nuclei. The first three terms in Equation 2.1 are the volume, surface and Coulomb contributions, respectively. These contributions represent those that would be required to calculate the energy of a charged liquid drop. The volume term

depends linearly on the mass of the nucleus. This is due to nucleons only interacting with several nearest neighbour nuclei because of the short range of the nuclear force. This makes the binding energy per nucleon constant, and therefore, proportional to the volume, see Fig. 2.1. However, nucleons which are situated at the surface of a nucleus will experience a lower binding energy as they will not be surrounded by nucleons, unlike those away from the surface. The surface term is therefore proportional to the surface area of the nucleus, or liquid drop. The Coulomb term needs to be considered due to the electrostatic force, acting repulsively, between protons [6]. Although the use of Equation 2.1 treats the nucleus as a liquid drop, the final two terms are added to account for the specific number of protons and neutrons in the nucleus. The fourth term, the symmetry term, comes from the Pauli principle, whereby it prevents the occupation of an orbital by two identical particles with identical spins. If nucleons could occupy any of the orbitals, then the maximum binding energy would be when they occupied the lowest orbitals possible. Energetically, if only this term were considered, then the symmetric distribution of $Z = N = A/2$ would be favoured. The final term is the pairing term. Nucleons tend to form pairs, with zero spin. The δ term is therefore positive if the nucleus is even-even since all the nucleons will be coupled, negative if the nucleus is odd-odd and 0 if it is odd-even [55].

Although the liquid drop model is macroscopic, the mass equation shows that in order to calculate the total energy, both the macroscopic and microscopic energies need to be considered. This gives:

$$E_{total} = E_{macroscopic} + E_{microscopic} \tag{2.3}$$

, where the liquid drop model represents the macroscopic part and the shell model corrections represent the microscopic.

2.2 Spherical Shell Model

The Shell Model is an example of a microscopic model. A fundamental assumption of the Shell Model is "the motion of a single nucleon is governed by a potential caused by all the other nucleons"[54]. If the nucleons are considered in this manner, then it allows nucleons to occupy a series of levels or shells, and within those levels, a series of sub-levels or sub-shells. The occupancy of these various shells and sub-shells is governed by the Pauli Exclusion principle which requires protons and neutrons to

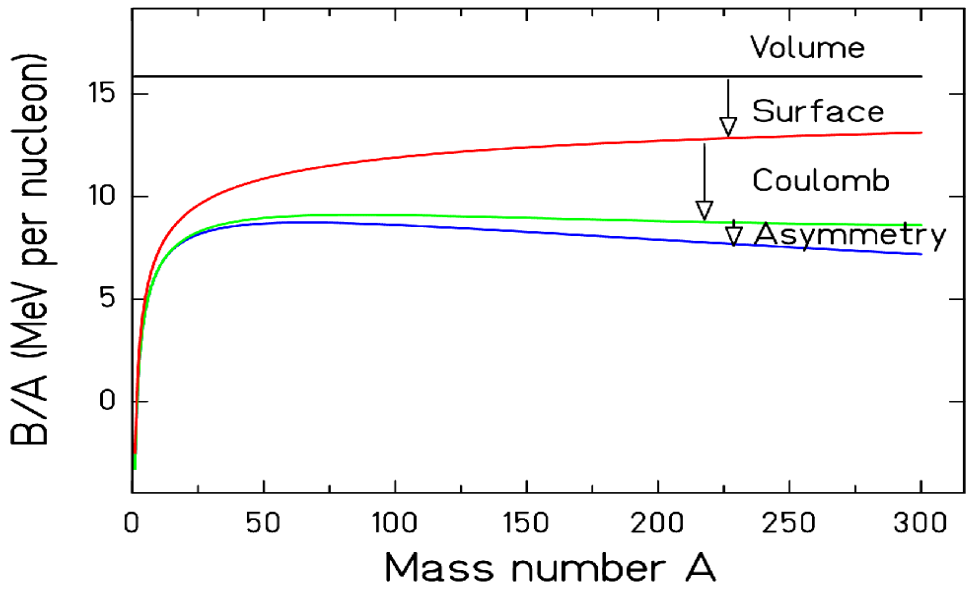

Figure 2.1: Contributions to the binding energy per nucleon according to the liquid-drop model along the beta stability line. The blue line is the total binding energy per nucleon [56].

be considered separately. The existence of the 'magic numbers' is also due to the shell structure of the nucleus. Comparing the separation energies of neutrons and protons with that predicated by the semi-empirical mass formula, then very visible jumps are seen at very particular numbers; 2,8, 20, 28, 50, 82 and 126.

The theoretical basis of the shell model is that the nuclear Hamiltonian can be written as the sum of an independent-particle Hamiltonian ($\hat{H}_0$) and a residual interaction $\hat{V}$ shown as [57],

$$\hat{H} = \hat{H}_0 + \hat{V} \tag{2.4}$$

. In order to calculate the potential of the shell model, two models are usually considered in the solving of the three dimensional Schrödinger equation as starting models. These are the Infinite Well and the Harmonic Oscillator Potentials, see Fig. 2.2. These two models were able to replicate the magic numbers of 2, 8 and 20, but higher numbers could not be produced by these models, see Fig. 2.3. These models were also not realistic, as both would require an infinite amount of energy in order to separate a neutron or proton.

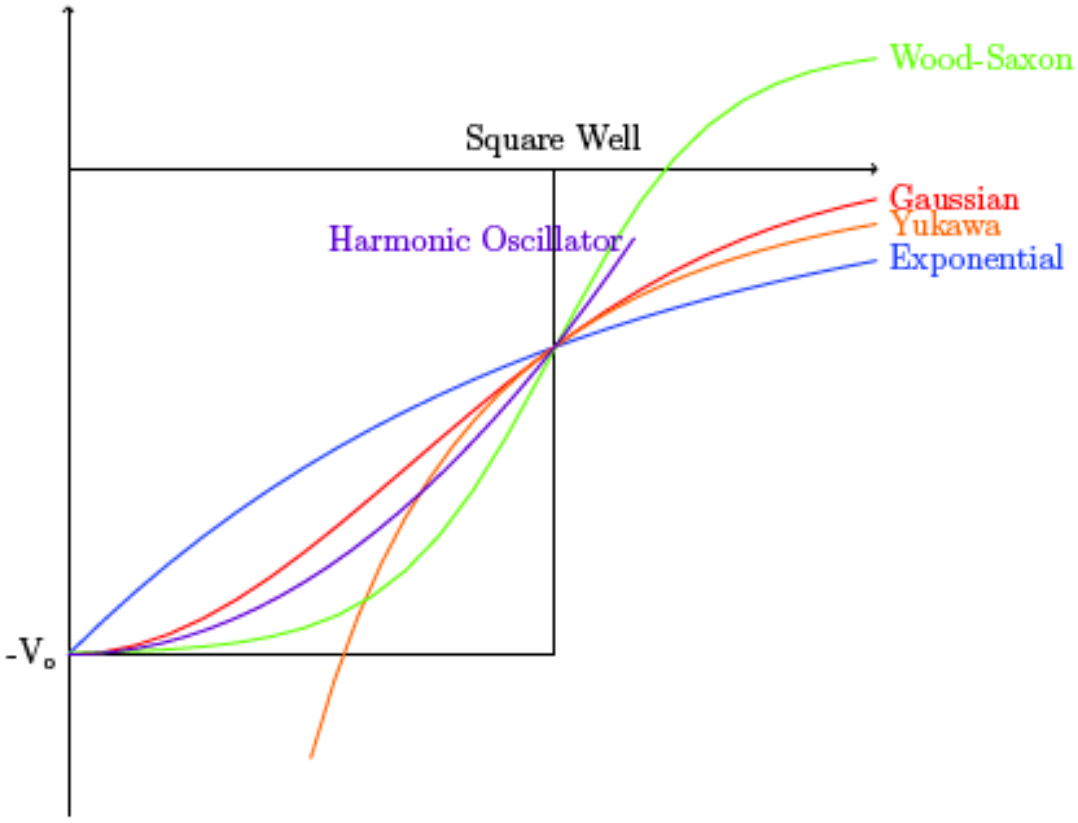

Figure 2.2: Graph of different potentials used to solve the Schrödinger equation. The Harmonic Oscillator and Woods-Saxon are given as examples in the text [58].

An improved model was developed to represent the nuclear potential more realistically, the Woods-Saxon Potential model. The shape of this potential is about half-way between the harmonic oscillator and infinite square well potentials, see Fig. 2.2 and is a good representation of the matter density distribution within the nuclei due to having more of a 'flat bottom' distribution [59]. It is given in the form,

$$V(r) = -\frac{V_0}{1 + \exp[(r - R)/a]} \tag{2.5}$$

, where $V(r)$ is the potential energy and V_0 is the well depth. This can be adjusted to give the correct separation energy. A typical value would be 50 MeV. R is the mean radius and is given by $R = 1.25A^{1/3}$ fm where A is the mass number. a is the skin thickness and has a typical value of 0.524 fm [54]. This potential again can provide the magic numbers of 2, 8 and 20 but fails at higher values, see Fig. 2.3.

In 1949 the model was improved by Maria Goeppert Mayer and Hans Jensen, who suggested, that similar to atomic physics, the nuclear potential should be a combination of a central potential and a strong spin-orbit interaction [61]. The spin-orbit interaction can be written as,

$$V_{so}(r)\mathbf{l.s} \tag{2.6}$$

, and causes the re-ordering of the levels. Each spherical level is now split into two, l + 1/2 and l - 1/2 depending on the orientation of L and S relative to each other. From Fig. 2.3 it can be seen that as L + 1/2 decreases, L - 1/2 increases in energy. It is therefore possible to give the states a total angular momentum $j = l + s$ [54].

2.3 Nilsson Model (deformed approach)

While the above described shell model can only be applied to spherical nuclei, the Nilsson model can be applied to nearly all deformed nuclei, and hence is one of the most successful models developed. It describes single particle motion within a non-spherical potential. This potential can be represented as [62],

$$V = V_0(r) + V_2(r)P_2(\cos\theta) \tag{2.7}$$

. In this case it is appropriate to use an axially symmetric single particle Hamil-

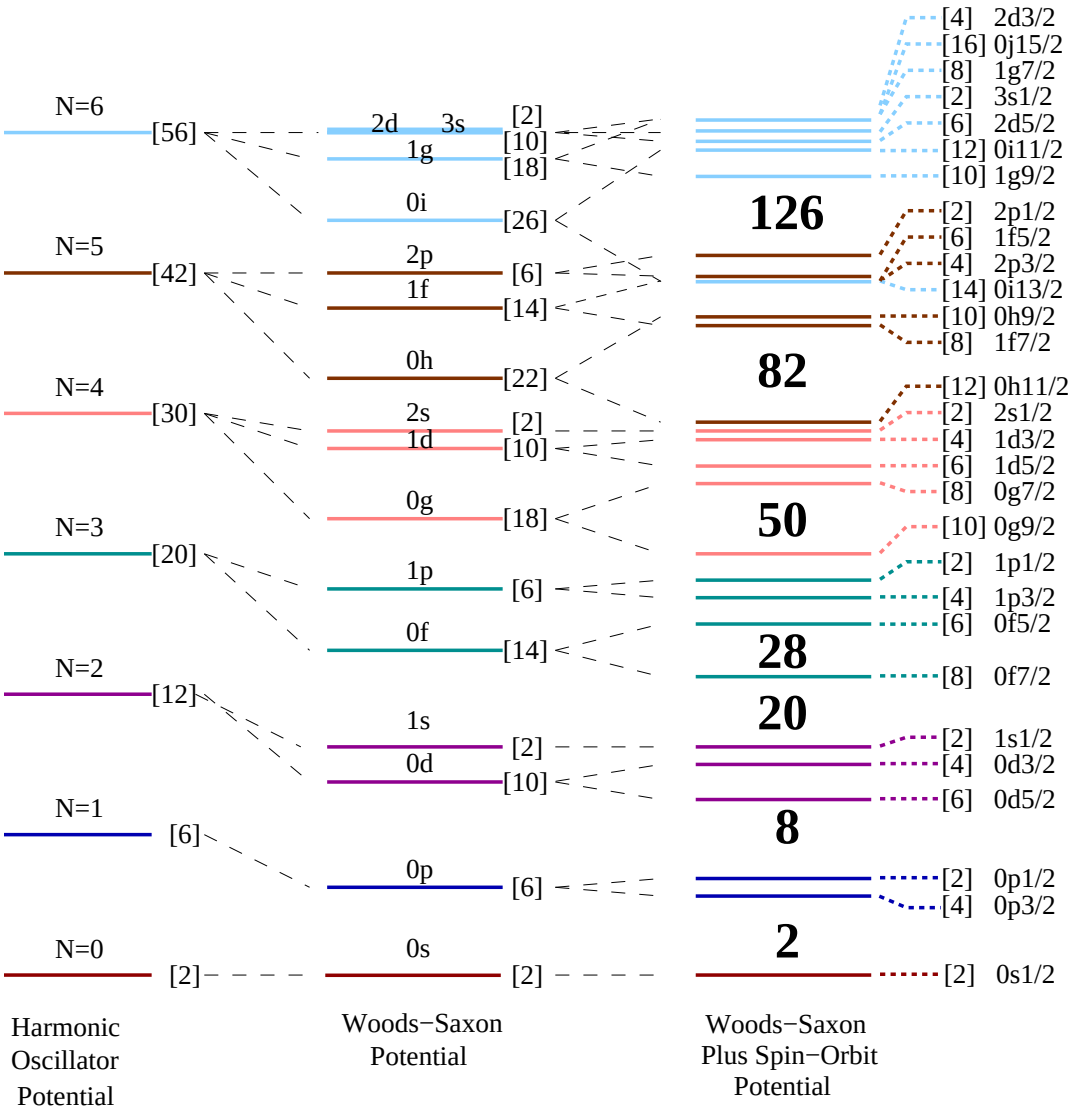

Figure 2.3: The levels generated by the Harmonic Oscillator, Woods-Saxon potential model and Woods-Saxon with the spin-orbit term potentials [60].

tonian with the form,

$$H = T + V \tag{2.8}$$

$$H = \frac{\mathbf{p^2}}{2m} + \frac{1}{2}m[\omega_x(\mathbf{x^2} + \mathbf{y^2}) + \omega_\mathbf{z}\mathbf{z^2}] + \mathbf{Cl}\cdot\mathbf{s} + \mathbf{Dl^2} \tag{2.9}$$

. The first two terms are representative of the kinetic energy and the harmonic oscillator potential, as seen in Equation 2.8. The third and fourth terms are from the spin-orbit interaction and an attractive term respectively [63]. The term $\mathbf{Dl^2}$ is only seen in relation to the harmonic oscillator potential. The purpose of the term is to make the bottom of the potential flatter and therefore closer in shape to the Woods-Saxon potential, which in turn has greater similarity to the actual density distribution in nuclei. The one-dimensional oscillator frequencies are defined by ω_x, ω_y and ω_z in the x,y and z directions. Furthermore, this condition satisfies

$$H\Psi_i = E_i\Psi_i \tag{2.10}$$

, where Ψ_i is a Nilsson wavefunction of the form [62],

$$\Psi_i = \Sigma_j C_j^i \Phi_j \tag{2.11}$$

, in terms of the spherical shell model wavefunctions, Φ_j which is weighted on the configuration mixing coefficients C_j^i.

In the spherical shell each of the single particle state energy levels has a degeneracy of 2j+1. If nuclei are deformed, then this no longer holds. The energy levels are now dependent on the spatial orientation of the orbit relative to the core [54]. This is demonstrated in Figure 2.4, where a valence nucleon with a single j orbit has been placed in a prolate deformed potential. In this situation the orbit at position K_1 will have a lower energy than the orbit labelled K_2.

The orbit orientation can be defined by Ω, the projection of total angular momentum j of the odd nucleon on the symmetry axis (orbital and spin s) [64]. This is shown in Figure 2.5 where

$$\Omega = \Lambda + \Sigma \tag{2.12}$$

, is the projection of angular momentum and projection of intrinsic spin along the symmetry axis respectively [64].

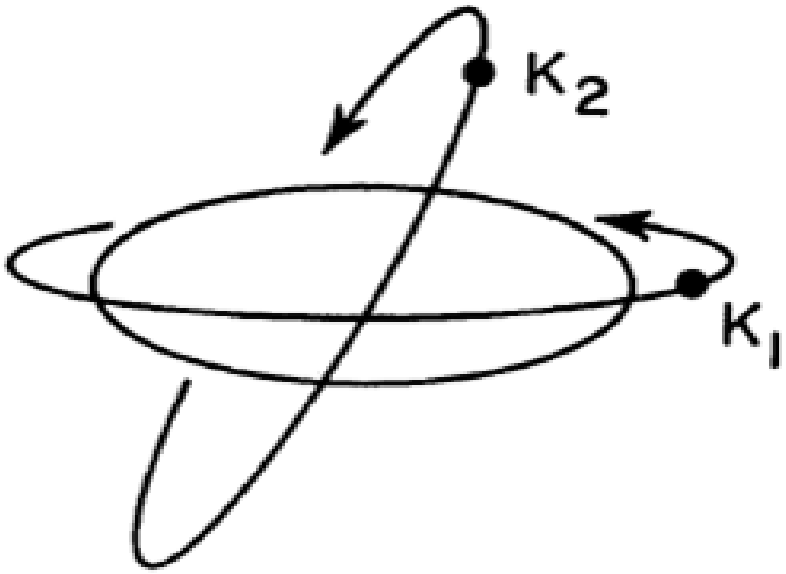

Figure 2.4: Comparison of two single-particle orbits K_1 and K_2. These orbits are shown at two diferent inclinations in relation to a prolate nucleus [62]

On the diagram, K is given as the total angular projection J, since in this case, it is only the axially symmetric nuclei that are considered. Since the rotational angular momentum for low-lying states is perpendicular to the symmetry axis Z, then K = Ω [62]. The angle between the symmetry axis Z, and the total angular momentum j, can be written as,

$$\theta = \sin^{-1} \frac{K}{j} \tag{2.13}$$

. In the first instance, the nuclei have reflection symmetry for either of the possible two Ω directions. The same energy will therefore be given to the +Ω and -Ω components which gives the levels a degeneracy of 2 [54]. Considering a prolate deformation, the state which has the smallest Ω value is the one which will interact most strongly with the core. This means it will be more tightly bound and hence lowest in energy. These states then increase as Ω + 1, Ω + 2 etc. On the oblate side, the converse is true. The state with the highest Ω value is the lowest state, and then follows as Ω - 1, Ω - 2 etc. A simplified version of the Nilsson diagram can then be produced, see Fig. 2.6.

However, if the rate of change of θ is now considered, then it is seen to change

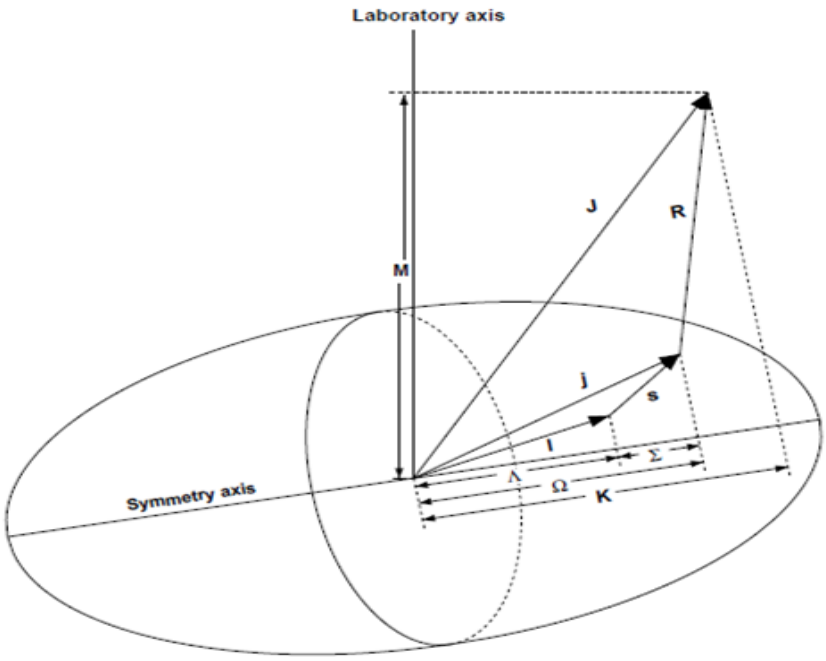

Figure 2.5: Diagram of the axes labels of a deformed nuclei [64]. The definition of each of the letters can be found in the text.

slowly for low values of K and faster for high values of K. This implies that the difference in energy will be smaller for low K values and larger for higher values of K. The corresponding simplified Nilsson diagram is shown in Figure 2.7.

To be able to build the full Nilsson diagram, several j values need to be combined. Since, according to quantum mechanics, it is not possible for two levels with the same quantum numbers to cross, then this means that no lines which have the same K value can cross in the Nilsson diagram. They therefore repel each other. The different j values can now be included to show the deformations where the orbit energies intermingle [62]. The relevant Nilsson diagrams are shown in Figures 2.8 and 2.9.

The Nilsson orbits are labelled as,

$$K^{\pi}[Nn_z\Lambda] \tag{2.14}$$

, where K is as previously described, π is the parity, N is the oscillator shell quantum number, n_z is the number of nodes in the wave function along the z axis and Λ is the component of the orbital angular momentum along the z axis [62],[59]. From previous, we defined $K = \Omega$. Eqn. 2.12 can therefore be re-written as,

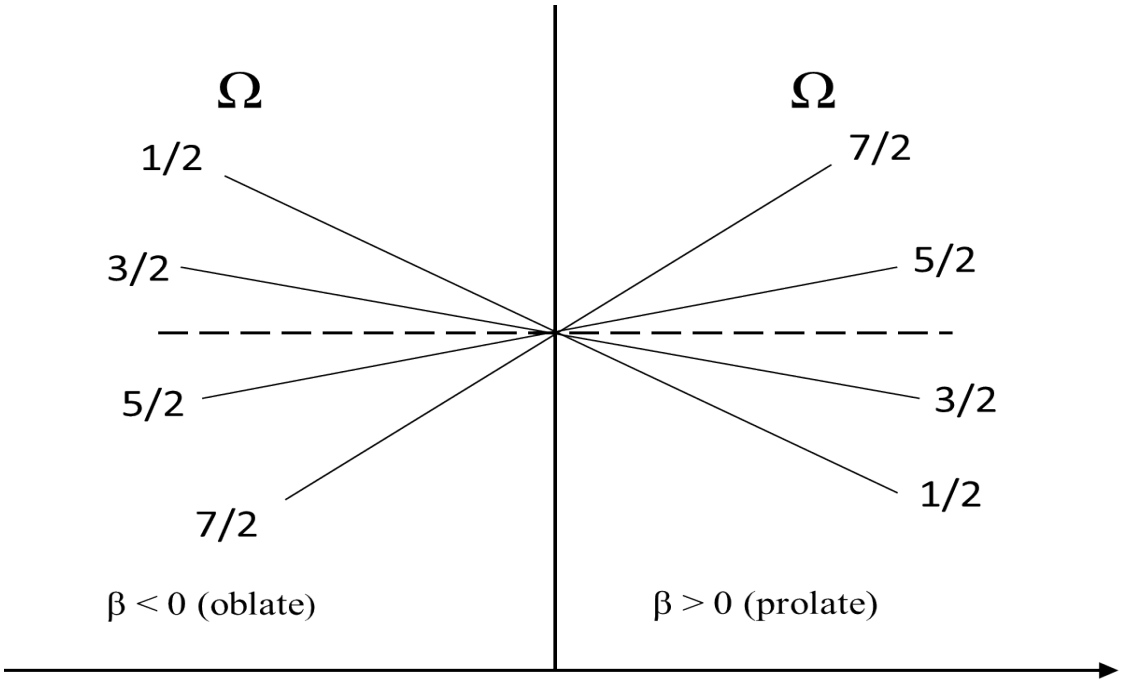

Figure 2.6: Diagram of simplified Nilsson model not taking into account the energy differences [54].

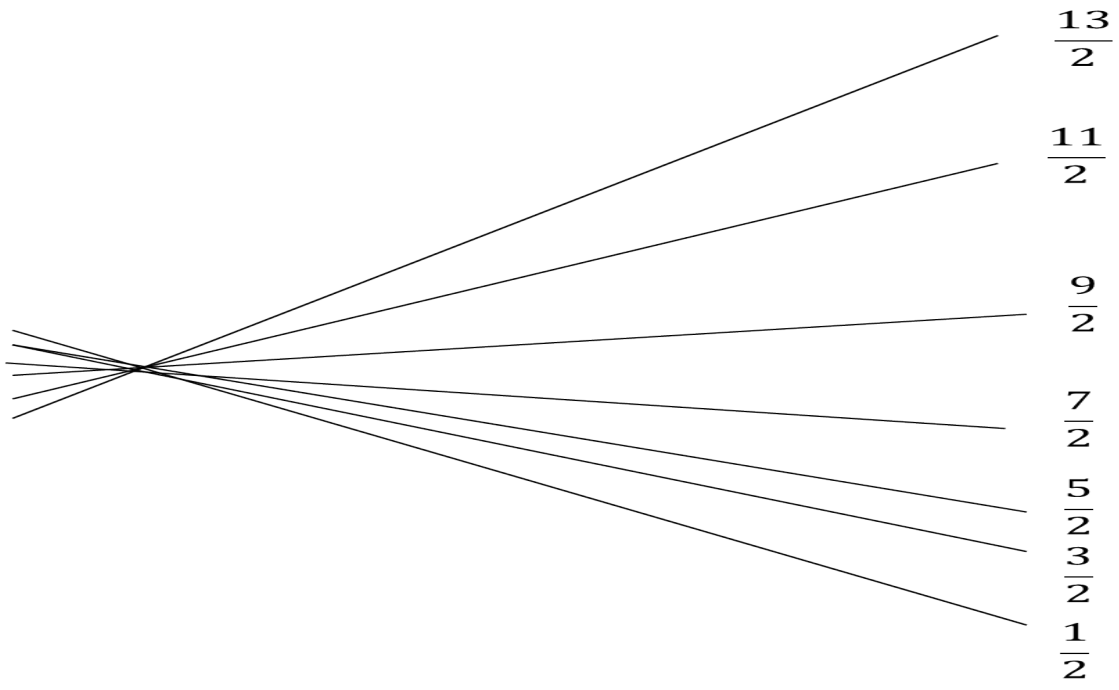

Figure 2.7: Diagram of second simplification of Nilsson model [62].

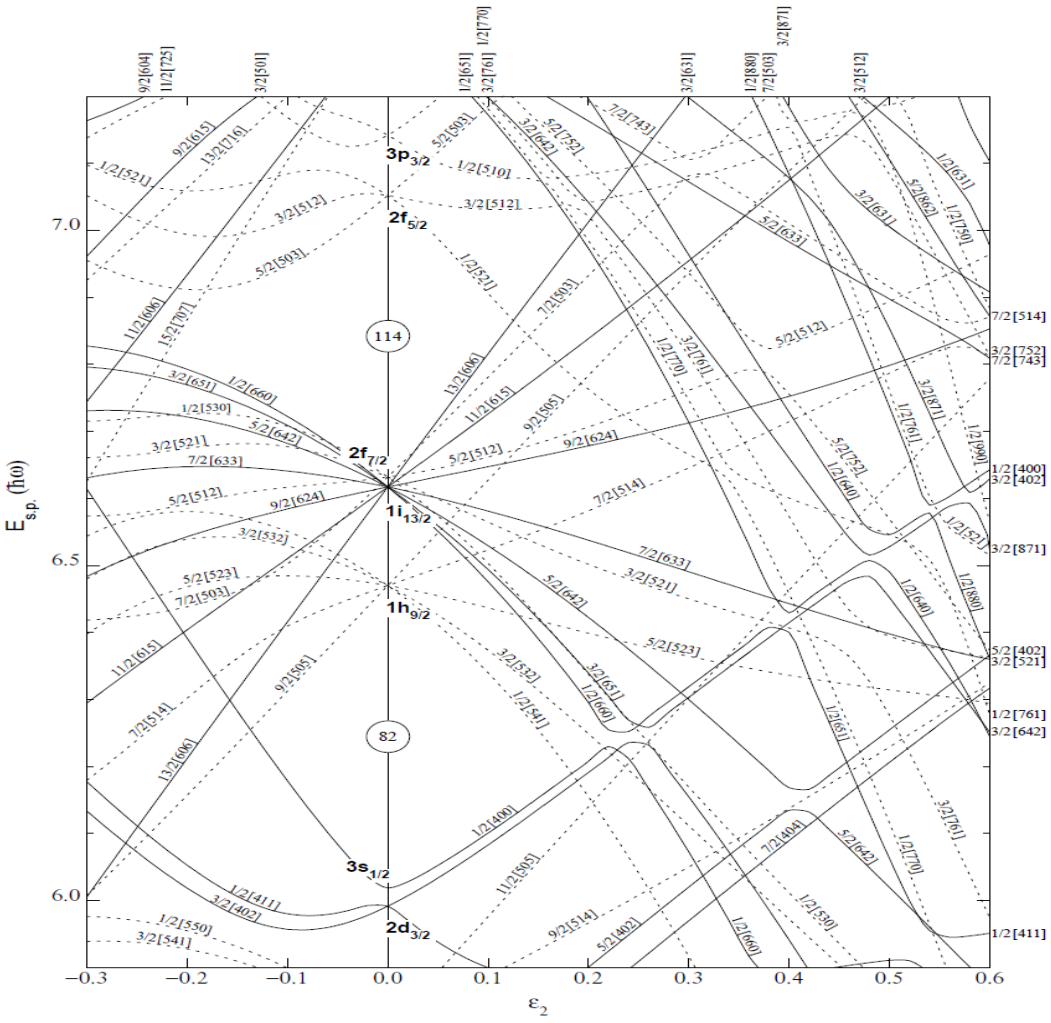

Figure 2.8: Nilsson diagram of energies for Z > 82 [64].

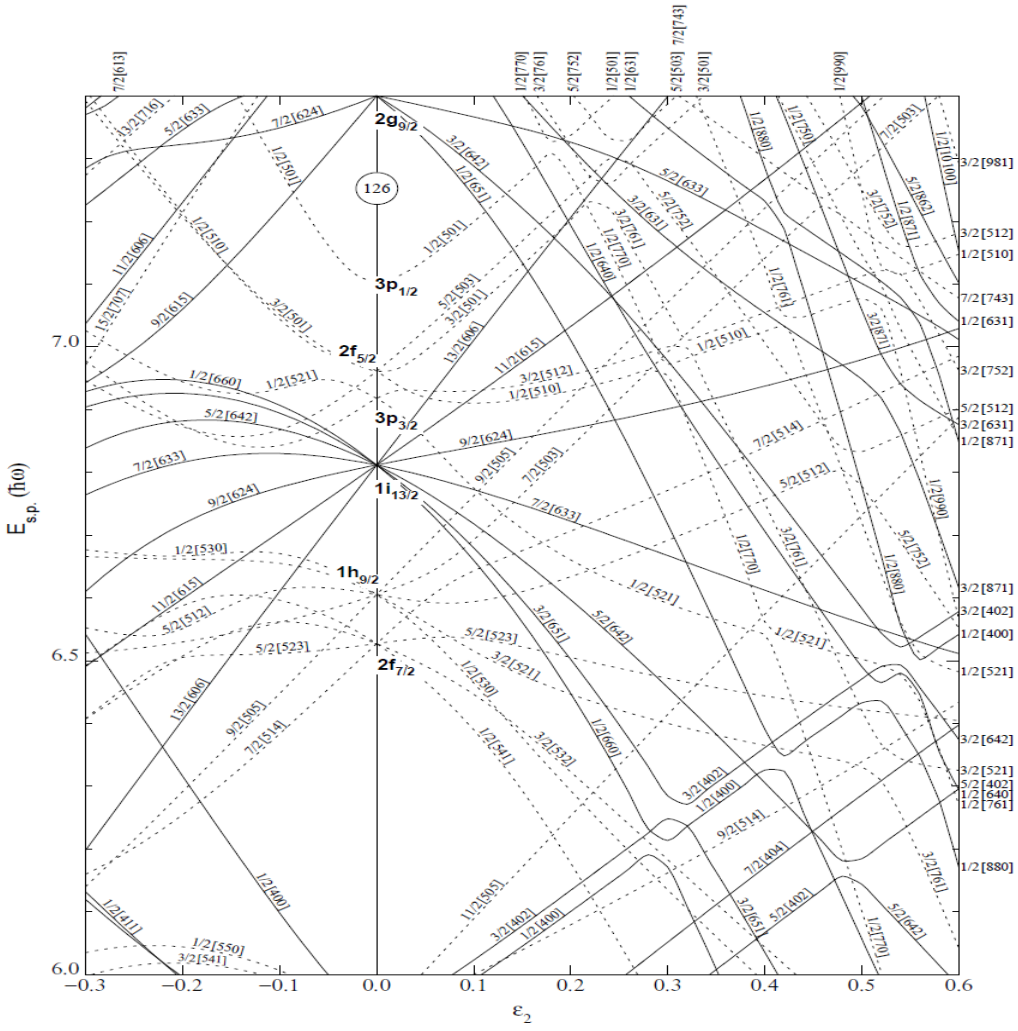

Figure 2.9: Nilsson diagram of energies for N $\leq$ 82 and $\leq$ 126 [64].

$$K = \Lambda + \Sigma = \Lambda \pm \frac{1}{2} \tag{2.15}$$

, where Σ is the intrinsic nucleon spin projection on the symmetry axis.

2.4 Alpha Decay

In 1909, six years after Rutherford had measured the charge to mass ratio of the α particles, he also showed that the α particles were helium nuclei, ^{4}He. Alpha decay is an effect of Coulomb repulsion, which has a greater effect for heavy nuclei, as the force increase at a rate of Z^2 compared to the specific nuclear binding force which increases as A. Spontaneous emission of an α particle can be written as [54],

$${}^{A}_{Z}X_N \rightarrow {}^{A-4}_{Z-2}X'_{N-2} + \alpha \tag{2.16}$$

. This spontaneous decay however, can only take place if the Q-value is greater than 0. The Q-value can be calculated as the difference in initial and final masses of the system. It can be written as,

$$Q_\alpha = (m_X - m_{x'} - m_\alpha)c^2 \tag{2.17}$$

, where the Q_α-value is the energy released in the α decay and m_X and $m_{x'}$ are the masses.

The kinetic energy of the fragments, $T_{X'} + T_\alpha$ is also equal to the Q-value. Equation 2.17 can now be modified to read,

$$Q_\alpha = (m_X - m_{x'} - m_\alpha)c^2 = T_{X'} + T_\alpha \tag{2.18}$$

. If it is assumed that the momentum of the parent is 0 and the momentum of the daughter and α particle is 0 (thus, assuming momentum conservation in α decay) then this allows the Q value to be re-written as,

$$Q_\alpha = T_\alpha \left(\frac{m_{x'} + m_\alpha}{m_{x'}} \right) \simeq T_\alpha \frac{A}{A-4} \tag{2.19}$$

. It is typical for the α particle to carry away approximately 98% of the Q-value, and the recoil daughter the remaining 2% [54], with A having a value of ~ 200.

It was noticed by Geiger and Nuttall that the larger the emitted α particle energy, the shorter the lifetime. This is reflected in what is known as the Geiger-Nuttall law

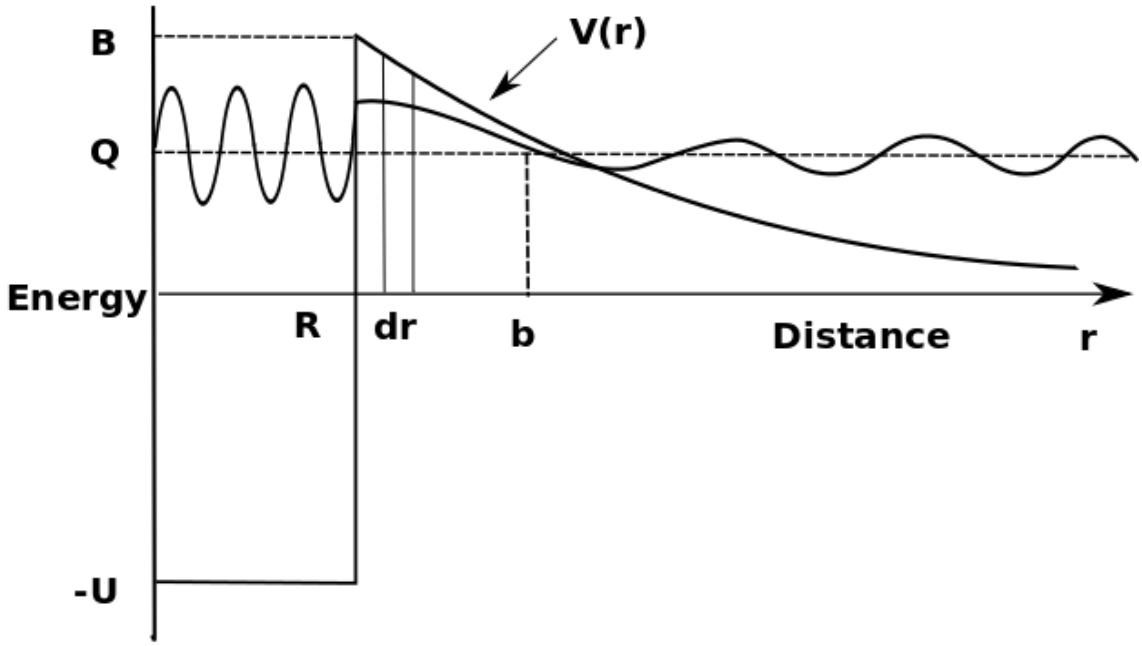

Figure 2.10: Schematic of α particle tunnelling. V(r) represents the potential energy between the daughter nucleus and α particle. At a distance of R≤r , the potential is a square well. Beyond this only the Coulomb repulsion causes an effect. The α particle tunnels through the barrier from R to b. Adapted from [6].

which describes this experimental observation. The law can be expressed as [55],

$$\log T_{1/2} = a(Z) + \frac{b(Z)}{\sqrt{Q_\alpha}} \tag{2.20}$$

, where $T_{1/2}$ is the half-life, and a(Z) and b(Z) are empirically-deduced constants which are different for each Z value.

The theory of α decay was presented both independently and simultaneously by Gamow (1928) [65] and Gurney and Condon (1928) who stated that "disintegration is a natural consequence of the laws of quantum mechanics without any special hypothesis" [66, 6]. The basis of the theory put forward, is that a pre-formed α particle is assumed to be in the nucleus, trapped there by the Coulomb barrier. The region in which it can move is determined by the potential of the daughter nucleus. The α particle can however escape by tunnelling through the Coulomb barrier.

The process of α particle tunnelling is shown in Figure 2.10. Here, V(r) is the potential energy between the daughter nucleus and the α particle, and is plotted as a function of the distance r between them. The height of the Coulomb barrier is represented as B. For the nuclei of interest, typical values are $B \sim$ 20–25 MeV, with

a Q_α value of $\sim$ 7–8 MeV showing that the process of α decay is sub-barrier one. At a distance of R≤r the potential can be thought of as a square well (as this is just the nuclear potential), with a depth -U. The α particle is able to move in this region and has an energy of Q + U [54]. The region between R and b forms the potential barrier. Here it is seen that the potential is larger than energy available, Q_α. Due to quantum mechanics, the α particle has a probability to tunnel through this barrier, which is represented by the point b on Figure 2.10. The potential over the interval *dr* can be thought of as many trapezoidal barriers through which the α particle needs to tunnel in order to escape the nucleus. If r > R, then the potential V(r) varies as 1/r and so R/b = Q/B.

The probability of the α particle tunnelling through the barrier is given as,

$$P = e^{-2G} \tag{2.21}$$

, where G is the Gamow factor given by,

$$G = \sqrt{\frac{2m}{\hbar^2}} \int_R^b [V(r) - Q]^{\frac{1}{2}} dr \tag{2.22}$$

, and can be evaluated to,

$$G = \sqrt{\frac{2m}{\hbar^2 Q}} \frac{2Ze^2}{4\pi\epsilon_0} [cos^{-1}\sqrt{x} - \sqrt{x(1-x)}] \tag{2.23}$$

, where x = R/b = Q/B [54, 6].

The probability formula given in Eqn. 2.21 can be extended to give an expression in terms of the decay constant, namely,

$$\lambda = Pfe^{-2G} \tag{2.24}$$

, where λ is the decay constant, G is the Gamow factor, P is now the pre-formation probability and f is the frequency of presenting at the barrier [6]. If this equation is combined with that in Equation 2.23 and values are inserted, it can be shown that the half-life is strongly dependent on Q_α and since the barrier height also increases with Z, then this also leads to an increase in the half-life.

Angular momentum I_α can be carried by an α particle. A parity change is possible with the decay, and therefore a selection rule must apply. In the case of α decay, "if the initial and final parities are the same, then l_α must be even; if the parities are different, the l_α must be odd" [54]. This focuses on decays between initial

and final states, but it needs to be remembered that an initial state can populate different final states in the daughter nucleus. This is known as fine structure.

The reduced width for α decay can be written as,

$$\delta^2 = \frac{h\lambda}{P} \tag{2.25}$$

, where δ^2 is the reduced width, h is Planck's constant, λ the decay constant and P is the barrier penetration factor [67]. If rates of α decay are being discussed, it is usual to refer to the hindrance factor (HF) which can be defined as

$$\mathrm{HF} = \frac{T_{1/2}(\alpha)_{exp}}{T_{1/2}(\alpha)_{theor}} \tag{2.26}$$

, where $T_{1/2}$ indicates it is the partial half-lives that are considered [68]. Primarily, this is the ratio between the rates of the ground state and the excited state α decay intensities, multiplied by the ratio of the barrier penetration factors. This however, does not take into account any effects from the centrifugal barrier. If it is possible to assign an angular momentum to an α decay, then a factor similar to the HF can be defined, however, the barrier penetration factor needs to be taken into account if allowing for any centrifugal barrier effects [67]. This is described by the expression,

$$V_l = \frac{l(l+1)\hbar}{2\mu R^2} \tag{2.27}$$

, where l is the angular momentum of the α particle, μ is the reduced mass and R is the relevant radius [69]. This can further be shown by Fig. 2.11 in which the potential energy of α decay is modified due to the centrifugal potential.

As mentioned previously, most simplified models assume that the α particle already exists within the nucleus and its rate of decay is determined by the potential barrier of the nucleus. When the half-lives of the α decay are investigated, it can be seen that some decays have a longer half-life than would be expected. One reason for this is that a change in spin can lengthen the half-life. This however, cannot always alone describe why some half-lives are longer than expected. This suggests that in some nuclei the process of creating an α particle is different.

This difference is most likely to occur in the nuclei which have an odd neutron, proton or both. Most α decay theories relate to even-even nuclei, in which the neutrons and protons are all paired off. To create an α particle, it therefore requires two of these pairs to join. In nuclei that have an odd proton, neutron or one of each

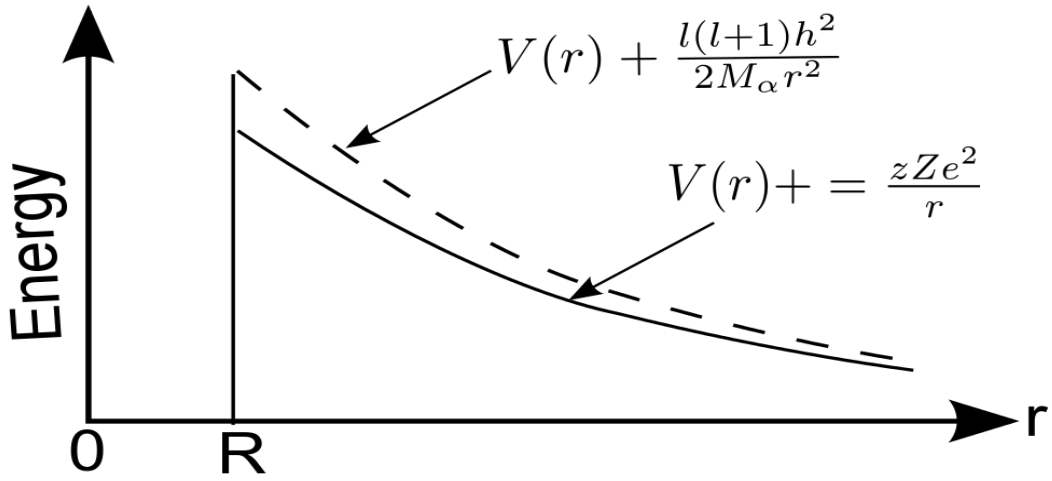

Figure 2.11: Potential energy modification in α decay due to the centrifugal potential. Adapted from [70].

(for odd-odd nuclei), then this particle can block access to pairings and that level is no longer accessible to α particle formation. In some cases, as in ^{196}At, although the odd particles do cause some blocking, they are mainly spectators with the decay occurring in the even-even core as will be shown in Chapter 6 based on reduced widths values.

2.5 Electromagnetic Transitions

If a γ - ray transition is considered, proceeding from an excited initial level of angular momentum I_i and parity π_i to a final level of I_f and parity π_f, then due to conservation of momentum it is required that,

$$\vec{I_i} = \vec{L} + \vec{I_f} \tag{2.28}$$

. This will give a range of L values from the largest $I_i + I_f$ and the smallest $|I_i - I_f|$ [54]. The radiation that is emitted can either be electric or magnetic and depends on the parity of the initial and final levels. If there is no change in parity then the radiation emitted is said to have even parity and if there is a parity change,

then it will have an odd parity. This can be summarised into selection rules as shown,

- $\Delta\pi = no$: even electric, odd magnetic
- $\Delta\pi = yes$: odd electric, even magnetic

. There is an exception to the rule. This is when $I_i = I_f = 0$ as $L = 0$ is forbidden. This is because $L \geq 1$ due to the photon having an intrinsic spin of 1 and there are no monopole transitions. Therefore, transitions where $I_i = I_f = 0$ can either decay by internal conversion (see Section 2.5.1) or the competing process of pair production, if the energy is greater than 1022 keV.

For each decay that occurs, it is possible to calculate the transition probability. The probability per unit time is therefore [54];

$$\lambda(\sigma L) = \frac{P(\sigma L)}{\hbar\omega} = \frac{2(L+1)}{\epsilon_0 \hbar L[(2L+1)!!]^2}\left(\frac{\omega}{c}\right)^{2L+1}[m_{fi}(\sigma L)]^2 \tag{2.29}$$

. In quantum mechanics, the radiation is emitted as discrete photons and so the matrix element of the multipole operator is required. It is of the form [6];

$$M_{fi}(\sigma L) = \int \Psi_f^* m(\sigma L)\Psi_i \, d\nu \tag{2.30}$$

, where the integral is over the whole volume of the nucleus, the wavefunctions Ψ_f and Ψ_i refer to the final and initial states of the nucleus and $m(\sigma L)$ is related to the multipole moment. This will then give a transition probability for the electric multipole of;

$$\lambda(EL) \approx \frac{8\pi(L+1)}{L[(2L+1)!!]^2}\frac{e^2}{4\pi\epsilon_0\hbar c}\left(\frac{E}{\hbar c}\right)^{2L+1}\left(\frac{3}{L+3}\right)^2 cR^{2L} \tag{2.31}$$

, and for the magnetic multipole it will give a transition probability of;

$$\begin{aligned}\lambda(ML) \approx & \frac{8\pi(L+1)}{L[(2L+1)!!]^2}\left(\mu_p - \frac{1}{L+1}\right)^2\left(\frac{\hbar}{m_p c}\right)^2 \\ & \times\left(\frac{e^2}{4\pi\epsilon_0\hbar c}\right)\left(\frac{E}{\hbar c}\right)^{2L+1}\left(\frac{3}{L+2}\right)^2\end{aligned} \tag{2.32}$$

. Estimates of these transition probabilities can be made by using an independent particle picture and considering transitions of a nucleon moving from one single-particle orbit to another, without affecting the rest of the nucleus. These estimates

Table 2.1: Weisskopf estimates for the first two multipole orders for electric and magnetic transitions. Values taken from [54] and [64].

Transition Probability	γ ray half-life
$\lambda(E1) = 1.0 \times 10^{14} A^{\frac{2}{3}} E^3$	$E1_{T_{1/2}} = \frac{6.76\times10^{-6}}{E_\gamma^3 A^{2/3}}$
$\lambda(E2) = 7.3 \times 10^{7} A^{\frac{4}{3}} E^5$	$E2_{T_{1/2}} = \frac{9.52\times10^{6}}{E_\gamma^5 A^{4/3}}$
$\lambda(M1) = 5.6 \times 10^{13} E^3$	$M1_{T_{1/2}} = \frac{2.20\times10^{-5}}{E_\gamma^3}$
$\lambda(M2) = 3.5 \times 10^{7} A^{\frac{2}{3}} E^5$	$M2_{T_{1/2}} = \frac{3.10\times10^{7}}{E_\gamma^5 A^{2/3}}$

are known as Weisskopf single particle estimates. As they are estimates, often they do not give correct theoretical values compared with the measured values. It is possible to say that if the calculated value is greatly reduced, then there may be poor matching of the final and initial levels. If the values are much larger, it suggests that the assumption that the transition is due to the single particle alone is not correct. An example of this is the strongly enhanced $2 \rightarrow 0$ E2 decays in the strongly-deformed nuclei. This effect is due to collective enhancement of the E2 decay strength [64].

By considering the reduced transition probability ($B_{sp}(\sigma L)$) and through the use of simplifying assumptions i.e. single particle, the following expressions can also be produced.

$$B_{sp}(EL) = \frac{e^2}{4\pi}\left(\frac{3R^L}{L+3}\right)^2 \tag{2.33}$$

$$B_{sp}(ML) = 10\left(\frac{\hbar}{m_p c R}\right)^2 B_{sp}(EL) \tag{2.34}$$

. These are the Weisskopf single particle estimates [6]. If the substitution $R = R_0 A^{\frac{1}{3}}$ is made, then it is possible to get estimates for the lower multipole orders. Examples are shown in Table 2.1 [54].

These multipoles may mix. The most common type of mixing that occurs, is the electric quadrupole E2 with the magnetic dipole M1. This will occur when the levels are such that the selection rules allow both to be permitted [71]. The strength of each in the mix can be calculated and is expressed in general terms as

$$\delta = \frac{< J_f||E2||J_i >}{< J_f||M1||J_i >} \tag{2.35}$$

, where J_f and J_i are the final and initial states respectively.

2.5.1 Internal Conversion

Instead of γ emission, the excitation energy can be directly transferred to an orbital electron, which is then emitted. This is called internal conversion. It also occurs in $0^+ \rightarrow 0^+$ decays as no γ transitions are allowed. If nuclear recoil is omitted, then the ejected electron has a kinetic energy of,

$$E_{el} = E_\gamma - B_e \tag{2.36}$$

, where E_γ is the transition energy and B_e is the binding energy of the electron in a specific electron shell [6]. It is possible to determine which shell the electron has been emitted from, as it will have a specific energy depending on its shell location. The electrons can therefore be labelled depending on which shell they originated from e.g. K,L,M. When an electron is emitted from an orbit, an electron from a higher shell will drop down to take its place. This results in the emission of characteristic X-rays or Auger electrons.

In some decays, internal conversion is the preferred method of decay over gamma decay. Therefore, when calculating the decay probability for gamma decay, the contribution from internal conversion needs to be accounted for. The total decay probability can therefore be written as the sum of two components; one from the gamma decay and one from the internal conversion,

$$\lambda_t = \lambda_\gamma + \lambda_e \tag{2.37}$$

. This can be re-written as [54],

$$\lambda_t = \lambda_\gamma(1 + \alpha_{tot}) \tag{2.38}$$

, where α_{tot} is the total internal conversion coefficient. This is defined as "the ratio of the electron emission rate (T_{ic}) to the gamma emission rate (T_γ)" [72] and is written as,

$$\alpha_{tot} = \frac{T_{ic}}{T_\gamma} \tag{2.39}$$

. This is for the total internal conversion coefficient, which is made up of the internal coefficients of each of the shells, such that,

$$\alpha_{tot} = \alpha_K + \alpha_L + \alpha_M + ... \tag{2.40}$$

. Each of these shell coefficients can also be broken further to give the subshell contributions.

2.6 Fission

As stated before, the process of fission can be likened to that of a liquid drop, first described by Meitner and Frisch [10] and further compared to a liquid drop by Bohr and Wheeler [53]. Although Bohr and Wheeler [53] were able to explain the process of fission, they could not explain why the actinides predominantly fissioned asymmetrically. The liquid drop model (LDM) therefore describes fission as the potential energy changes that are seen when there are shape distortions caused by the interaction of surface and Coulomb effects [73]. This picture however, does not take into account any shell effects or interactions caused by independent particle motion in the parent fissioning nucleus and/or in the fission fragments. The LDM was also found to not be sufficient to explain everything that was known by fission by the end of the 1950's [74]. The process of fission can therefore not be considered as a macroscopic model only, but as a macro-micro model in which shell effects also play a part.

In order to understand the measured values (e.g. mass-energy distributions, neutron multiplicities) and describe them theoretically, shell effects need to be taken into account [59]. It is these shell effects that are the reason for complex two-humped structures of fission barriers in some nuclei (fission isomers). Corrections were therefore made to the LDM in the form of shell corrections by Strutinsky [75].

The importance of shell structure becomes apparent when looking at asymmetric mass distributions of fragments, particularly those of heavier masses. The mass of the heavy fission fragment group tends to be constant at $A \sim 140$, whereas the mass of the light fission fragment group increases as the parent mass increases [54].

Therefore the macroscopic-microscopic model uses the LDM as the macroscopic part, and the shell model as the microscopic. However different variants of the LDM and shell model can be used, and have been used by different authors.

The second model type that can be used are the self-consistent microscopic models which are based on the Hartree-Fock Bogoliubov (HFB) method [76]. In these models there is no macroscopic part, and this model was used in the work by Ghys *et al.* [77].

Depicted in Fig. 2.12, is the potential-energy surface (PES) as a function of the deformation of the nucleus, of which the fission barrier is a point on this PES. At

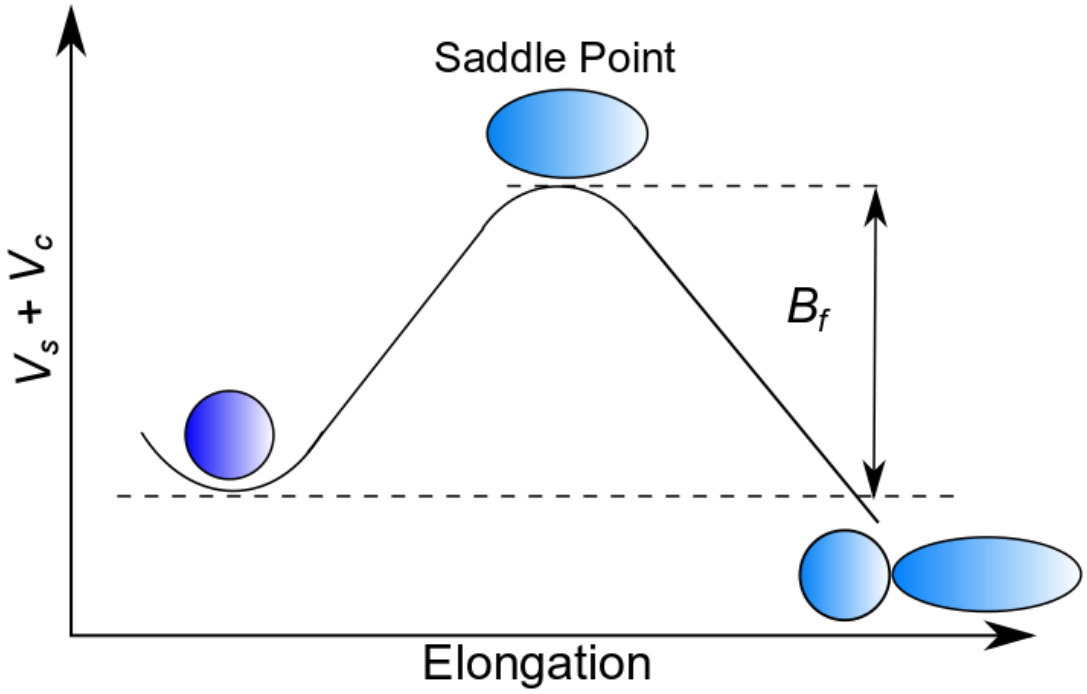

Figure 2.12: The sum of the Coulomb and surface energy as a function of the deformation. Marked on the diagram are the saddle point and the height of the fission barrier. Adapted from [58].

the saddle point, in most cases, the fission fragments have not yet fully separated. If the nucleus is able to traverse the barrier, it reaches the scission point, where the neck that has formed between the fragments breaks and the fragments separate. On Fig. 2.12 this occurs on the downward slope of the potential-energy curve after the saddle point. Since it is possible for the developing fission fragments to exchange nucleons, this leads to a variety of fission fragments being formed. This produces a spread of products varying in mass, proton and neutron number. Once scission has occurred the fission fragments are accelerated by the Coulomb repulsion between them [78].

2.6.1 Total Kinetic Energy

Of the energy released in fission, the largest amount is distributed to the kinetic energy of the fragments. The values indicate that the average total kinetic energy of the fission fragments does not depend on the initial excitation energy to a high sensitivity. This means that almost all of the kinetic energy of the fission fragments comes from the Coulomb repulsion which acts on the fission fragments after scission.

The total kinetic energy varies linearly with $Z^2/A^{1/3}$. This can be shown visually in Fig. 2.13 which was developed by Viola *et al.* [79] and provides a summary of TKE data for various nuclides.

However it was first noted by Terrell in 1959 [80] that since the kinetic energy of the fragments is caused by the Coulomb repulsion then it can be said that,

$$V_c = \frac{Z_1 Z_2 e^2}{R_1 + R_2} \tag{2.41}$$

. If it assumed to fission symmetrically and the radius is taken as $R = r_0 A^{1/3}$ then it can be said that,

$$V_c = \frac{Z^2 e^2}{8(\frac{1}{2})^{1/3} r_0 A^{1/3}} \tag{2.42}$$

. Although this shows the dependence already mentioned, the magnitude of r_0 will be too great. This is due to the fragments being assumed to be spherical [73]. This however is just a general guide and should not be depended upon since mass distributions can vary greatly from the expected values.

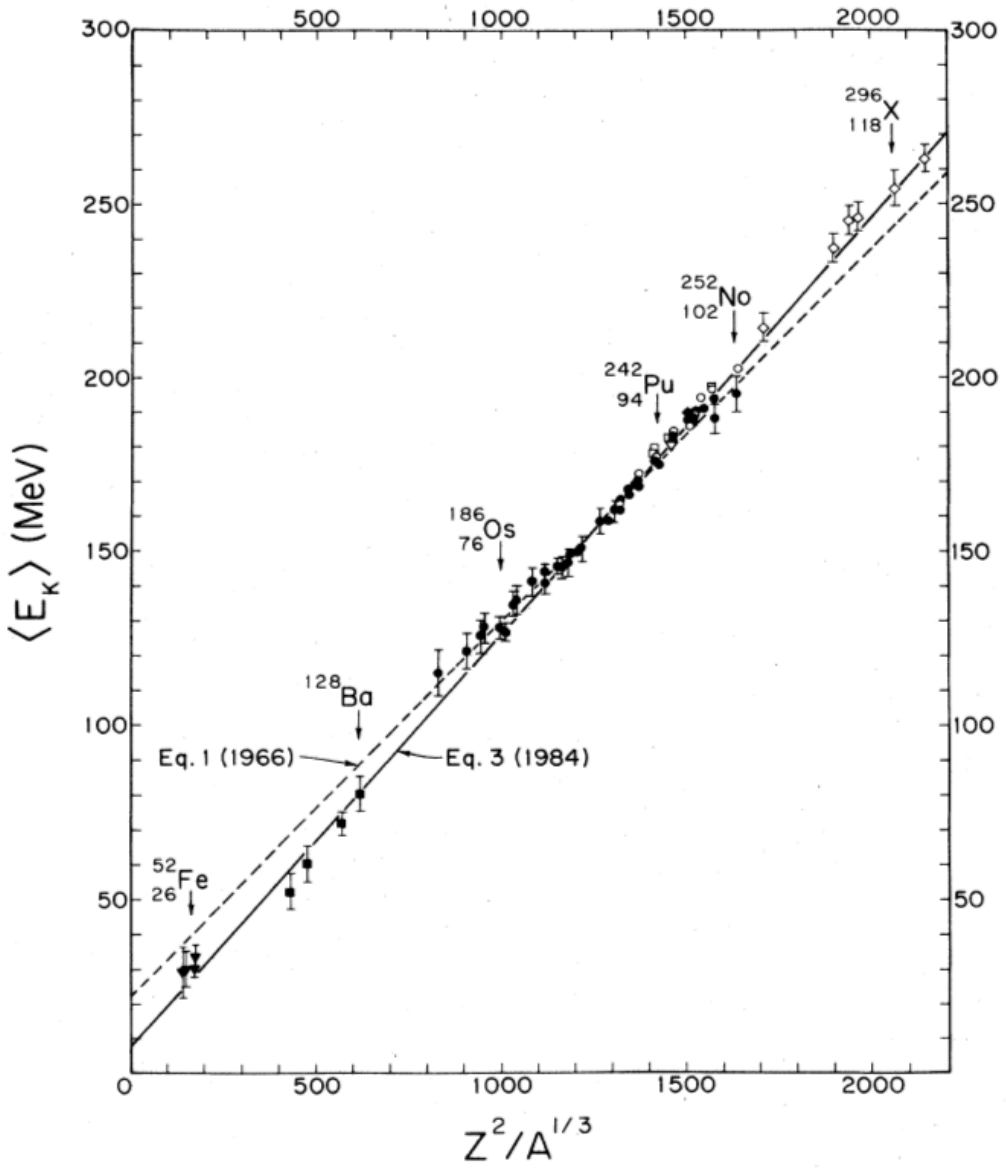

Figure 2.13: Viola plot of the relationship between TKE and $Z^2/A^{1/3}$ of fissioning nucleus [79]

2.6.2 Mass Distribution

The mass distribution of fission fragments can be classified in two distinct "modes", symmetric fission and asymmetric fission. The observation of asymmetric fission helped in the development of the nuclear shell model [81].

Asymmetric fission appears to be associated more with low-energy fission processes, rather than symmetric fission at the higher E^* [54].

The first explanation of distinct fission modes was proposed by Pashkevich [82] in 1971. At the transition state, the decision to fission asymmetrically or symmetrically is due to the difference in height for each of the fission barriers relating to the mass distribution. However, at the scission point, it is the average TKE difference that is the determinant. Fig. 1.2 provides a graphical summary of low-energy fission studies. It can be seen that the mass distributions fall into three categories, asymmetric, symmetric and bimodal mass distributions. It is noted in a paper by Itkis *et al.* [83], that around A ∼200, asymmetric fission is no longer favoured energetically.

The case of ^{180}Tl

In 2010, Andreyev *et al.* published a paper entitled "New Type of Asymmetric Fission in Proton-Rich Nuclei" [30]. This paper discusses the βDF of ^{180}Tl, whose β decay daughter is ^{180}Hg and was expected to fission symmetrically. The latter is believed to fission symmetrically since common arguments state that shell effects in the fragments determine mass distributions. For comparison, the predominant asymmetric mass split of heavy actinides is believed to be due to the strong shell corrections of the fission fragments in the vicinity of the doubly-magic ^{132}Sn. In the case of ^{180}Hg, a symmetric fission would lead to ^{90}Zr, (Z) = 40, which is a semi-magic number and a neutron number (N) = 50 which is one of the magic numbers. The fission of ^{180}Hg however, was found to be asymmetric. The asymmetric fragment distribution can be seen clearly in Figure 2.14.

To explain why ^{180}Hg fissions asymmetrically instead of symmetrically, Ichikawa *et al.* [32] produced the potential energy surface plot as shown in Figure 2.15 where the macroscopic-microscopic approach was used.

The blue area to the left of Fig. 2.15 is the ground state of ^{180}Hg. Moving out of this ground state there is an asymmetric valley and a symmetric valley. The symmetric valley is much deeper than the asymmetric valley and lies lower in energy at larger elongations. The entrance to the symmetric valley also lies at a much higher

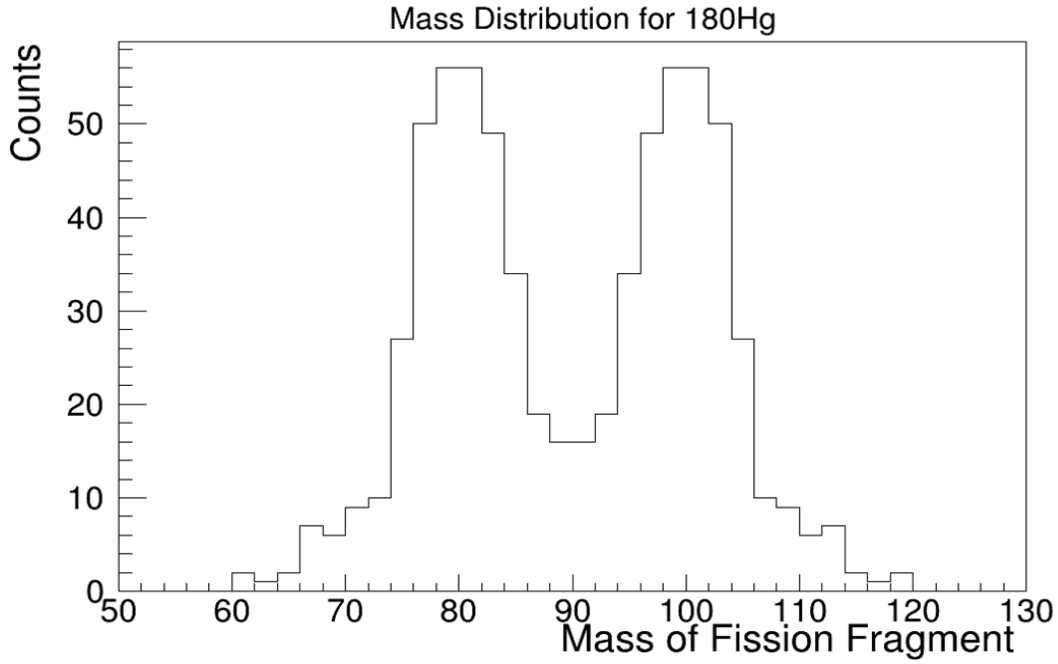

Figure 2.14: Asymmetric mass distribution of ^{180}Hg (adapted from [28]). ^{180}Hg was expected to fission symmetrically.

excitation energy than the entrance to the asymmetric valley. The two valleys are separated by a ridge, which as the elongation increases, disappears. It would then be expected that the system would then fall into the symmetric valley. This however is not the case, as by this stage a well-developed neck has formed, restricting the flow of mass between the forming fragments. This makes it un-energetically favourable to change from the asymmetric valley to the symmetric valley [30].

2.7 Beta-delayed Fission

Beta-delayed fission (βDF) is a two-step exotic decay process. Specifically on the neutron-deficient side, relevant to this work, a parent nucleus (*A, Z*) beta decays to an excited state in the daughter nucleus (*A, Z-1*), and if the excited state lies close to or above the fission barrier, then there is a probability that fission will occur. The fission from these states near the top of the fission barrier occur, in effect, instantaneously (10^{-14}–10^{-15} s) whereas the timescale for populating the states that may fission is determined by the half-life of the precursor nuclide [27], hence the delayed fission. Therefore in βDF the fission is from an excited state(s) in

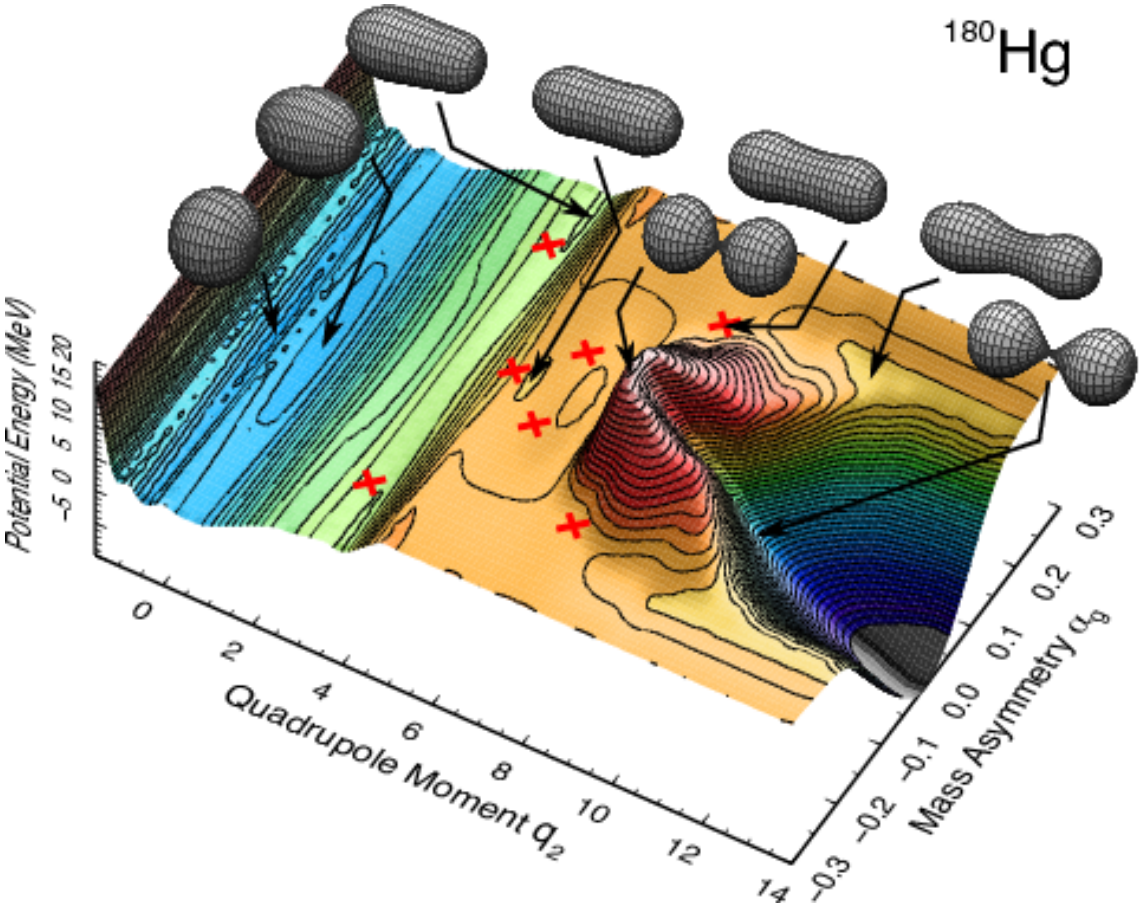

Figure 2.15: The above plot shows the potential energy surface of ^{180}Hg as calculated by Ichikawa *et al.* [32]. The ground state of ^{180}Hg is seen on the left hand side, at $q_2 = 0$, and mass-asymmetry $\alpha_\gamma = 0$. Although a deep symmetric valley is present, there is a large barrier that would need to be overcome in order to enter this valley. The red crosses indicate areas where there are small potential energy changes.

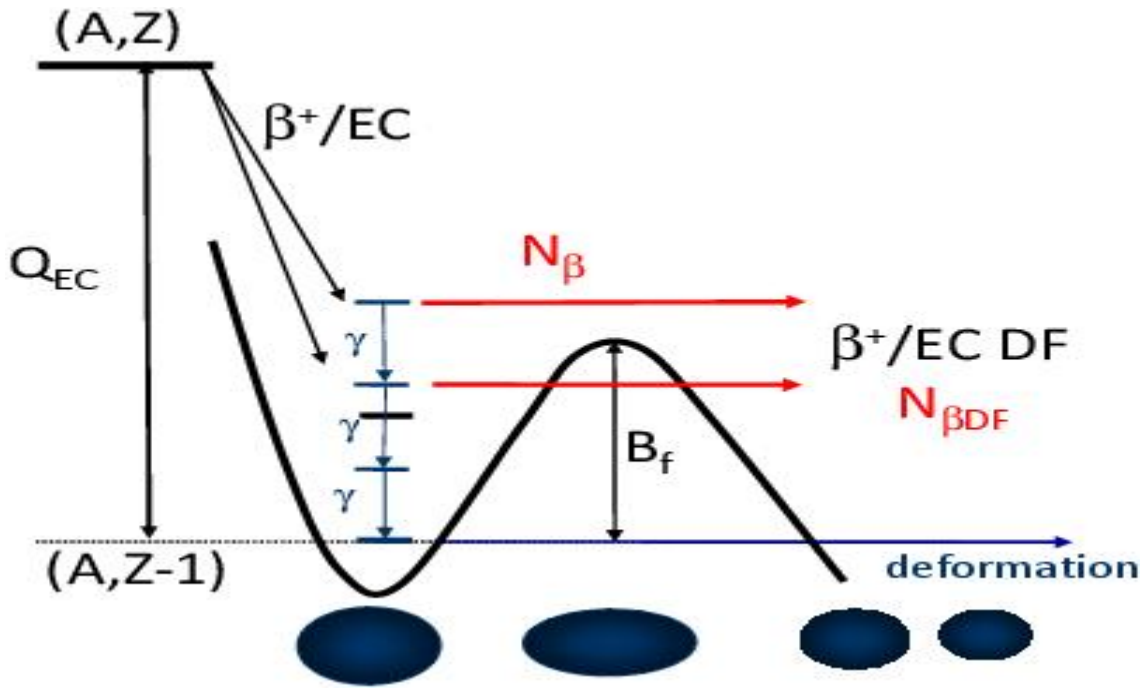

Figure 2.16: Diagram of the process of βDF for the neutron-deficient side of the chart. The Q_{EC} and B_f are indicated on the diagram [58].

the daughter but that the time behaviour of the fission is determined by the parent. The fission of the nucleus is however in competition from from other decay modes, i.e. γ and particle decay. This competition, and the β strength function, affect the probability of βDF occurring.

The probability of βDF can be determined from experiment using:

$$P_{\beta DF} = \frac{N_{\beta DF}}{N_\beta}, \tag{2.43}$$

, where $N_{\beta DF}$ is the number of fission events measured and N_β is the number of β decays.

βDF is a low-energy fission process where the excitation energy of the fissioning daughter nucleus is limited by the Q_{EC} value of the parent β-decaying isotope. In the lead region, this is normally a value of between 9–12 MeV. Fig. 2.17 shows the variation of Q_{EC}(At) and B_f(Po) for the βDF of astatine isotopes in the mass range of interest. For the lightest neutron deficient nuclei the Q_{EC} (Finite Range Droplet Model/Finite Range Liquid Drop Model (FRDM/FRLDM) [84, 85]), Q_{EC} (AME2012 [86]), B_f (FRDM/FRLDM), B_f (Thomas Fermi (TF) [87]) are plotted showing the decrease in Q_{EC} as B_f increases. This plot also demonstrates why it is

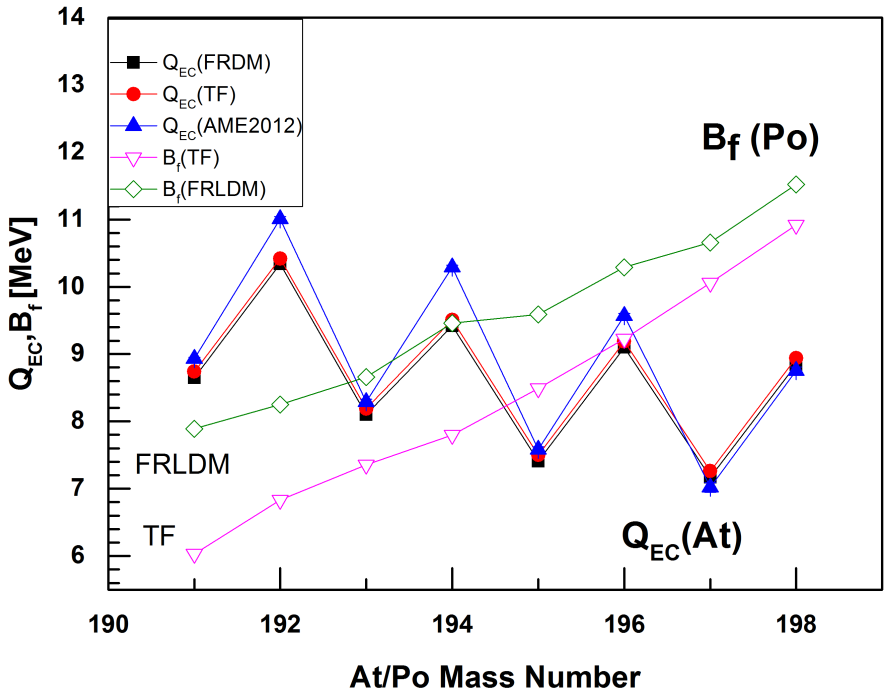

Figure 2.17: Calculated Q_{EC}(At) (closed circle and square symbols) and B_f(Po) (open symbols) values from the FRDM/FRLDM and from the TF model. The experimental Q_{EC} values from AME2012 are shown by the closed triangles.

only odd-odd nuclei that have been found to βDF. It can be seen that the parent astatines Q_{EC} values which have an even A have an energy $\sim$ 2 MeV higher than the odd - A astatines. This Q_{EC} difference and the production of an even-even daughter (which fissions more easily) is why βDF has only be observed for the odd-odd nuclei. This however can prove to be problematic due to the smaller mass astatine isotopes having more than one state present with a β branch. Also, it is not always known which state is the ground state, which is a general problem with odd-odd nuclei [24].

Calculating the Q_{EC}-B_f difference for ^{194}At, the FRDM/FRLDM estimate is $Q_{EC}(^{194}\text{At})$-$B_f(^{194}\text{Po})$= -0.04 MeV. In comparison, the value for ^{196}At is $Q_{EC}(^{196}\text{At})$-$B_f(^{196}\text{Po})$= -1.19 MeV for the FRDM/FLRDM, which is smaller.

This will likely be reflected in the value of $P_{\beta DF}$ which, as shown in the text, will be smaller than that of the lighter astatines. The value of -1.19 MeV also indicates that it will be sub-barrier fission that occurs in this case.

If it is assumed that the only criterion for βDF to occur is based on Q_{EC}-B_f, there would be a large number of nuclei for which βDF could be observed (except

the β-stable ones). Therefore by having a b_β which is non-zero and $> 1\%$, this limits the number of potential nuclei that can βDF to ~ 100 [24]. In Fig. 1.2 the diamonds represent the known βDF cases of which there are only 26.

Chapter 3

Experimental Method

3.1 ISOLDE Facility

All results discussed in this thesis are from experiments carried out at ISOLDE. The layout of the ISOLDE [88] facility can be seen in Figure 3.1. Highlighted on the figure are the locations of the High Resolution Separator (HRS) and General Purpose Separator (GPS) targets, the mass separators themselves and the beamline that was used in these experiments. These will be discussed further in this chapter.

3.1.1 Proton beam and Target

The protons are supplied to ISOLDE from the PS-Booster (PSB). The PSB is made from four synchrotron rings which receive protons from Linac2 at 50 MeV. These protons are then accelerated to 1.4 GeV. However, with the recent energy upgrade that took place in 2013 - 2014, the PSB is now able to supply 2 GeV protons. The protons are delivered as a series of pulses, with a duration of 2.4 μs and a spacing interval of 1.2 s. The pulses are grouped together in bunches that can contain 36 to 42 pulses to create a 'supercycle' which typically has a duration of $\sim$40–50 s. The pulses in each supercycle are either directed to ISOLDE or diverted to other set-ups. Typically 50% of the pulses in the supercycle will be sent to ISOLDE [90].

There are two target stations at ISOLDE, one for each of the mass separators. Different target materials are available and over 60 elements have been produced for study. The choice of target depends on the type of study being performed and the yield of the radioisotope to be produced. In the case of the experiments discussed here, a thick 50 g/cm^2 UC_X target was used, as shown in Figure 3.2 [91]. The UC_X target is composed of round discs, which are contained in a tantalum tube, which is

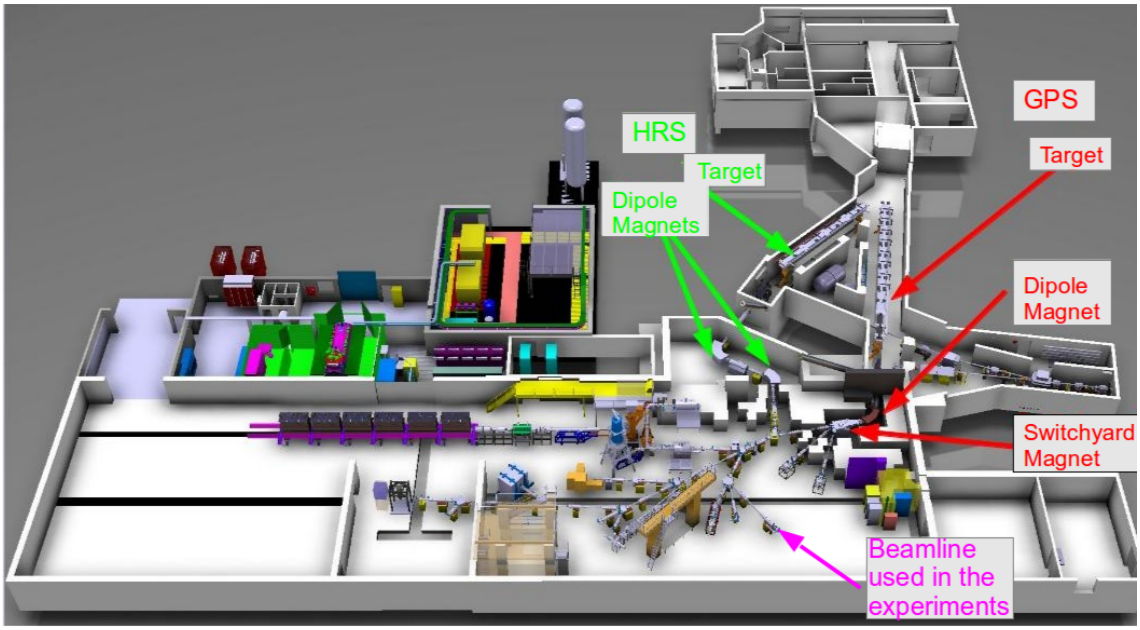

Figure 3.1: Layout of the ISOLDE facility. Labels on the figure indicate the main components of the facility. These are the HRS and GPS targets and associated mass separators, and the position of the Windmill system that was used. Image taken from [89]

.

heated to temperatures of between 1700 ℃ and 2400 ℃ [92].

When a high-energy proton hits the UC_X target, three main processes can occur. These are spallation, fission and fragmentation reactions [91]. Each of these processes is demonstrated in Figure 3.3.

This results in a large spread of products ranging from the very light to the heavy nuclei that the target material is made from. Spallation is a two stage process. The first stage, referred to as the intra-nuclear cascade (INC) occurs when the projectile (travelling at relativistic speeds) smashes into the target nuclei. Due to relativistic effects the wavelength of the projectile is such that it causes nucleon-nucleon collisions which form the INC. In stage two the remaining nucleus had thermal excitation energy and angular momentum. The nucleus therefore de-exites by evaporating large numbers of protons, neutrons and α particles and emitting γ-rays until it reaches ground state [93]. Spallation reactions mainly populate the neutron-deficient side of the nuclear chart. In the fragmentation process a variety of isotopes that are close to the target and projectile nuclei are produced. It can also produce very light nuclei. The third process is fission, in which the excited target nucleus splits into two nuclei, with the release of neutrons. The fission process

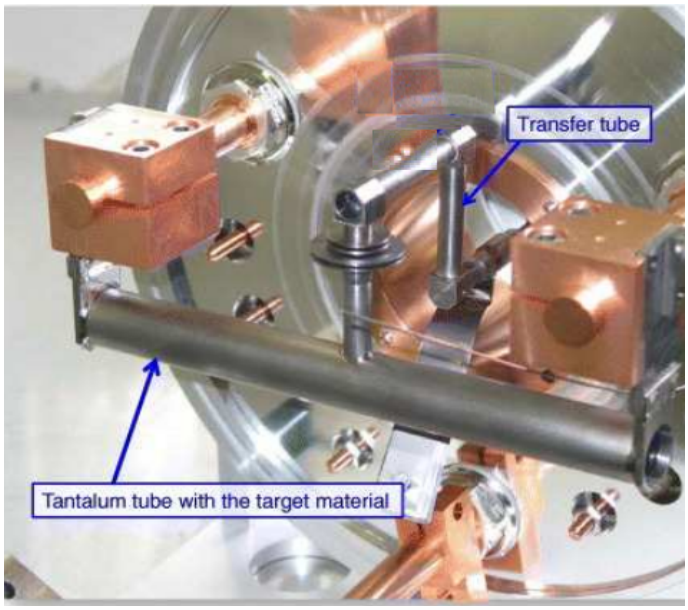

Figure 3.2: Image of the target used at the HRS and GPS. Adapted from [91].

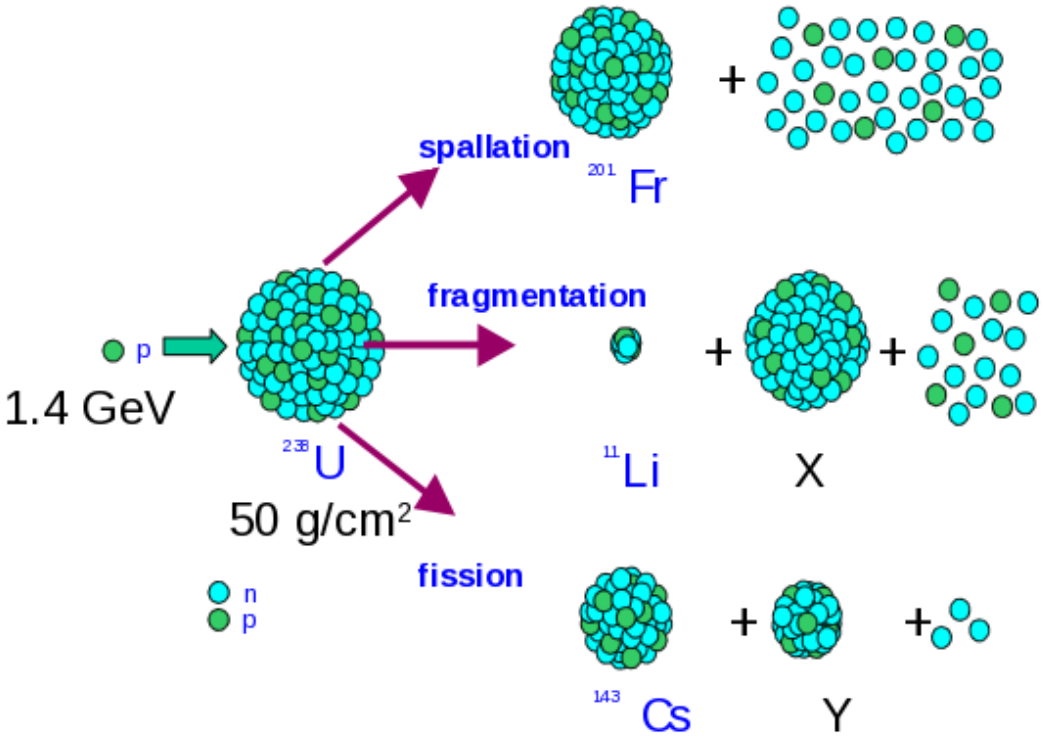

Figure 3.3: The three main production processes that occur when using an uranium target. These processes are spallation, fragmentation and fission [89].

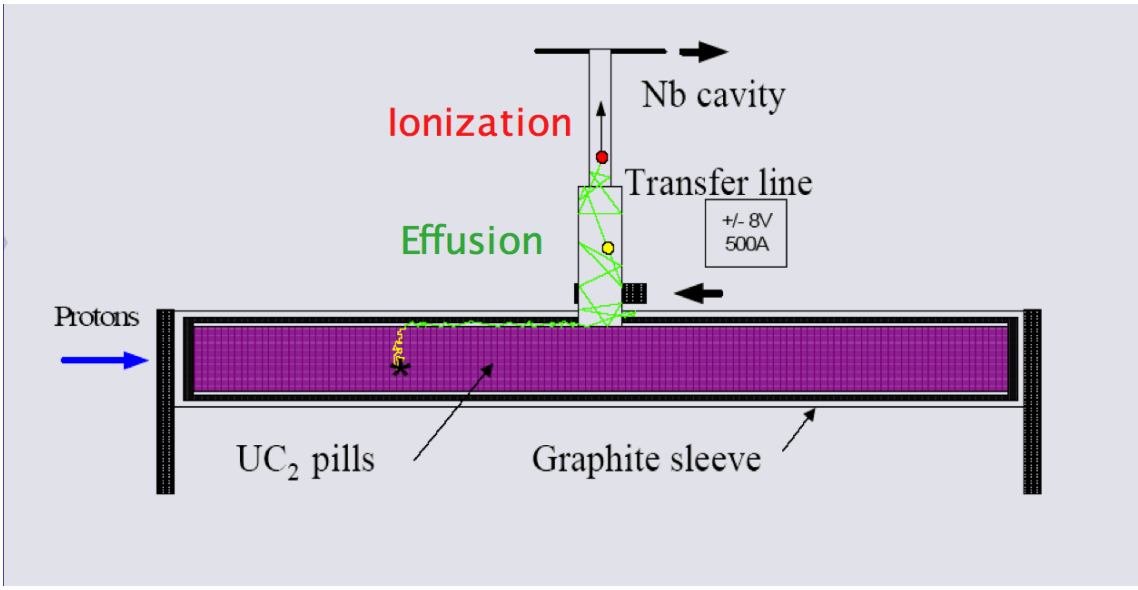

Figure 3.4: The path that the atoms take to travel from the target to the ion source cavity [89].

mainly creates the nuclei found on the neutron-rich side of the chart of nuclides [94]. This is because typically the nuclides that will readily undergo fission tend to be neutron-rich and therefore the daughter products they produce will also be neutron-rich. The astatine isotopes in this work were produced through spallation reactions. The reaction products travel by diffusion and effusion from the target chamber to the ion source through a transfer tube, as shown in Figure 3.4.

3.1.2 Ion Sources

Due to the high temperature of the target, then it is possible to get release times of under a second since the target is in carbide form. All the nuclei initially produced are in the atomic (neutral) state. Therefore to extract them from the target, they need to be ionised in an ion source. By applying a potential the ions can then be extracted from the source. There are three different types of ion sources at ISOLDE; surface, plasma and laser sources. These are outlined in the following subsections, but emphasis is placed on laser ion source, which was utilised in this work. An overview of each element produced at ISOLDE and its ionisation process can be seen in Figure 3.5.

Figure 3.5: The elements that can be produced at ISOLDE. Each colour represents the method by which the ionisation occurs. Some elements can be ionised by two methods. These elements are shown as boxes containing more than one of the colours [58].

Surface Ionisation

Surface ionisation has proven to be a very successful method to produce positive and negative ions of charge 1^+ or 1^-. In this process, an atom comes into contact with a heated surface and gains or loses an electron before being re-emitted as an ion [95]. The efficiency of surface ionisation is given by the Saha-Langmuir equation,

$$\frac{n_+}{n_a} = (\frac{\omega_+}{\omega_a})exp[-\frac{(I-\phi)\epsilon}{kT}], \tag{3.1}$$

, where n_+, n_a are the number of ions and atoms per cm^3, respectively, ϕ is the work function at temperature T, ϵ is the charge on an electron, k is the Boltzmann constant, I is the ionisation potential and ω_+, ω_a are the statistical weights of ions and atoms, respectively [96]. Ionisation efficiencies of 50-100% can be obtained for elements that have an electron affinity greater than 2 eV or an ionisation potential less than 5 eV [97]. Examples are francium and thallium isotopes, the former being one of the easiest elements produced at ISOLDE by surface ionisation.

Typically, this is a non-selective ion source, which does not provide strong element selectivity, except for specific cases of very easily-ionised elements, such as francium.

Plasma Ion Source

The plasma ion source can be used in cases where it is not possible to ionise an element by surface ionisation. Most ISOL plasma ion sources were based on the Forced Electron Beam Induced Arc Discharge (FEBIAD) design [98]. The ion source contains a gas mixture, argon and xenon in the case of ISOLDE, which is ionised by electrons which have been accelerated between the transfer line and the extraction electrode. The electrons can have energies of between 100 and 200 eV. This electrons are then capable of ionising any other atoms that are present in the ion source. The ion source installed at CERN is the MK5 high temperature plasma ion source, with a maximum temperature $\sim$ 1900 ℃ and has the advantage that the same current which is used to heat the transfer line, from target to ion source, also heats the disc-shaped cathode [99]. This is also a non-selective ion source, whereby all elements produced in the target will be ionised with comparable efficiencies.

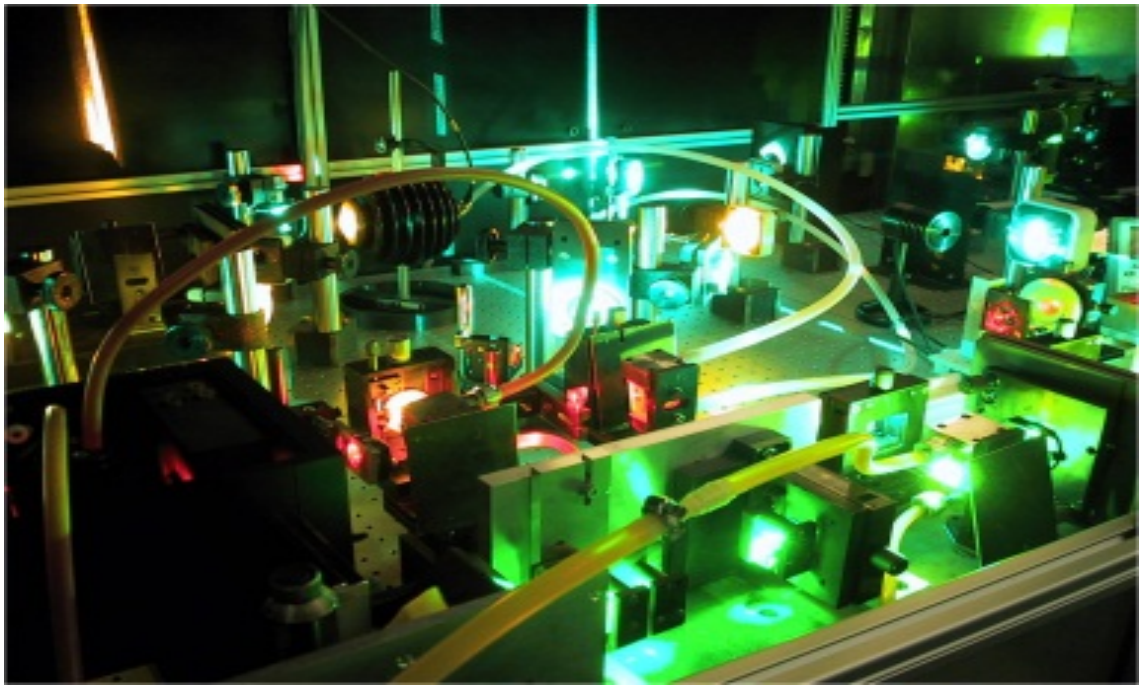

Figure 3.6: The RILIS system that was used to ionise the astatine.

3.1.3 Resonant Ionisation Laser Ion Source

The principle of a resonant laser ionisation source (RILIS) is to provide a multi-step ionisation process. Due to the nature of this process, a high degree of ionisation selectivity for a specific element can be achieved. A schematic demonstrating these ionisation methods is shown in Figure 3.7. The ionisation process can be effectively carried out by the use of pulsed laser systems. The laser photons are used for ionisation and have precise wavelengths to match the electron transition energies of an ionisation scheme. The ionisation stage involves a valence electron being excited in steps until it is above the ionisation potential.

The final step to ionise the atom can either be a non-resonant photo-ionisation to the continuum or, a resonant step into an auto-ionising or Rydberg state [100]. In the case of a Rydberg state, the atom is ionised with removal of an electron by a constant or pulsed electric field, absorption of an infra-red photon, or by a collision [92].

The confinement and extraction of the ions within the hot ion cavity source is identical to surface ion sources. The time taken for atoms to diffuse out of a hot cavity source is approximately 0.1 ms. This time is small compared to diffusion/effusion time from the target, which ensures that the conditions are suitable for ionisation

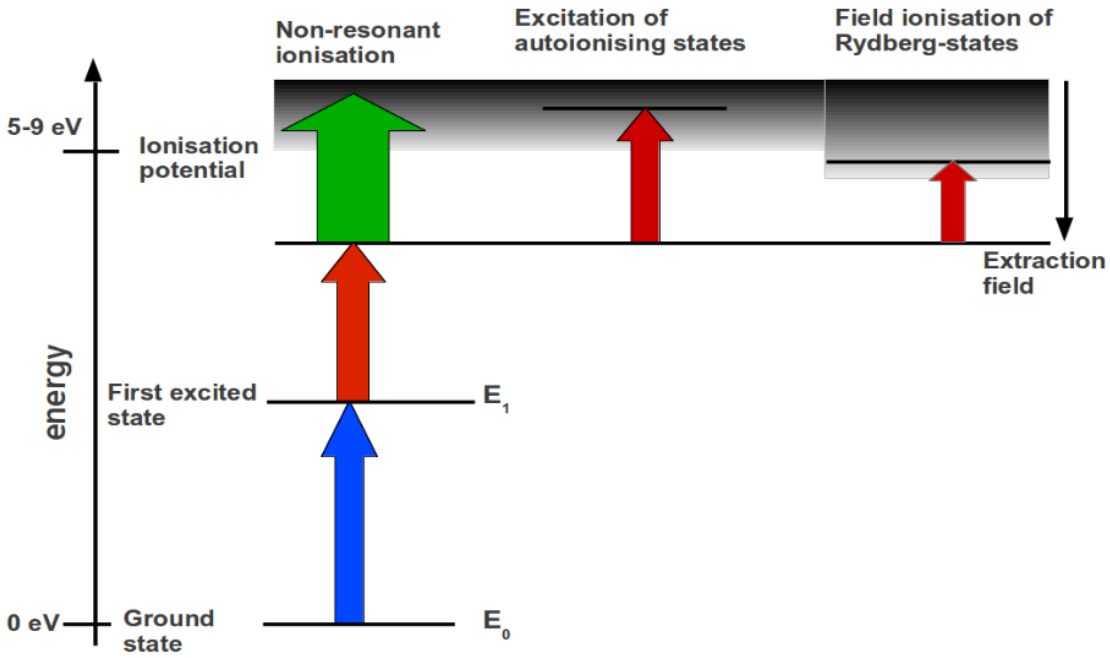

Figure 3.7: Diagram demonstrating auto-ionisation, ionisation to the continuum and via a Rydberg state.

of any short-lived isotopes. However, to ensure efficient interaction with the atoms, the lasers need to have a pulse repetition rate of at least 10 kHz [101]. Although the hot cavity does act as an impedance, it can only delay the effusion of atoms for approximately 100 μs until the next laser pulse is able to interact with the atoms [92]. The ionisation scheme for astatine is shown in Figure 3.8. The development of the scheme is described in the PhD thesis by Rothe [102].

After ionisation to the 1^+ charge states, the ions are extracted using a potential of 30–60 keV. After extraction, the ions are then mass separated by GPS and HRS, see next section. A summary of this whole process is depicted in Figure 3.9, which also shows three possible detector systems. The detector system pertaining to this experiment, the Windmill, will be discussed in detail in Section 3.2.1.

3.1.4 Mass Separation

There are two mass separators at ISOLDE, the General Purpose Separator (GPS) and the High Resolution Separator (HRS). Although each separator has its own target, they are both fed into a common beam line to allow the beam to be sent to any of the experimental lines. The GPS is the smaller of the two separators. Using

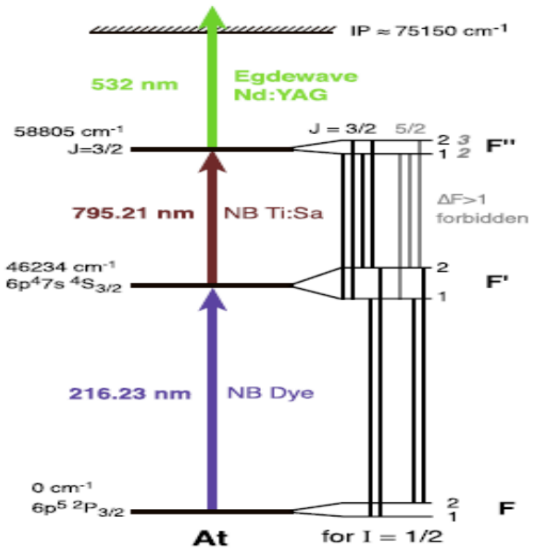

Figure 3.8: Ionisation scheme of astatine developed by Marsh *et al.*, [103].

an electrostatic switchyard magnet, three masses can be sent through beamlines known as mass lines. These are identified as the low, central and high mass lines. The low and high mass lines can select mass ranges at ±15% to the central mass line [88]. These three beams can be transported simultaneously to three different experimental set-ups in the experimental hall, however in practice this method is rarely used. The mass resolution m/Δm of GPS is approximately 2400 [88].

Whereas GPS has only one bending magnet, HRS has two magnets. One is located at 90° for the first separator stage, and 60° for the second separator stage [104]. Unlike the GPS, only one beam of a specified mass can be produced at HRS. The mass resolution of HRS is > 5000 [105].

3.2 Detector System

After mass separation the beam is transported to one of the three detection systems, being ISOLDE Farady cups, the Windmill decay spectroscopy setup and ISOLTRAP, the MR-TOF mass separator [103]. The Windmill detector system used in these experiments was designed and built at the Instituut voor Kern-en Stralingsfysica, KU Leuven, University of Leuven.

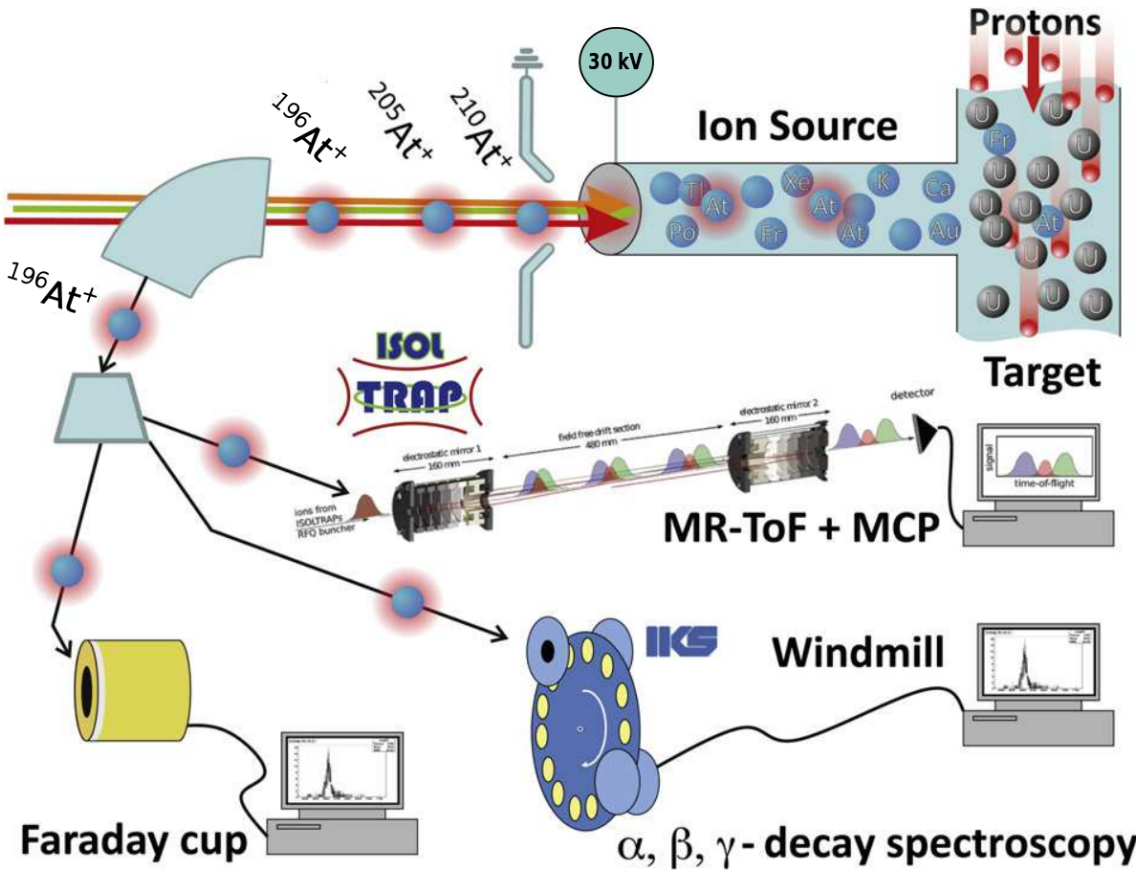

Figure 3.9: The summary of the production process for our experiments. The astatine, produced in the reactions between the beam of protons and the UC_X target, is ionised using the RILIS system. The ionised astatine is then extracted using a 30 kV potential. The astatine travels through a mass separator where the mass of interest is selected. This beam of relevant mass astatine is then directed to the detection station. Depending on the type of measurement that is being carried out, different detection stations will be utilised. Shown in the above diagram are the ISOLDE Farady cups, the Windmill α decay spectroscopy set-up and ISOLTRAP, the MR-ToF mass separator[103].

3.2.1 Windmill

The Windmill is a vacuum chamber containing four silicon detectors and an aluminium rotating wheel. Placed equidistantly around the wheel are ten carbon foils of thickness 20μg/cm^2. A picture of the inside of the Windmill chamber is shown in Figure 3.10.

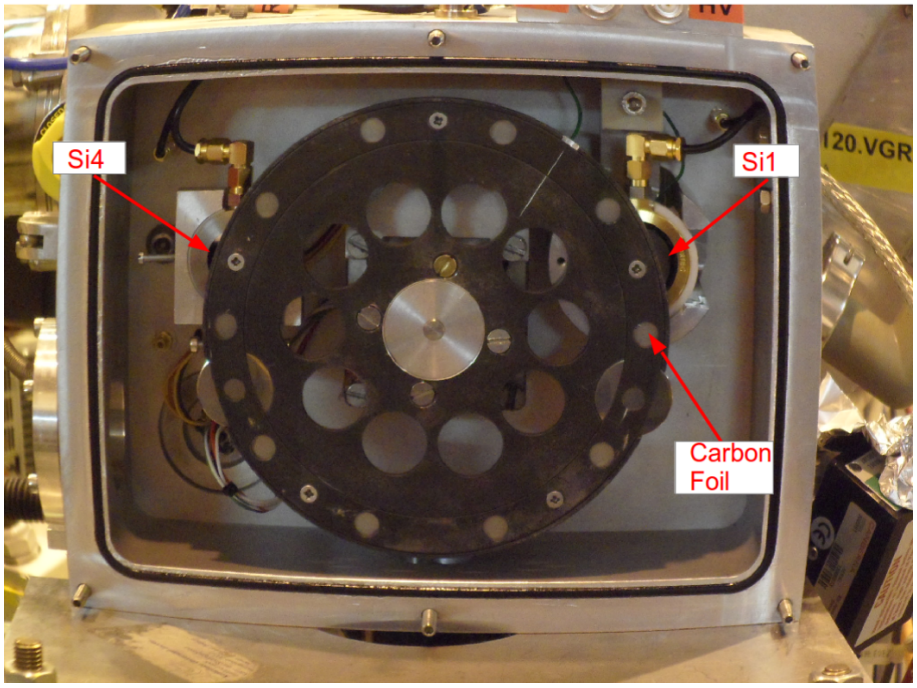

Figure 3.10: Picture of inside the windmill chamber while it is open. The rotating wheel is clearly seen in the centre of the chamber. Although mainly hidden behind the wheel, Si1 and Si4 can be seen. The silicon detectors and carbon foils are labelled.

The beam enters the chamber through the hole of a surface barrier annular detector (43-051F). This detector is known as Si1. The annular detector has a depletion depth of 300 μm with an active area of 450 mm^2 and a central hole of 8 mm. The beam then implants into one of the carbon foils. The thickness of the carbon foils required for this experiment was determined using the program SRIM [106]. The carbon foils needed to be thick enough to stop the incoming 30-60 keV beam to allow implantation, but thin enough to allow α particles and fission fragments to escape with a minimal amount of energy loss. Situated behind the carbon foil is a second surface barrier detector known as Si2. This detector is totally-depleted (47-038D) with a depletion depth of 300 μm and and active area

of 300 mm^2. The Full Width Half Maximum (FWHM) of the annular and totally depleted detectors are 25 keV and 20 keV respectively for α particles, measured with the 5.486-MeV α-decay from ^{241}Am [107]. The pairing of Si1 and Si2 allows for coincidence measurements of the fission fragments. This is important as only for coincident events can the mass distribution be extracted (as explained in Chapter 5). The location of Si1 and Si2 is known as the implantation position. After a supercycle is finished, the wheel is rotated 144° anticlockwise using a step motor to the decay position [108]. Two Passivated Implanted Planar Silicon (PIPS) detectors are situated here in the same geometry as Si1 and Si2. These detectors are known as Si3 (74256) and Si4(74257) [58]. The thickness of the detectors was 300 μm with an active area of 300 mm^2[109]. The FWHM of an α particle is 15 keV using 5.486-MeV α particles from ^{241}Am. The use of Si3 and Si4 allows long-lived daughter and granddaughter products to be studied. The positioning of all four silicon detectors can be seen in the schematic shown in Figure 3.11 and the photographs in Figure 3.12.

Silicon detectors are a type of semiconductor detector. For a semiconductor detector to work, a junction needs to be formed. A commonly used junction is the pn junction. These are formed using specialised techniques to join to n- and p-type semiconductor material in one crystal. For a semiconductor material to be n-type it will have been doped by an impurity that will result in an excess of electrons. Conversely, a p-type semiconductor material is one which has been doped with an impurity to produce an excess of holes [110] The formation of a pn junction creates an area around the junction depleted of charge carriers. Since the concentration difference of holes and electrons in each material is different, holes will initially diffuse towards the n-type region and electrons towards the p-type region. This causes a charge buildup on either side of the junction, and hence an electric field. This electric field, in turn, creates a potential difference across the junction, known as the contact potential. This changing potential is the depletion region. This area has no charge carriers and any electron-hole pairs that are produced by ionising radiation will be removed by the electric field [111]. This generates an output signal, which will be proportional to the energy of the incoming ionising radiation, which can then be displayed using analysis software.

Although a detector with the above description will work, it will have a very poor performance. If an external voltage is applied, in particular a reverse-bias, the performance is found to improve considerably. In this configuration the holes and electrons are attracted away from the junction with the effect that the depletion

region increases in size. This increases the volume of material that can be used for detection purposes and any charge carriers created in this region can be collected quickly. The depletion region width can be adjusted by altering the external applied voltage. A higher external voltage will produce a wider depletion region. There is however, a limit to the voltage that can be applied. The resistance of the semiconductor determines this limit and if this resistance is exceeded, the junction will breakdown and no longer operate in the required manner.

There are also two High Purity Ge detectors as part of this set-up, one detector directly behind Si2, and the second at 90° anticlockwise with respect to the first as shown in Figure 3.13. These are known as Ge1 and Ge2. Germanium detectors can detect γ rays through three interactions that γ rays have with matter. These are the photoelectric effect, compton scattering and pair production. In these processes, the γ ray loses energy through absorption or scattering. Some γ rays, however, will not interact and pass straight through a material losing no energy.

To construct a germanium detector a large piece of high quality germanium is heated to further remove any impurities, and this process is repeated until the impurity levels are very low. A single large crystal can then be grown from this material. Depending on which impurities are remaining in the crystal, it can be either mildly n- or p-type. HPGe detectors are normally operated as fully depleted detectors. Applying a reverse bias to the crystal's electrical contacts creates a depletion region. The lower the impurity levels, the larger the depletion region for a given voltage.

Silicon Detectors and Fission Fragments

Fission fragments have much larger masses than α particles and this leads to performance effects occurring in the silicon detectors. This is commonly known as pulse-height defect (PHD) [113, 111]. Due to their larger mass, the fragments will lose more energy when passing through the entrance window than lighter particles of the same energy. Fission fragments also create a high density of electron-hole pairs due to their high effective charge. This 'cloud' affects the external electric field, and electron-hole pairs are not moved straight away resulting in a higher chance of recombination compared to the detection of α particles. Diffusion will dissipate the cloud and the pairs will drift again under the influence of the electric field, but with a delay. This means that the detector calibration will differ for different particle types. A particular calibration method is therefore used for fission fragments which will be described in Section 5 along with further details of PHD.

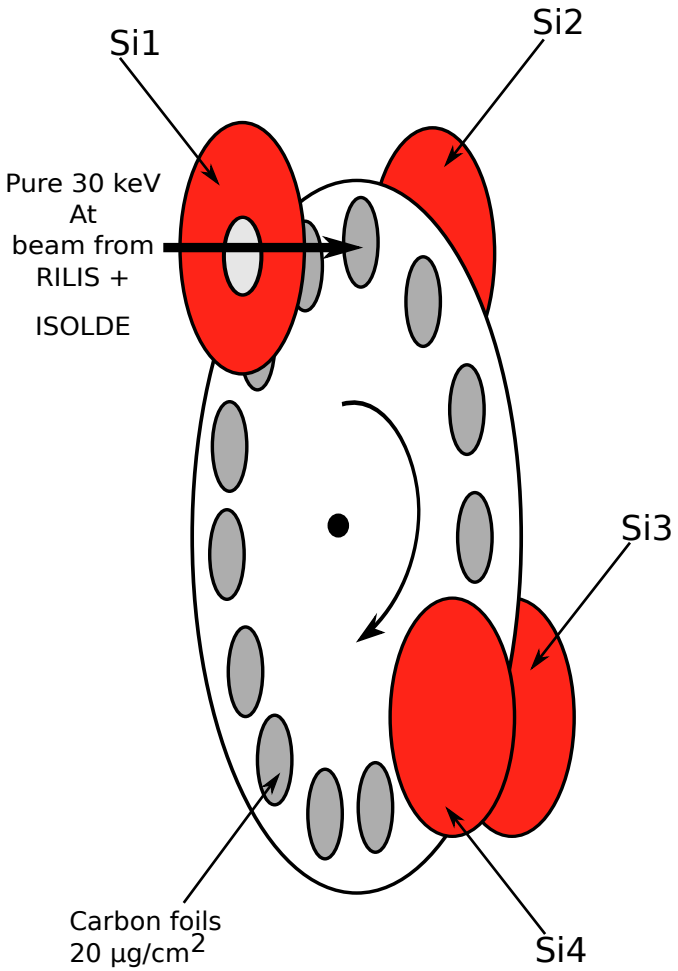

Figure 3.11: The positioning of the four silicon detectors within the chamber and their positioning relative to the wheel and each other, adapted from [30] by [112].

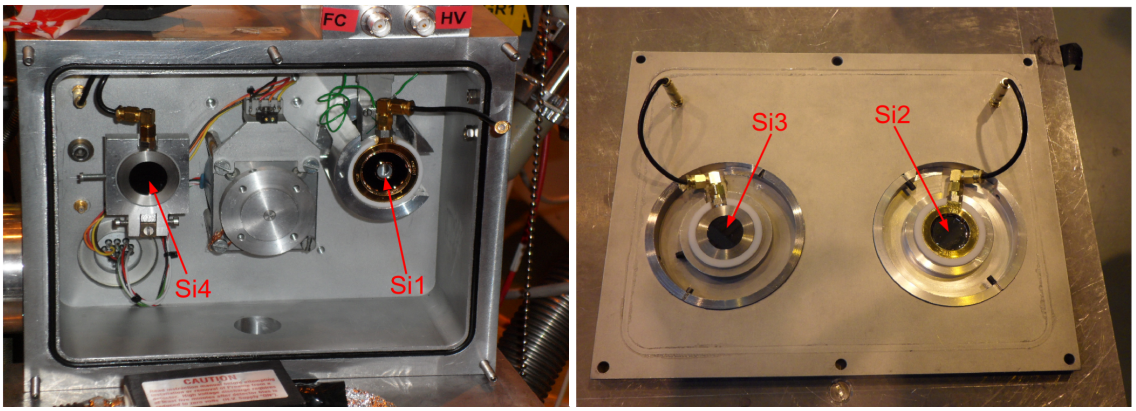

(a) Silicon detectors Si1 and Si4 (b) Silicon detectors Si2 and Si3

Figure 3.12: Picture (a) shows the Si1 surface barrier detector on the right, and the Si4 PIPS detector on the left. Picture (b) shows surface barrier Si2 detector on the right and the Si3 PIPS detector on the left.

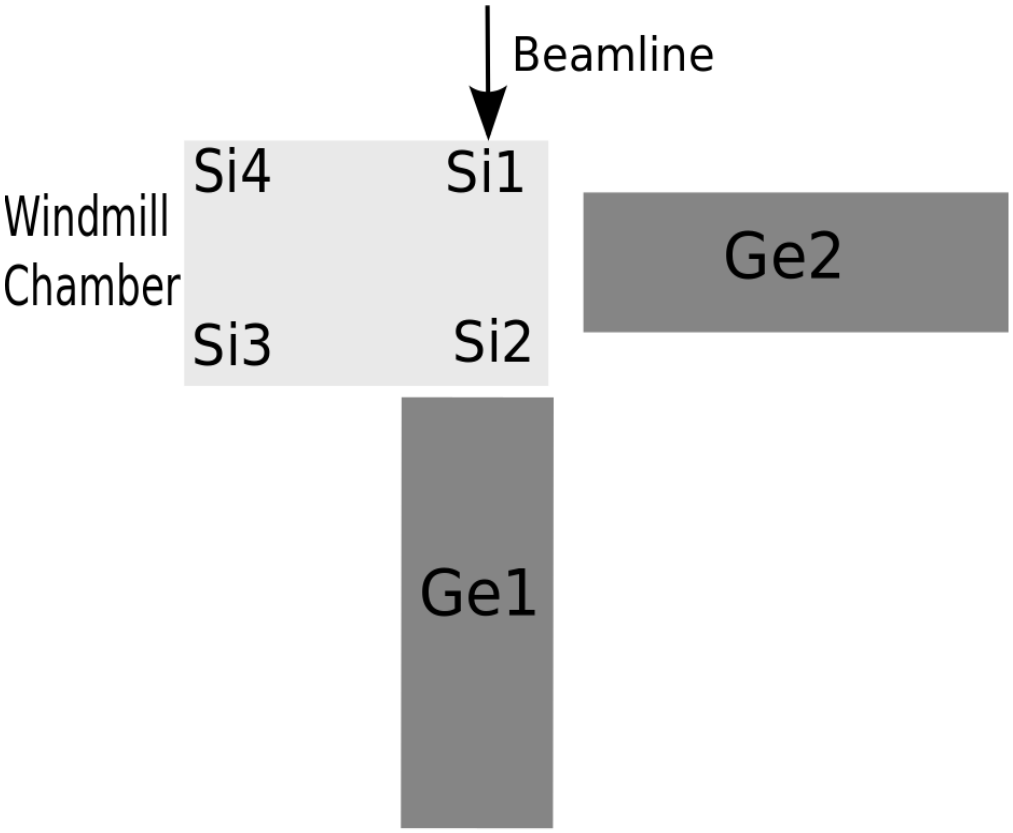

Figure 3.13: A simple diagram of the arrangement of the HPGe detectors in relation to the beamline, Windmill chamber and silicon detectors.

3.2.2 Electronics

Digital electronics were employed for both experimental runs. Nine Digital Gamma Finder (DGF) modules were available of which eight were utilised at a time, leaving one spare module. The modules are numbered from 0 to 8. In the 2011 run, modules 0 - 7 were used, but due to problems with module 7 in 2012 it was replaced with module 8. The layout of the modules for the 2011 and 2012 experimental runs are shown in Figure 3.14a and 3.14b.

Out of the channels on the modules used for Si1-Si4 and Ge1-Ge2, only the top and bottom channels were utilised for the energy and timing respectively. Module 6 is used for the pulser and only the top channel is used on this DFG. The timing module (7 or 8) uses all four channels. To control the timing of the system, multiple clocks were used. These clocks are set depending on the number of pulses in the supercycle and which number of pulse in the supercycle is the first to be sent to either HRS or GPS depending on the mass separator used. The main clocks utilised are listed below with the method by which it was set.

- DAQ Delay: (first proton pulse number to be sent to HRS or GPS -1) x 1200 ms + 834 ms. The 1200 ms is the time between successive proton pulses in the supercycle and the 834 ms represents the signal time from being received to being transmitted to the recording equipment.
- Windmill: number of proton pulses in the Supercycle x 1200 ms - 1100 ms - 100 ms. The 1200 ms is the time between successive proton pulses as set for the DAQ Delay . The 1100 ms is the time taken for the Windmill to turn, and the extra 100 ms is there to make sure it has turned.
- DAQ Ready: This is the time of the Windmill clock - 100 ms. This ensures that no collecting happens while the Windmill is still turning.
- Beam Gate: Same as the DAQ ready clock.

By using these clocks the data acquisition can be triggered to start at the beginning of the delayed SC, determined by the DAQ Delay clock. The system is also connected to a beam gate in the ISOLDE control room, which provides a time signal for the time between the proton pulse and when mass separator is able to send the beam to the set-up [58]. There are also auxiliary timers for the Proton Pulses and Supercycle.

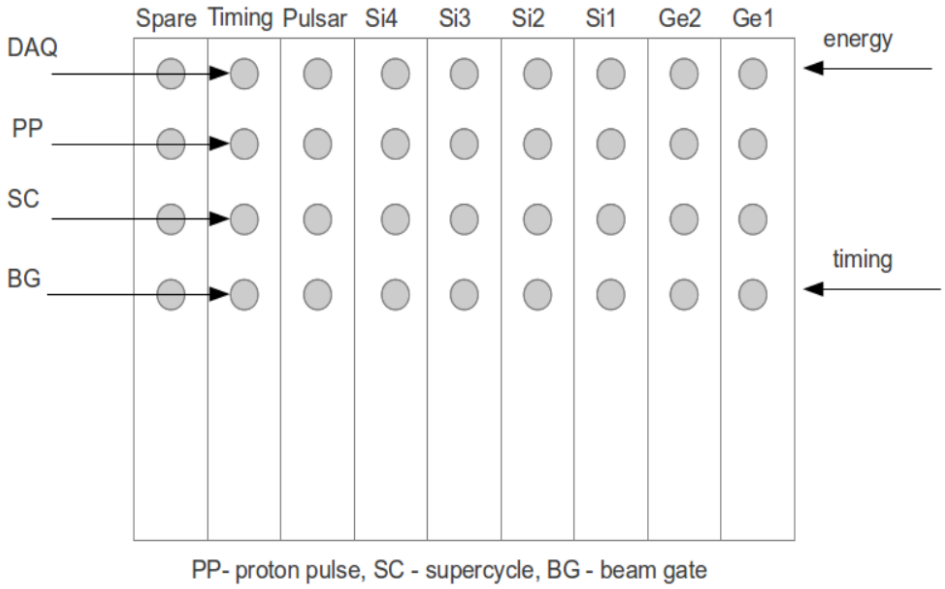

(a) DGF set-up for the 2011 run

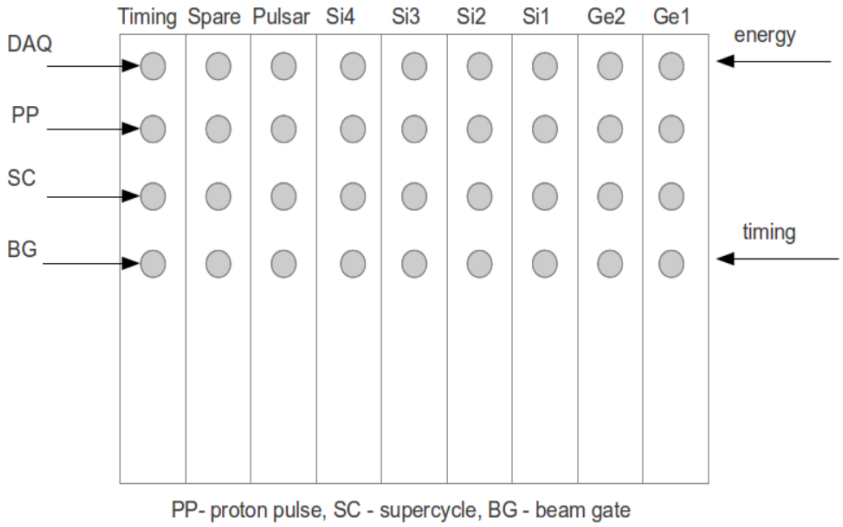

(b) DGF set-up for the 2012 run

Figure 3.14: Order of the DGF modules in 2011 (a), and (b) order of the DGF modules in 2012.

Chapter 4

Analysis of HRS Data

4.1 Calibration of the α- and γ-Decay Spectra

In this section the method by which the α and γ spectra were calculated is detailed. In Chapter 5 the calibration specific to fission will be discussed. Any calibration methods discussed in this chapter will be appropriate for both the 2011 (HRS) and 2012 (GPS) data unless stated otherwise.

4.1.1 α Spectra Calibration

Depending on the data being recorded, the energy range of the silicon detectors could be altered. Since in most runs fission fragments also needed to be recorded, the energy range was set from $\sim$ 200 keV to 100 MeV. In this section the calibration of the α-decay energy range (5 – 8 MeV) will be discussed, while the fission calibration is discussed in Chapter 5.

Initially the silicon detectors were set-up and roughly calibrated using a ^{241}Am source. This could not be used for the actual calibration due to the decay pattern of ^{241}Am. There are three main α decays at energies of 5485.6 keV, 5442.8 keV and 5388.0 keV. The 5485.6 keV is the strongest of the lines, but if the energy resolution of the detectors were to be above $\sim$ 30 keV then the second strongest peak (5442.8 keV) may not be resolved creating a broader peak. There is also a 60 keV γ transition in coincidence with the 5486 keV decay, which creates a conversion electron. This conversion electron can cause a shoulder in the ^{241}Am peak due to summing of the 5486 keV α particle and the conversion electron if both are registered in the same detector. The point at which the ^{241}Am source sits is offset from silicon detector, which means the calibration source is not sitting directly in line with the detector.

To calibrate the α decay spectra more precisely, the known peaks of the decay daughters of ^{196}At, ^{192}Bi (after ^{196}At α decay) and ^{196}Po (after ^{196}At β decay) were used. Both of these nuclides have well known energies of 6060(5) keV and 6521(5) keV, respectively [114]. Using an uncalibrated spectrum and the energy values of these peaks, the spectra were calibrated by assuming a linear relationship between the energy E, the channel number Ch, the gain A, and the offset B to give;

$$E = A \times Ch + B \tag{4.1}$$

. In this case, it was possible to find the gain value A, by calculating the 'gradient' between the two well known peaks. This could be done by using the noted variables to give,

$$A = \frac{E_2 - E_1}{Ch_2 - Ch_1} \tag{4.2}$$

, where E_1 and E_2 are the quoted energies of the α decay peaks, and Ch_1 and Ch_2 are the centroid channel numbers of the uncalibrated spectra. By rearranging Eqn. 4.1.1 and substituting in the values of A, E and Ch for one of the peaks the offset can be calculated using;

$$B = E - (A \times Ch) \tag{4.3}$$

. The calculated A and B values were then entered into the analysis code to be able to calibrate all of the data files. This process had to be repeated while working through the data files due to the calibration shifting as the runs progressed.

The α decay energies were determined using the first set of ^{196}At files that were obtained in May 2011 (containing 13 files). The resulting fitted spectrum is shown in Fig 4.1 where all 13 of the run files have been used to increase the statistics. The plot (b) in Fig. 4.1 shows the error on the fit as,

$$\text{residual} = \frac{(\text{number of counts} - \text{number in fit})}{\sqrt{\text{number of counts}}} \tag{4.4}$$

. Two methods were trialled for fitting the spectra. The first was using an interactive program, whereby the peaks were identified by selecting the limits by clicking on the plot. The background of the plot was also selected in this manner. The peaks were then fitted with a Gaussian function using these limits and the selected limits of background. This allowed the background to be taken into account

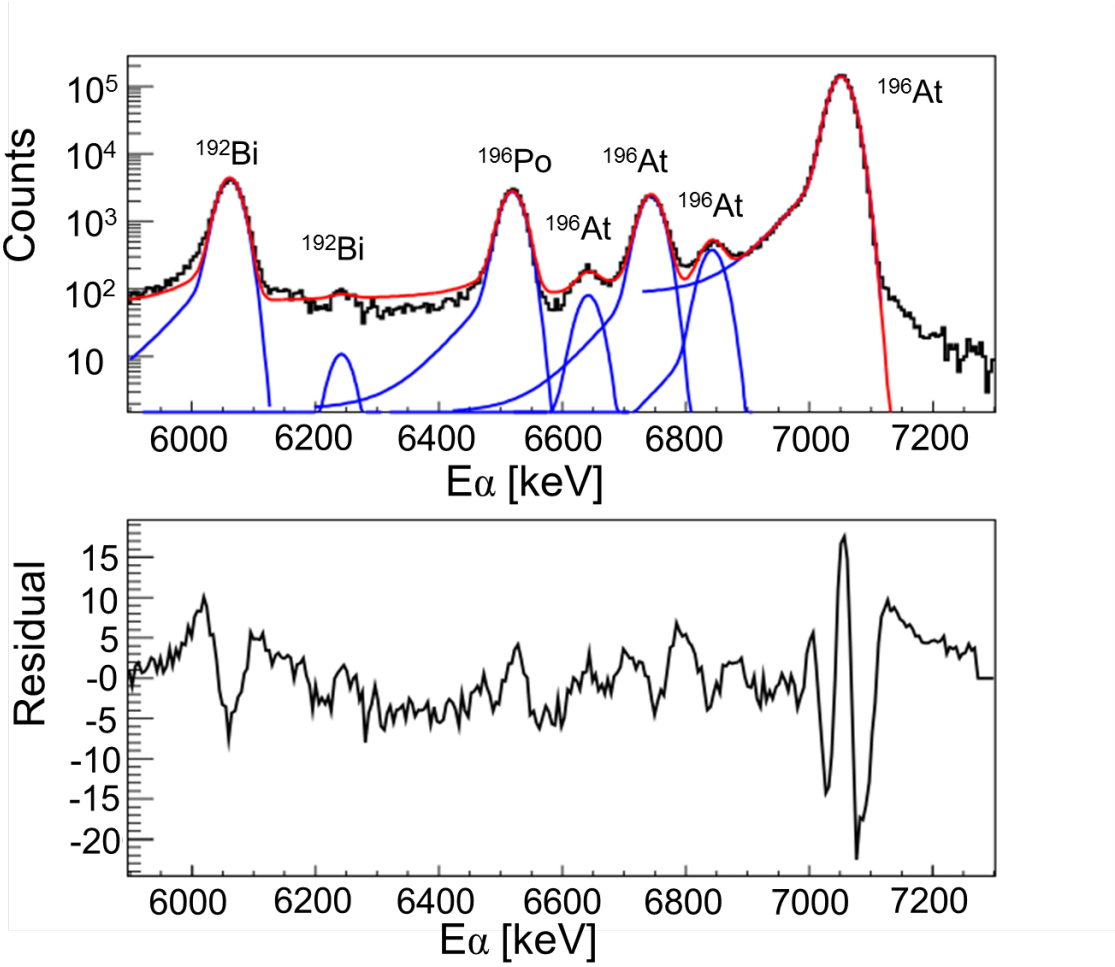

Figure 4.1: α-decay energy spectrum for ^{196}At taken at HRS showing the tails fitting procedure that was used. This spectrum uses all 13 run files from the first set of data files. A similar plot is shown in Fig. 6.1 (b), but for only the first 6 run files as will be explained.

with the fit. The information obtained from using this method included the centroid value, FWHM and content of the peak. The second method, and the one which was used to determine the energy of the peaks, was a called a tails fit. In this method, the limits of the peaks were inputted as part of a code, along with the limits for a boundary background region. In this fit however, the tails of the α decay peaks are also taken into consideration. This accounts for the shape of the peak and an overlap that is seen between peaks. The fit therefore provides a more accurate representation of the shape of the peak. The second fit is demonstrated in Fig. 4.1. Using the fitted spectrum information, a plot was produced to detail the energies of the peaks as found by the HRS runs, see Fig. A.1 in Appendix A. Again, in this instance, all 13 files and the data from Si1 and Si2 were used.

4.1.2 γ Calibration

To calibrate the HPGe detectors, standard calibration sources were used to produce calibration spectra. Four calibration sources were used, ^{137}Cs, ^{60}Co, ^{133}Ba and ^{152}Eu. Using the standard source spectra, the HPGe detectors were calibrated using a similar method to that described above.

4.2 Efficiency of the silicon detectors

The efficiency of the silicon detectors was calculated by V. Liberati (see [58] for details) using the Geant Monte Carlo simulation program. This gave geometrical efficiencies plots for the Si1 and Si2 detectors. Recent work by colleagues at Leuven [78] discovered that the measured absolute efficiencies were lower by a factor of 2. However the absolute value of the Si detector efficiency is not used in the derivation of the branching ratios in this work, see Section 6.3. In order to determine experimentally the absolute efficiency the following method was used. ^{241}Am has the advantage of being an α emitter (used to calibrate the silicon detectors) and emits a 60 keV γ-ray (can be used for the HPGe detectors). Therefore to calculate the absolute efficiency the ratio was taken between the number of $\alpha-\gamma$ coincidences and the number of γ counts. This gave efficiencies of $\sim$ 9(1) % for Si1 and 15(1) % for Si2.

4.3 Efficiency of the HPGe Detectors

To determine the absolute photopeak efficiency of the HPGe detectors to different γ ray energies, the efficiency of the each of the γ rays emitted by the standard calibration sources was calculated. These were then plotted to produce an efficiency curve. An experimental data point was also plotted using the ^{192}Bi 184 keV γ ray. The efficiency was calculated from;

$$\epsilon_\gamma = \frac{N_\gamma}{N_{\gamma,tot}} \tag{4.5}$$

, where N_γ is the number of counts seen and $N_{\gamma,tot}$ is the total number of γ-rays emitted. To determine N_γ the number of counts is taken from a fit of the peak in the spectrum. To calculate the total number of γ-rays emitted $N_{\gamma,tot}$, the activity of the source needed to be calculated for the date when the data was collected. A correction was applied to account for the time that had passed between the source being produced and calibrated at the factory and being used at the experimental run. The original and calculated activities are given in Table 4.1. Using the calculated values, the activity of each of the γ-rays from the sources were corrected for their branching. The efficiency for the experimental data point was calculated from,

$$\epsilon_\gamma = \frac{N_{\alpha\gamma}}{N_\alpha}(1 + \alpha_{total}) \tag{4.6}$$

, where $N_{\alpha\gamma}$ is the number of $\alpha - \gamma$ coincidences, N_α is the number of counts in the related α-decay peak and α_{total} is the conversion coefficient taken from [72].

The calibration curve produced is shown in Fig. 4.2. This graph includes a point calculated from the 184 keV γ transition of ^{192}Bi, as the multipolarity of this transition is already well known. This multipolarity and the calculation of those for ^{196}At transitions will be discussed further in Section 6.3.1.

As can been seen from Fig. 4.2, some of the points do not sit where expected. This graph has been constructed from different calibration source sets which are indicated by the different coloured points.

4.4 Analysis Code

The data were collected as .bin files which were converted to .root files through the use of a C++ analysis code. The code was originally developed by a previous member of the collaboration then further developed by V Liberati [58]. The use

Table 4.1: List of γ-ray calibration sources used. The activities were calculated for the date of the May 2011 experiment as the γ data is only from that experiment.

Source	Original Activity [kBq]	Run Activity [kBq]	Half-Life [years]	γ transitions used [keV]
^{60}Co	2.1	1.2	5.27	1173, 1332
^{152}Eu	11.8	9.5	13.53	122, 245, 344, 367, 411, 444, 489, 587, 689, 779, 868, 965, 1087, 1113, 1409
^{137}Cs	22.42	20.4	30.07	662
^{133}Ba	11.6	8.8	10.55	81, 276, 303, 356, 384

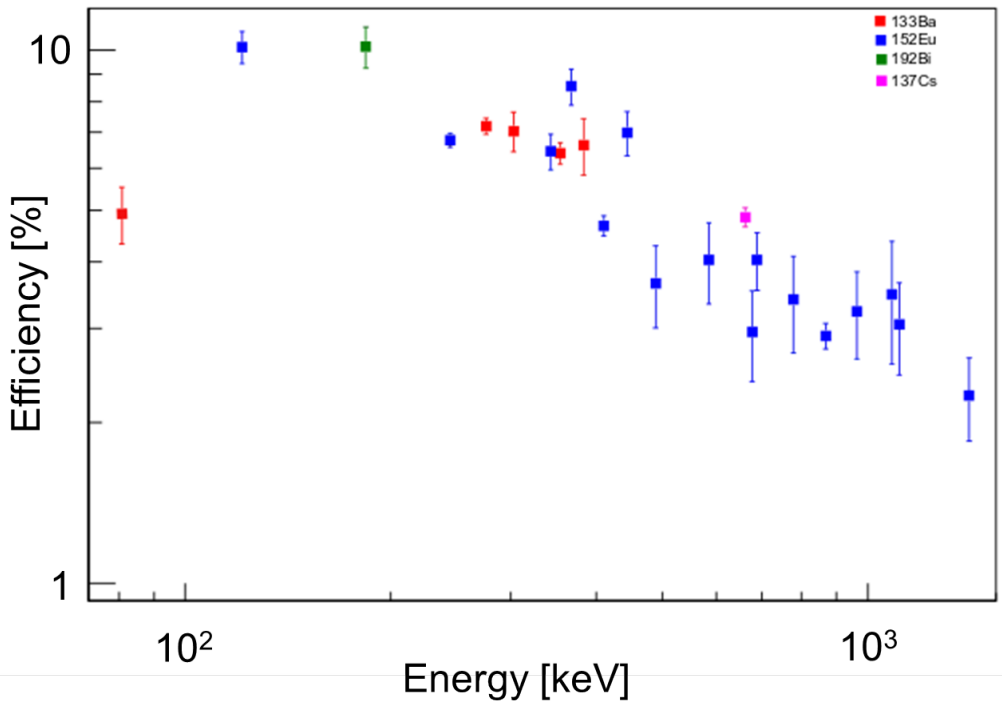

Figure 4.2: Resultant efficiency curve from plotting the efficiencies of the main γ transitions of the different calibration sources.Four calibration sources were used as indicated by the different colours. The four sources were a combination of three standard sources, ^{133}Ba, ^{152}Eu and ^{137}Cs and an experimental data point from ^{192}Bi.

of this code allowed all analysis to take place and produce all the relevant spectra. Any required modifications to the code were made by the author of this thesis.

4.4.1 Rassmussen Code

To calculate the α-decay reduced widths, a Fortran 90 code was utilised. The code is based on the work by Rassmussen [67, 115]. The code was modified to take account of branching, and the intensity of the particular α decay. The modification to the code was carried out as part of this PhD work. The new version of the code will now be used for the calculations of reduced α- decay widths from all future data.

Chapter 5

Schmitt Calibration for Fission Events

As was mentioned in Section 3.2.1, silicon detectors suffer from an effect called Pulse Height Defect (PHD) when detecting high mass particles like fission fragments. PHD is the difference in energy between the actual energy of the incoming (in this case) fission fragment, and the energy registered by the detector when calibrated using α particles. There are three main contributors to the energy loss in PHD.

The first, is the energy loss by the fragment as it passes through the entrance window or dead layer of the detector. The amount of energy lost will be dependent on the thickness of the entrance window or dead layer. The second reason is that the fission fragments travel at lower velocities near the end of the track, which means nuclear collisions become important. These lead to recoil nuclei, which also have low velocities, reducing the probability of electronic collisions occurring. This reduces the efficiency of electron-hole pair production, which in turn, reduces the energy collected by the detector (known as non-ionising collisions). Linked into these reasons, and therefore rate, of energy loss is the stopping power of the medium. This can be described by the Bethe-Bloch formula normally given as,

$$-\frac{dE}{dx} = \left(\frac{ze^2}{4\pi\varepsilon_0}\right)^2 \frac{4\pi Z\rho N_A}{Am\upsilon^2}\left[\ln\left(\frac{2m\upsilon^2}{I}\right) - \ln(1-\beta^2) - \beta^2\right] \tag{5.1}$$

, where $\frac{dE}{dx}$ is the rate of energy loss per unit length, $\upsilon = \beta c$ the ion velocity, ze the electronic charge, m is the mass of the electron, N_A Avagadro's number, A and Z the atomic mass and atomic number of the material, and ρ the density of the stopping material [6]. For particles with velocities much less than β then the formula can be simplified to,

$$-\frac{dE}{dx} = \left(\frac{ze^2}{4\pi\varepsilon_0}\right)^2 \frac{4\pi Z\rho N_A}{Am\mathrm{v}^2}\left[\ln\left(\frac{2m\mathrm{v}^2}{I}\right)\right] \tag{5.2}$$

, where the symbols have the same meaning, except now v is used to indicate the particles velocity. Thirdly, it is expected that there is a high rate of electron-hole recombination in the plasma that is created along the fission fragment track. This effect should be reduced by an increase in bias voltage, however this has a limit or electrical breakdown of the detector can occur. Therefore by creating a high electric field, this should help minimise this third contributor [110]. This means that it is not possible to perform a linear calibration similar to the one used for the α particles. A particular method for calibration was therefore developed by Schmitt *et al.* [116], and further improved upon by Weissenberger *et al.* [117].

As seen in Section 4.1.1, typically the calibration equation can be written in the form,

$$E = C_1 x + C_2 \tag{5.3}$$

, where x is the pulse height, E is the energy and C_1 and C_2 are constants. There is still a linear relationship for the fission fragments, but now that relationship leads to a mass dependence on the constants. The equation can be re-written as,

$$E = (a + a^{'}M)x + b + b^{'}M \tag{5.4}$$

, where, like in Eqn. 5.3, x is the pulse height and E is the energy. In Eq. 5.4, the constants a, $a^{'}$, b, and $b^{'}$ relate to the detector itself and M is the mass of the ion. In order to calculate this set of constants, the mean pulse heights of light and heavy fragments from a reference fission fragment spectrum are used [28]. In order to calculate these values Weissenberger defined them as [117]

$$a = A/(P_L - P_H) \tag{5.5}$$
$$a^{'} = A^{'}/(P_L - P_H) \tag{5.6}$$
$$b = B - aP_L \tag{5.7}$$
$$b^{'} = B^{'} - a^{'}P_L \tag{5.8}$$

. The constants A, $A^{'}$, B and $B^{'}$ are specific for a fissioning isotope. Values were calculated for these constants by both Schmitt *et al.* [116] and Weissenberger *et*

al. [117]. New values were calculated by L. Ghys and were listed in a collaboration report [118].

The calibration was performed at the Institut Laue-Langevin (ILL) in Grenoble. In this case, fission fragments from the ^{235}U(n,f) reaction were used. The fission fragments can then be separated using their mass-to-charge ratio (A/q) and their energy-to-charge ratio (E/q) [118].

However, both the energy and mass of the fragments are not known in Eqn. 5.4. In order to solve this, extra equations are needed to form a system of equations. To do this, the mass and momentum conservation laws are used. This gives the equations:

$$E_1 = (a_1 + a_1^{'} m_1)x_1 + b_1 + b_1^{'} m_1, \tag{5.9}$$

$$E_2 = (a_2 + a_2^{'} m_2)x_2 + b_2 + b_2^{'} m_2, \tag{5.10}$$

$$m_1^* E_1^* = m_2^* E_2^*, \tag{5.11}$$

$$A_f = m_1^* + m_2^* \tag{5.12}$$

, where the subscripts 1 and 2 represent the Si1 and Si2 detectors, the * represents the values before any neutron emission and A_f is the mass of the fissioning nuclide [28]. Using this method only coincident fragments can be used, as the values need to be inserted simultaneously into the above equations. The energy and mass values before and after possible neutron emission are related. This relationship is formed from the energy losses that the fragment will experience. This allows the initial energy (E_i^*) and mass (m_i^*) as;

$$E_i^* = E_i + \Delta E_{i,\mu} + \Delta E_{i,cf} + \Delta E_{i,dl}, \tag{5.13}$$

$$m_i^* = m_i + \mu_i \tag{5.14}$$

, where $\Delta E_{i,\mu}$ is the energy taken away by neutron emission, $\Delta E_{i,cf}$ is the energy lost in the carbon foil and $\Delta E_{i,dl}$ is the energy lost in the dead layer of the detector. This value is already taken into account in the previous calibration constants if the fragments are detected at the same angle as where the constants were calculated. To calculate the energy that is lost to any neutrons, the method by Balagna *et al.* [119] was implemented by Elsevier *et al.* [28], giving the set of equations;

Table 5.1: Parameters used in the Schmitt calibration of the silicon detectors. The i subscript means either Si1 or Si2.

Variable	Si1	Si2
$a_i^{'}$	1.647 x 10^{-6}	1.705 x 10^{-6}
$b_i^{'}$	0.036	0.032
a_i	1.576 x 10^{-3}	1.559 x 10^{-3}
b_i	-0.57	-0.29
A_f	196	
($\Delta E_{i,cf}$	0.3 MeV	1.1 MeV)
ΔE_i	1.1 MeV	1.9 MeV
F_i	1	1

$$E_i^* = (a_i/F_i + a_i^{'} m_i^*)x_i + b_i/F_i + b^{'} m_i^* + \Delta E_{i,cf}/F_i + \Delta E_{i,dl}/F_i, \tag{5.15}$$

$$0 = m_2^* E*_2 - m_1^* E_1^*, \tag{5.16}$$

$$A_f = m_1^* + m_2^* \tag{5.17}$$

, where $F_i = 1 - \mu_i/m_i^*$. If $F_i = 1$ is assumed, then m_i^* becomes the solution of a quadratic equation of the form;

$$A{m_i^*}^2 + Bm_i^* + C = 0 \tag{5.18}$$

, where A, B and C are given by;

$$A = a_1^{'} x_1 + b_1^{'} - a_2^{'} x_2 - b_2^{'}, \tag{5.19}$$

$$B = a_1 x_1 + b_1 + a_2 x_2 + b_2 + 2A_f a_2^{'} x_2 + 2A_f b_2^{'} + \Delta E_{i,cf} + \Delta E_{i,dl}, \tag{5.20}$$

$$C = -A_f(a_2 x_2 + a_2^{'} A_f x_2 + b_2 + A_f b_2^{'}) \tag{5.21}$$

. Due to the complexity of the equation, a program was written in order to solve these equations and produce calibrated fission spectra. This still required the calculation and input of all the variables. The code, however, was modified from the layout of equations given in [28]. Instead of explicitly stating the energy lost to any neutrons, the terms for the variables B and C were each divided by F_i. Table 5.1 shows the variable values that were inputted for each detector.

The $b_i^{'}$ and b_i are calculated values pertaining to the detectors themselves and

were calculated from the experiments at ILL. The $a_i^{'}$ and a_i value were calculated using both information from ILL and the α calibration value from these experiments. This can be represented as;

$$A_{IS534} = \frac{a_{IS534}}{a_{ILL}} \tag{5.22}$$

, where A is equivalent to a_i and A$^{'}$ can be calculated in the same manner which then represents $a_i^{'}$. The x_i values are not included in the table as they were extracted by the program. The values for the carbon foils and ^{196}At were calculated by S. Sels [120] using the SRIM program. The astatine ions are implanted into the carbon foils, which are 20 $\mu g/cm^2$, or 888 Å, thick. The SRIM calculation was re-run as part of this work with the implantation depth shown in Fig. 5.1.

The energy loss relevant to each detector is different due to the depth of foil the fission fragments need to escape from. An energy loss therefore had to be calculated separately for each detector. As the ion of interest, ^{98}Mo is used as this represents the symmetrical fission fragment from ^{196}Po. The energy value used is $\sim$ 74 MeV as this represents half the average TKE. This results in energy loss values of 0.3 MeV for the fission fragments travelling towards Si1 and 1.1 MeV for fission fragments travelling towards Si2.

To calculate the actual energy that was lost, the sum of all sources of energy loss was taken to give total values of 1.1 MeV and 1.9 MeV for Si1 and Si2 respectively [121]. These values were used in the final calculations.

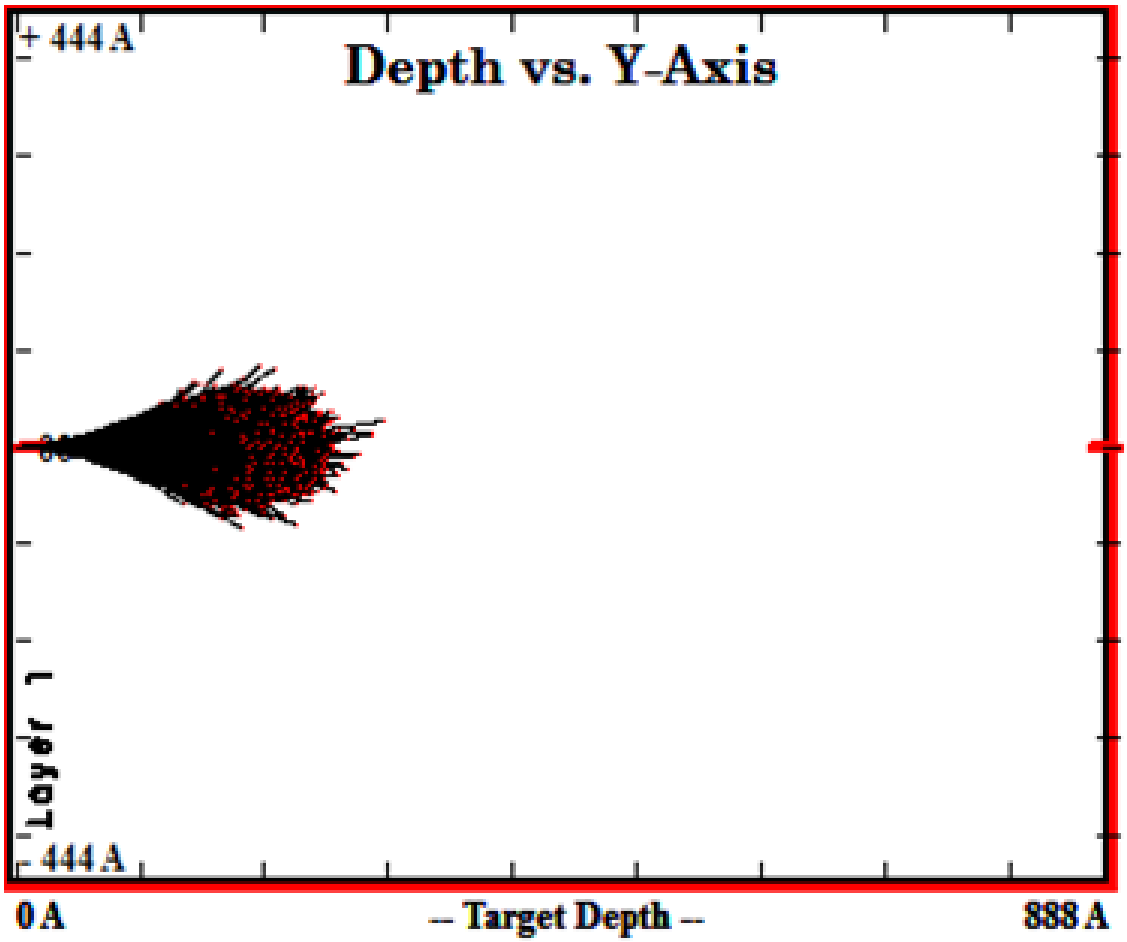

Figure 5.1: SRIM calculation of the implantation depth of the astatine ions. This shows how far the fission fragments will need to travel to escape the carbon foil, and therefore how much energy they will lose.

Chapter 6

α Decay Results of ^{196}At

6.1 Alpha Decay

In comparison to the data of HRS, approximately 50 times more α decays of ^{196}At were collected in Experiment II at GPS but the quality of data and extracted information is very different. As will be shown below, due to the availability of HPGe detectors and the much cleaner spectra obtained during the HRS experiment, experiment I data were used in the data analysis for fine-structure α-decay studies and for the deduction of the α and β-branching ratios for ^{196}At. The GPS data however, being more abundant, was used for the βDF investigation. A summary of the HRS and GPS experiments are given in Table 6.1, while further details of the calibrated spectra can be found in Section 4.1.1 and Appendix A.

Figs. 6.1(a,b) show part of the energy spectra measured in Si1 and Si2 for the GPS and HRS runs, respectively. As seen in Fig. 6.1(a), there is mass contamination from the α decays of the heavier $^{197-201}$At isotopes. In this spectrum only the main peak of ^{196}At (6.22×10^7 counts) is seen, with no fine structure decays visible. This is due to the lower mass-resolving power and, possibly, a non-optimal GPS tuning in Experiment II. Despite being strongly suppressed by GPS, these masses still weakly leaked through the separator due to their much larger production yields in comparison with ^{196}At. In contrast to this, due to the higher resolving power of HRS and the use of extra slits in the respective beam line of ISOLDE, these contaminants are fully absent in the experiment at HRS, see Fig. 6.1(b), which corresponds to 30 min of data collection when the HPGe detectors were connected. As will be seen, only the α decays of ^{196}At, and of its daughter products, ^{192}Bi (after α decay) and ^{196}Po (after β decay) are present.

Table 6.1: Summary of the overall experiment parameters for the two experiments. These give the average α rate in each detector and the fission fragment rate also. The Ge detector column at the end indicates whether there were HPGe detectors connected or not.

Nucleus	Year and Separator	Si1 α rate (s^{-1})	Si2 α rate (s^{-1})	No. of FFs in Si1	No. of FFs in Si2	FF rate Si1 (h^{-1})	FF rate Si2 (h^{-1})	Measured time (h)	Ge Det
^{196}At	2011 (HRS)	55.2	96	5	9	0.95	1.7	5.28	part
^{196}At	2012 (GPS)	175.4	322.8	96	188	2.8	5.5	34	no

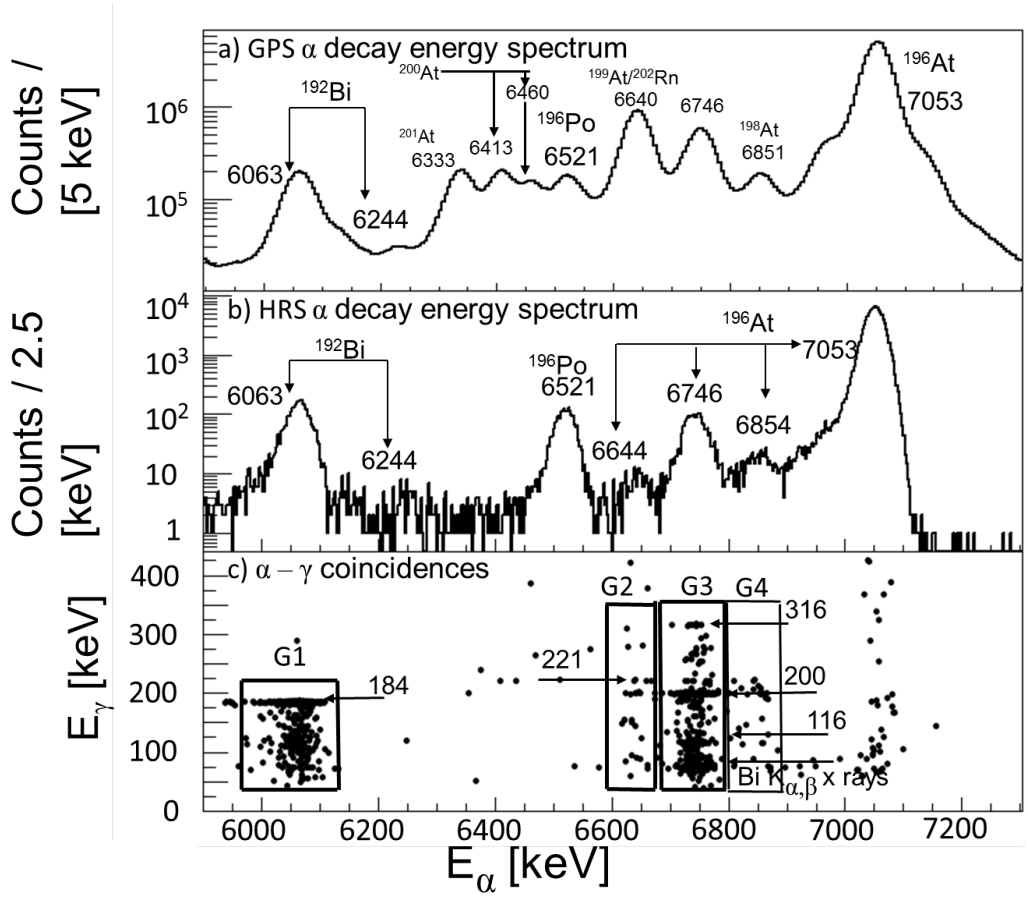

Figure 6.1: (a) Part of the α-decay spectrum measured in the GPS experiment and summed from the Si1 and Si2 detectors. The peaks are marked with their energies (in keV) and isotopes they belong to. (b) The same for the HRS experiment, but only a part of the data collected during ∼30 min is shown, for which respective coincidence α-γ data are also available and shown in panel (c), see text. (c) The prompt $\alpha - \gamma$ coincidence plot for the α decays from (b), measured within the time interval of 600 ns.

Fig. 6.1 (b) clearly shows seven α-decay peaks including the main 7053(9) keV peak (which has been mentioned in past literature see Section 1.3.2), and a previously identified fine structure peak. This has an energy value of 6746(9) keV and has been seen recently in a study by Kalaninovà [48]. The other two peaks however were previously unobserved. They have energies of 6644(11) keV and 6854(9) keV and are attributed to the fine structure decay of ^{196}At as will be shown. Also present on the plot are the β decay daughter ^{196}Po at 6521(9) keV and the α decay daughter ^{192}Bi at 6063(9) keV and 6244(10) keV. The intensities of the peaks were also cal-

Table 6.2: A comparison of α-decay energies E_α, half-life values $T_{1/2}$ and deduced reduced α-decays widths δ^2_α for ^{196}At from the measurements in this work and previous results.

E_α (keV)	$T_{1/2}$ (ms)	I_α (%)	$Q_{\alpha,tot}$ (keV)	δ^2_α (keV)	Reference
7055(7)	300(100)				[41]
7053(30)	320^{+220}_{-90}				[42]
7044(7)	390^{+270}_{-120}				[43]
7065(30)	253(9)				[44]
7048(5)	388(7)				[45]
7055(12)	389(54)				[46]
7047(5)	350^{+50}_{-40}				[39]
7048(12)	350^{+290}_{-110}			27(2)	[47]
7045(5)	350(90)	96(2)		29(8)	[48]
6732(8)		4(2)		17(9)	[48]
7053(9)	358(5)	97.8(1)	7200(9)	26.6(20)	this work
6854(9)	365(167)	0.26(3)	7196(9)	0.36(5)*	this work
6746(9)	343(45)	1.80(6)	7202(9)	6.3(5)*	this work
6644(11)	413(574)	0.14(3)		1.2(3)*	this work

* reduced widths were calculated by using the deduced half-life of 358(5)ms.

culated for each of the α decay peaks, and this information (along with branching) was used to calculate the reduced α widths of the peaks. A summary of these peaks and those seen in the previous studies can be found in Table 6.2.

The HPGe detectors were only connected for six of the run files. Therefore any $\alpha - \gamma$ analysis only used these files to ensure that any calculated values were not distorted, due to a larger number of α decays not corresponding to the γ counts. The HRS spectrum shown in Fig. 6.1 (b) therefore reflects this reduction in the number of files.

Unfortunately, the HPGe detectors could not be connected during the GPS run. The detectors were calibrated and set-up but it was found that the dead time was too large to obtain anything useful from the detectors. The rate on Ge1 was noted to reach 8 kHz while sitting in position. An attempt was also made to connect the detectors for the ^{194}At run but rates were still $>$ 2.5kHz and almost all the peaks were suffering from summing.

Fig. 6.1(c) shows the $\alpha-\gamma$ coincidences for the α decays from panel (b), within a 600 ns coincidence time interval. The strongest 7053 keV α decay of ^{196}At would not be expected to have any coincident events, therefore the small number of coincident events in the broad range of γ-ray energies is considered as random. Four areas of

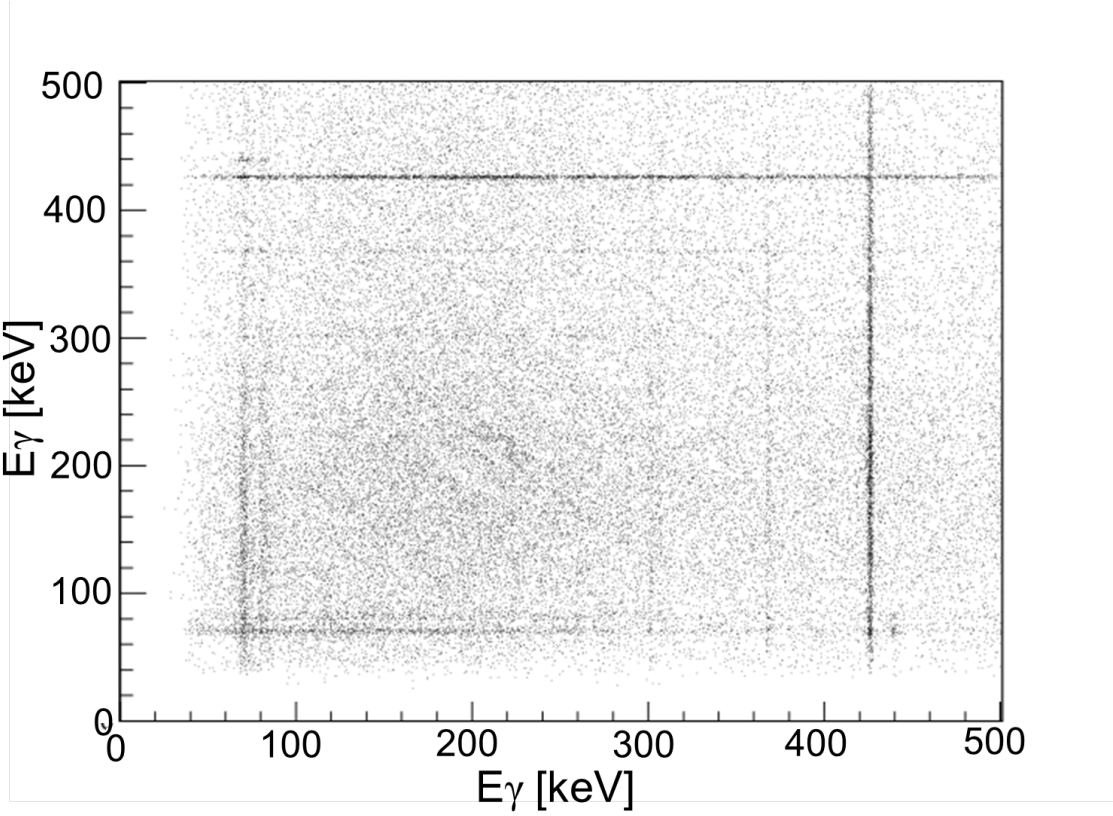

Figure 6.2: 2D $\gamma-\gamma$ matrix of Ge1 against Ge2 used to determine if any coincidences could be seen. This was drawn by plotting all events in Ge1 against all events in Ge2. Due to no time conditions being applied, this made it difficult to see any coincidences.

interest are marked by 'G1', 'G2', 'G3' and 'G4' in Fig. 6.1(c). The projections on the γ-energy axis from these three regions are shown in Fig. 6.6(a), (b), (c) and (d).

From the HRS run, a $\gamma - \gamma$ matrix was produced, as shown in Fig. 6.2. The matrix was created as a 2D histogram, by plotting the events from Ge1 against those from Ge2. Although coincidences were looked for, there were none apparent in the matrix, probably because of the low number of counts, and no timing conditions being applied. The spectrum recorded by Ge1 (directly behind Si2) is shown in Fig. 6.3. There are strong lines at energies 70.3(1), 80.3(1) keV which are likely to be X-rays, and three γ rays at energies 368.1(1), 426.1(1) and 439.6(1) keV. It is unclear which nuclides these belong to. The energies of interest are marked on the γ-ray energy spectrum where they correspond to γ ray coincidence event energies.

To reduce the number of random counts, timing conditions were applied to the coincidences. Areas of coincidences were chosen to examine the timing structure.

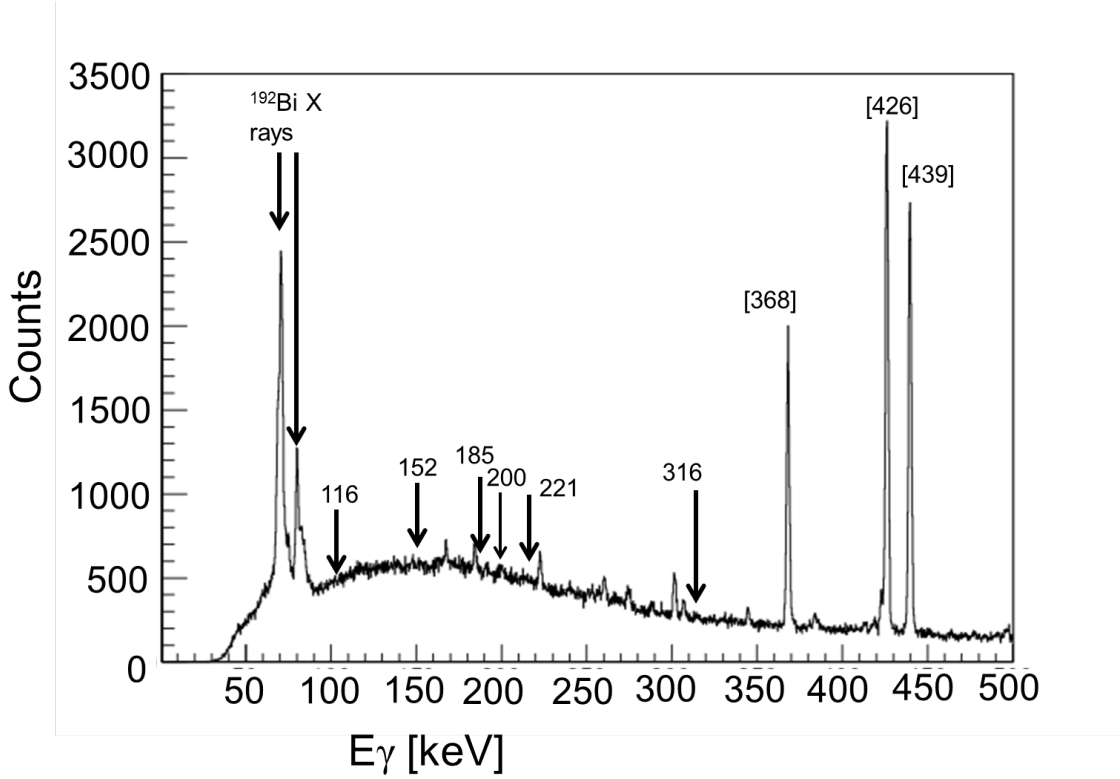

Figure 6.3: Total γ-ray energy spectrum from Ge1. Marked on the spectrum are the energies of the coincident γ transitions which are shown by the arrows. The energies in brackets are for the strong γ transitions that are present in the spectrum. The nuclides to which they belong are not known.

This was carried out to confirm if the coincidences came from γ rays or X-rays. Examples of the timing structures for each are shown in Fig. 6.4 and Fig. 6.5.

The γ ray has a well defined time structure whereas the X-ray does not. This can be seen in Fig. 6.4 and Fig. 6.5. Where the γ timing structure has a peak, showing the γ rays are prompt, the X ray structure does not have this single peak, indicating that the emission of X rays does not have the same prompt signal as γ rays. This structure could also be caused by the properties of the HPGe detectors themselves. At low energies, the timing properties of HPGe detectors for low energy events becomes worse due to the electrical field not being as defined. This is because for low energy rays, the interactions will take place near the surface of the detector. This confirmed that the low energy coincidences were X-rays. The X-rays seen are likely to be either characteristic X-rays from the lead shielding, or possibly caused by the emission of the alpha particle ionising the atom. Using these plots as a guide

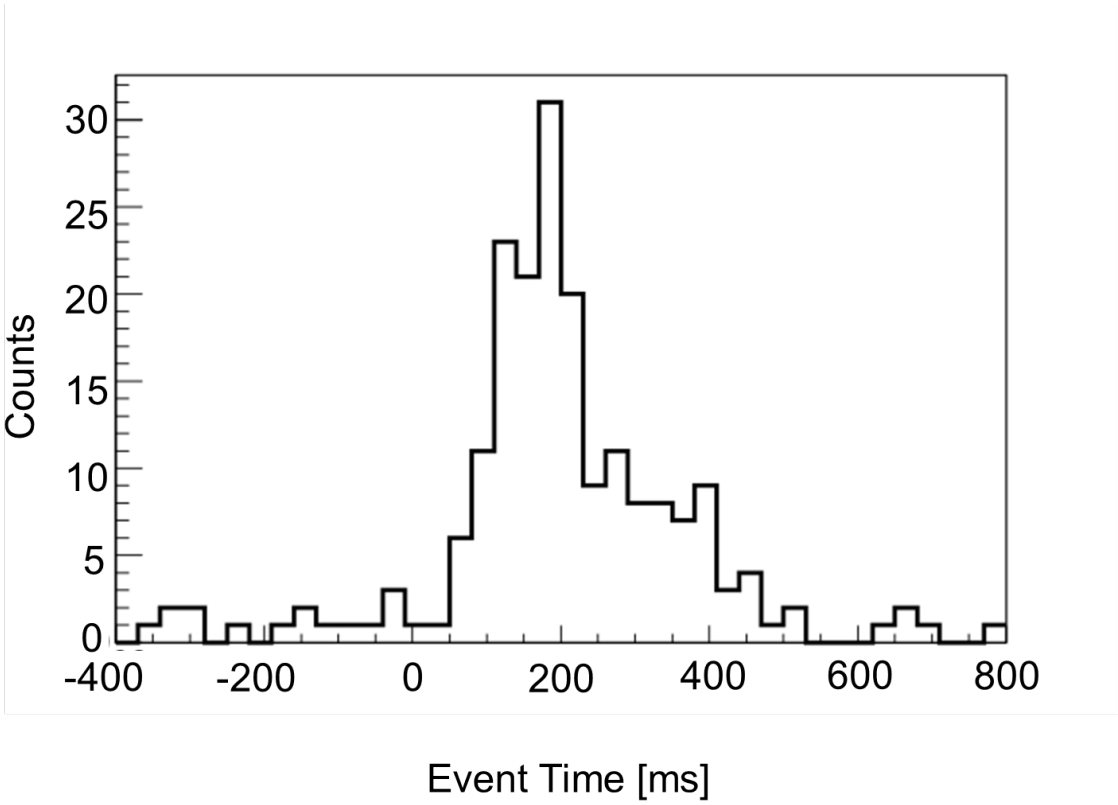

Figure 6.4: Timing structure of the γ rays associated with the fine structure peaks. It can be seen that the timing has a peak value after which the peak falls away as time increases.

it was determined that an ideal timing interval between the α particle and the γ ray was 600 ns. The differences in spectra, depending on applied time gate, can be seen in Appendix B.

Both Fig. 6.1(c) and Fig. 6.6(a) show the known coincidences between the 6060(5)-keV α decay of ^{192}Bi and the 184 keV E1 γ-ray transition in the daughter ^{188}Tl [122], see decay scheme in Fig. 6.7. As expected, no coincident events are seen for the full-energy 6244-keV α decay of ^{192}Bi. By comparing the number of ^{192}Bi single α decays in Fig. 6.1(b) and coincident 6060-184 keV events in Fig. 6.6(a), the absolute γ-ray efficiency at 184 keV was deduced as 10(1) % (see Section 4.3 for method). This value was used to normalize the γ-ray efficiency calibration curve produced with the use of the standard γ-ray sources.

Starting with the 6746 keV α decay peak, it was determined to be in coincidence with the 115.7(3) keV, 185.4(2) keV, 199.9(1) keV, 221.1(4) keV and 316.1(13) keV γ lines. For all γ transition values, the actual energy with error will be given the first

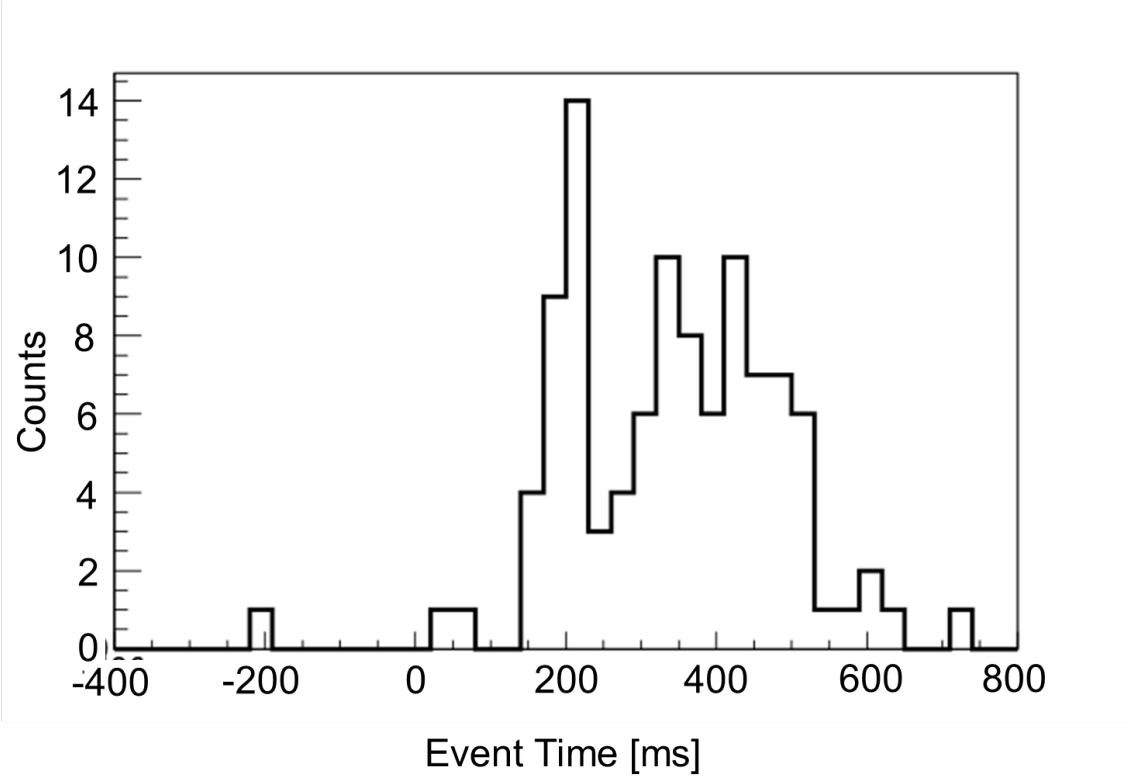

Figure 6.5: X ray timing structure of the lower energy area in coincidence with the fine structure peaks. It can be seen that the structure is not as well defined.

time it is mentioned, thereafter rounded values will be used. The coincident events of 6746 – 316 keV have a $Q_{\alpha,tot}$=Q_{α}(6746)+E_{γ}(316) value that is consistent with the 7053 keV decay. This establishes an excited state at 316 keV in ^{192}Bi. Based on the observation of the 6732(8) keV fine structure α decay of ^{196}At, the study by Kalaninová *et al.* [48] proposed the existence of the 320(10) keV excited state in ^{192}Bi. However, due to low statistics, no respective γ rays were observed. The 200 keV and 116 keV γ rays are also in coincidence with the 6746 keV decay and the γ ray energies sum to 316 keV. Therefore the 116 and 200 keV transitions are placed in a cascade parallel to the 316 keV decay, with the 116-keV γ ray feeding the 200 keV state. It can be seen in Fig. 6.6(b) that the intensities of the 116-keV and 200-keV γ rays strongly differ, which is explained by the difference in their internal conversion, after the difference in the calculated respective detection efficiencies were allowed for (relative error of 8%), see Section 6.3.1.

The weak 6644 keV α decay forms an excited state at 409(11) keV in ^{192}Bi. However, a full energy γ ray transition is not seen in this work. It is in coincidence

with the 200 and 221 keV, and tentatively with the weak 152.5(8) keV γ decays as seen in Fig. 6.6. The existence of the 200 and 221 keV coincidences, requires the presence of a 209(11) and 188(11) keV transition. These are shown as dashed lines in the decay scheme and as are yet unobserved. The 221 keV is in coincidence with both the 6644 keV and 6746 keV fine structure α decays. This fact suggests that an excited state at 221 keV should be present in ^{192}Bi, possibly feeding directly to the α-decaying state in this nucleus. This level has therefore been tentatively placed in the decay scheme in Fig. 6.7. The observation of 6746-221 keV coincidences also requires the presence of a (yet unobserved) 95 keV decay from the 316 keV state to the 221 keV state. The weak 185 keV decay was not placed in the decay scheme of ^{196}At $\rightarrow$ ^{192}Bi. The 6854 keV α decay is in coincidence with the 200 keV with a $Q_{\alpha,tot}$=Q_{α}(6854)+E_{γ}(200) value which is deemed to be in good agreement within error of the Q_{α} value of the full energy peak of 7053 keV. The 6854 keV α decay was therefore assigned as feeding the 200 keV level. The $\alpha - \gamma$ plots for each α decay are shown in Fig. 6.6(a, c, e, g). The corresponding γ projections are shown in Fig. 6.6 (b, d, f, h).

6.2 Half-lives

Different methods were used in order to deduce the half-lives of ^{196}Po and ^{196}At. As ^{196}Po has a known half-life in seconds, the decay data from the Si3 and Si4 decay detectors were used. Since there is no beam implantation at the decay detector site, any data here will only be the decay of ^{196}Po. By plotting the decay curve of the polonium, an exponential curve was fitted. The decay curve and fit are shown in Fig 6.8. The half-life was determined by using only one detector, then by plotting both detectors together. The final half-life was taken to be as ($T_{1/2}$) = 5.8(1) s which is in agreement with, but more precise, than the previous values of 5.5(5) s [123], 5.8(2) s [124] and 5.8(2) s [125].

To determine the half-life of ^{196}At, the data from HRS was used due to the contaminant products in the GPS data. From the literature, ^{196}At is known to have a half-life in the order of hundreds of ms. The astatine will therefore decay fully in the carbon foil at the position of the implantation detectors. Since there will be implantations occurring at the same time as decays, it is not possible to simply fit an exponential to the decay curve, as seen in the case of ^{196}Po. By plotting the decay of ^{196}At, it becomes apparent that the decay is a series of grow and decay peaks, that replicate the timings of the proton pulses. To find the half-life the

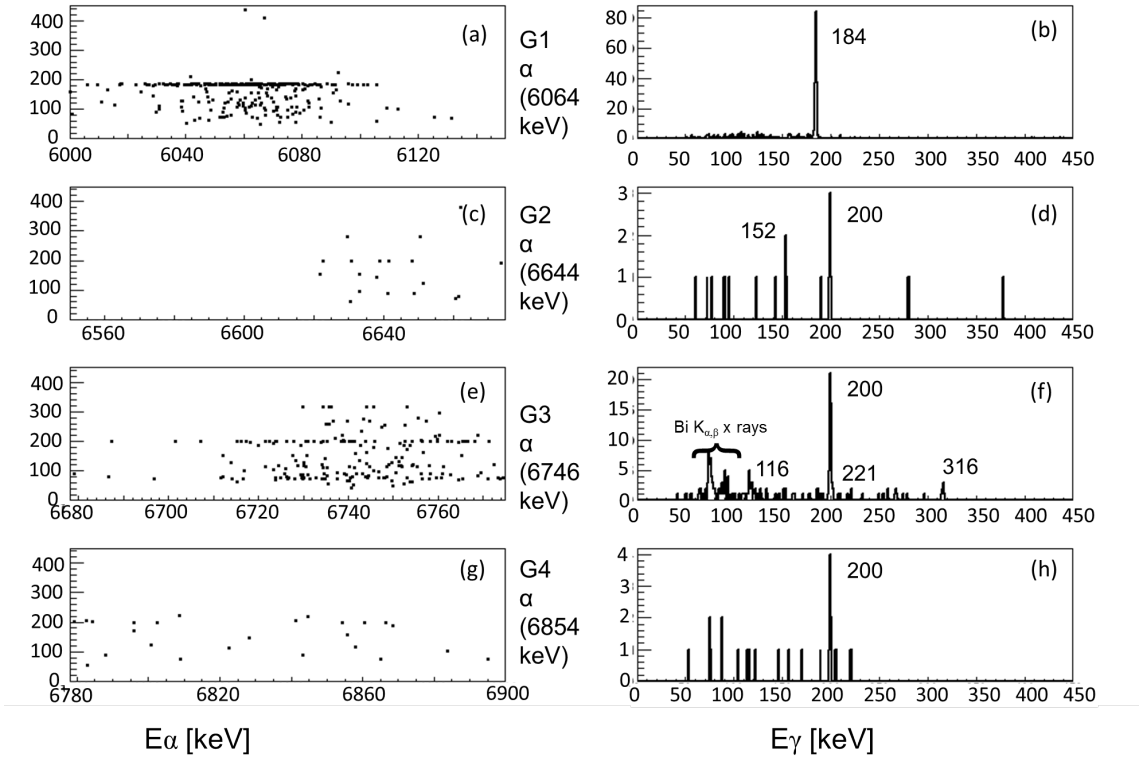

Figure 6.6: Comparison of the $\alpha - \gamma$ coincidences and γ projection of ^{192}Bi and the three α decay fine structure peaks.

Table 6.3: Half-life values for each of the α decay peaks.

Energy keV	Time window of peak (16-23) ms	(28-40) ms	Average Time ms
6644	427(296)	400(852)	413(574)
6746	341(47)	345(45)	343(45)
6854	389(169)	342(164)	365(167)
7053	357(5)	359(5)	358(5)
total	356(6)	360(5)	358(5)

'grow and decay' method therefore needs to be used, as fully described in [29]. As a brief overview, the 'grow and decay' method is when the structure of each proton pulse peak is drawn. It is the shape of this peak that gives the method its name. As implantation is occurring, then the peak grows from the alpha events being recorded. Once implantation stops, then only the decay curve remains until the next proton pulse arrives. This is why there must be sufficient time between proton pulses, as otherwise, the decay curve from the previous pulse may not have fully decayed before growing again.

The timing plot produced is shown in Fig. 6.9 where the pulses are 1.2 s apart.

It can be seen that if the proton pulses are in succession, there is not enough time to fully decay before the peak grows again with the next implantation. It is therefore not possible to fit to these peaks. Instead, peaks are chosen where there is a large enough time gap to fully decay. By fitting these peaks, the half-life can be determined. The peaks can also be shifted when calculating the half-lives to give a higher number of counts in each peak. Shifting the peaks only works if the timings of groups of peak are exactly the same.

Although the half-life of the main peak in ^{196}At is taken as the overall half-life, the half-life for each of the astatine peaks was also calculated. Table 6.3 gives the values that were calculated and which peaks were used for each. The half-lives of the fine structure peaks are in good agreement with each other and previous values from the literature (if known), see Table 6.2. The overall half-life can be given as the main peak's half-life due to the dominance of this peak. The errors are higher on the smaller fine structure peaks due to lack of statistics which meant it was harder to obtain a neat fit.

6.3 Branching Ratios

In order to calculate the branching ratio, the following formula was used,

$$b_\beta(^{196}At) = \frac{N_\beta(^{196}At)}{N_\beta(^{196}At) + N_\alpha(^{196}At)} \tag{6.1}$$

, where N_β and N_α are the number of β and α decays of the relevant nuclide respectively. The number of β decays cannot be seen directly and are therefore deduced from the number of ^{196}Po α decays and the b_α of ^{196}Po. The term N_β can be re-written as,

$$N_\beta(^{196}At) = N(^{196}Po) = \frac{N_\alpha(^{196}Po)}{1 - b_\beta(^{196}Po)} \tag{6.2}$$

. To deduce these values the data from the HRS experiments were used. Although there were more counts available in the GPS data, as seen in Section 6.1, the α spectrum for the HRS data is much cleaner for determining the number of counts in the relevant peaks. Before being able to find the number of counts, files needed to be selected that had the same supercycle (SC) structure. As will be explained later, the structure of the SC needs to be considered and therefore it is not possible to use files which have different structures. On examination of the files used for the energy determination, it was discovered that only three of these files appeared to have the same structure. Only these files were therefore used for the branching.

Firstly, the total number of ^{196}At needed to be determined. This was done by fitting the four ^{196}At α decay peaks (as done in Appendix A) then taking the number of counts and associated error, and totalling the four values. By using the previous fitting method, a background is already included in the fit and therefore does not need to be calculated separately. The time over which the α-decay energy spectrum is drawn will be explained later when discussing the ^{196}Po.

Secondly, the number of ^{196}Po decays needed to be calculated. As the number of β decays cannot be measured directly, the number had to be inferred from the number of α decays of ^{196}Po seen, with multiple corrections. Since it is possible for ^{196}Po to be produced directly in this experiment, a measure of the amount of directly produced ^{196}Po was needed. This was found by running a file during which the lasers were tuned on the ionisation of astatine and with the resonant transition laser blocked. As no ^{196}Po could therefore be from the β decay of ^{196}At, any ^{196}Po decays that were seen had to be produced directly. The laser 'off' file was run for 1495s and 34(6) counts were seen, evidence indicating its direct production in the

target by surface ionisation in the ion source. Since the laser on file was run for 3503s, this number of counts needed to be scaled. With a scaling factor of 2.34, the number of directly produced counts were 80(14). This amount of directly-produced ^{196}Po was estimated as ∼0.43% of the total ^{196}Po α decays measured in the HRS run and was subtracted from the total number of counts in the ^{196}Po peak.

The ^{196}Po has a half-life of ∼ 6s. It will therefore not only decay at the implantation detector's position, but also at the decay detector's position. The number of decays in the decay detectors can be found by determining the number of counts in the ^{196}Po decay peaks. There is however a consideration to be made. When the first supercycle (SC) starts, the foil will be at the implantation position. When the supercycle ends, the wheel rotates and the foil moves to the decay position. The implanted/decay counts in Si3 and Si4 associated with SC 1, are actually collected during SC 2. This is shown in Fig 6.11.

From Fig. 6.11, it can also been seen that a similar problem will occur at the end of a run. If after a number N of SCs the data acquisition system is stopped, the decay counts from SC N will actually be in SC N + 1 which is not being recorded. To mitigate against this problem, not only did files that had the same number of SCs require to be used, but the times of the 1st, 2nd, last and 2nd last SCs needed to be found. This meant that time conditions could be placed upon the α decay energy spectrum for the implantation and decay detectors, and only the SCs where both the parts were present were plotted. This gives 2680(52) decay counts in the decay detector position. During the movement of the foil between the two positions, the ^{196}Po will still be decaying, but these decays will not be recorded. The number of 'missed' decays needs to be calculated.

Firstly, the time structure from the ^{196}Po decay in Si2 was drawn over one SC. This represented all the α decays that were seen in a particular SC. Secondly, the time structure for the ^{196}Po in Si3 was drawn on the same plot. To draw this structure however, several considerations needed to be made. Depending on which of the SC is drawn for the implantation detector, then the following SC needs to be drawn for the decay structure. The time structure will need to be time shifted on the axis as not only did the decay occur after implantation, but the time taken for the windmill to turn also needs to be included. This will give a gap between the two time structures which represents the missing counts.

In this case, the two time structures did not match and therefore a scaling factor had to be introduced. The scaling factor was deduced by fitting the beginning of the decay curve in Si3 to the end of Si2. Since the plots have been scaled, the difference

Table 6.4: The table lists the variables, with values, that were required in order to calculate the branching ratio. The manner in which each of these numbers is applied is described in the text.

	Nuclide	
	^{196}Po	^{196}At
Si2	11364(107)	535408(736)
Si3	2680(52)	
direct production (counts)	42(5)	
Si3 scaling (counts)	1076(62)	
WM movement (counts)	440(18)	
b_α	94(5)%	

in counts also needs to be accounted for. This is found by taking the difference in counts between the two integrals of the fits on Si2 and Si3. This number will be subtracted from the total. The number of counts missed by the movement of the windmill was calculated using the approximate geometry of the shape of the gap. The gap can roughly be split into a rectangle and a triangle.

The number of counts missing from the rectangle can be calculated by multiplying the number of bins in the gap along the x-axis, by the number of counts that give the height of the start of Si3. The number of counts in the triangle can be calculated by multiplying the difference in height of the end and start of Si2 and Si3 by the number of bins and halving the number. Adding these two values together will give the number of counts missed due to the movement of the windmill. The final plot that is produced is shown in Fig. 6.12.

The last correction to be considered is the branching ratio of the ^{196}Po, $b_\alpha(^{196}\text{Po})$ = 94(5)% [125]. Only the α decay of the ^{196}Po is detected which means the number of β decays of the ^{196}Po need to be calculated to have the total number of ^{196}Po. The numbers used in the branching ratio calculation are shown in Table 6.4.

Once all corrections have been accounted for, the branching ratio could then be be calculated. Firstly the total number of ^{196}At is found by totalling the integral values from all four of the ^{196}At peaks. This gives a total of $\sim$ 535000 counts. Secondly the number of ^{196}Po decays using the corrections noted above in Table 6.4 is found from,

$$\text{No. of } ^{196}Po = a - b + c + d - e \times \frac{1}{b_\alpha(^{196}At)} \quad (6.3)$$

, where a is the integral from the implantation detector, b is direct production counts, c is the integral from the decay detector, d is the movement of the windmill and e is the scaling factor for the decay detector. Therefore the branching ratio can be be calculated as,

$$b_\beta = \frac{N(^{196}Po)}{N_{total}} \tag{6.4}$$

. The experimental branching ratios of $b_\beta = 2.6(2)\%$ and $b_\alpha = 97.4(2)\%$ were deduced for the first time for ^{196}At.

6.3.1 Multipolarities

Before calculating the multipolarities of the ^{196}At γ transitions, the process was first tested using the $\alpha - \gamma$ coincidence from ^{192}Bi. This multipolarity is already well-known as an E1 [122]. The method of calculation could therefore be tested to ensure that the expected answer was found.

To calculate the multipolarities, the generic expression:

$$N_\alpha = \frac{N_{\alpha\gamma}}{\varepsilon_\gamma}(1 + \alpha_{tot}) \tag{6.5}$$

, was used where N_α is the number of α decays for a specific α line in the singles spectrum (see Fig. 6.1 (b)), $N_{\alpha\gamma}$ is the respective number of $\alpha - \gamma$ coincidences observed in Fig. 6.1 (c), ε_γ is the detector efficiency at a specific energy, and α_{tot} is the total conversion coefficient of the respective γ ray.

The γ-ray transitions that are coincident with the fine structure α decay of ^{196}At are all prompt, which limits their multipolarity to E1, M1, or E2. Based on the estimation of the total conversion coefficients α_{total}, it is possible to deduce more precisely the multipolarity for the 200, 116 and 316 keV decays.

As seen in Fig. 6.7 the 316 keV level, which is fed by the 6746 keV decay, de-excites through the cascade of 200 and 116-keV transitions and also by a weak cross over full energy 316 keV decay. This allows the intensity balance (see Eqn. 6.3.1) between the feeding 6746 keV α decay and the following de-excitation, by accounting for the coincident 116 and 200 keV decays. The latter requires that their intensities be the same after the γ-ray efficiency and internal conversion corrections are applied.

$$N_\alpha(6746) = \frac{N_{\alpha(6746)\gamma(200)}}{\varepsilon_{\gamma(200)}}(1+\alpha_{tot(200)}) + \frac{N_{\alpha(6746)\gamma(316)}}{\varepsilon_{\gamma(316)}}(1+\alpha_{tot(316)})$$
$$= \frac{N_{\alpha(6746)\gamma(116)}}{\varepsilon_{\gamma(116)}}(1+\alpha_{tot(116)}) + \frac{N_{\alpha(6746)\gamma(316)}}{\varepsilon_{\gamma(316)}}(1+\alpha_{tot(316)}) \quad (6.6)$$

. As part of the intensity balance according to Eqn. 6.3.1, the intensity of the observed Bi K-X rays in Fig. 6.6 (c), provides a further constraint on the possible multipolarities. Therefore, to deduce the total conversion coefficients (thus, multipolarities) and the possible mixing ratios for the 116 and 200 keV γ rays, the number of $N_\alpha(6746) = 1783(43)$ counts from Fig. 6.1 (b) corrected for X-ray contribution needed to be used. The corrected values for each γ ray using Eqn. 6.3.1 are given in Table 6.5.

Based on the values of $N_{\alpha\gamma}$(6746-200)=88 cts and $N_{\alpha\gamma}$(6746-116)=23 cts taken from Fig. 6.1 (b) and corrected for the relevant γ efficiencies, the total experimental conversion coefficients of α_{tot} using Eqn. 6.3.1 were calculated as $\alpha_{tot}(116)$=5.6(5) and $\alpha_{tot}(200)$=1.05(1). The comparison with the calculated total conversion coefficients from [72] as seen in Table 6.5 suggests mixing of M1+E2 for both 116 and 200 keV γ rays, with the likely mixing ratio being 50(5)% for them both. Therefore the most likely multipolarity for the 316 keV transition is likely to be E2, due to the mixing of the cascade γ rays. To show that this method is correct, the number of X-rays can be calculated to confirm that the number seen, is reproduced. In this case (since they are K X-rays) the α_k value is used instead.

6.4 Discussion

From the results found in the previous sections, a new decay scheme for ^{196}At was produced, Fig. 6.7. Although both of the long-lived states of the α daughter are shown, from the $\alpha-\gamma$ plot in Fig. 6.1 (c) it is clear that only the I^π=(3^+) α-decaying state in ^{192}Bi, resulting from the $[\pi h_{9/2} \otimes \nu p_{3/2}]$ configuration is populated. This is because only the coincident 6060-184 keV events are seen. The spin/parity states that are assigned to the ^{192}Bi are tentative values based on α decay systematics. This is fully discussed in [122].

In order to build the decay scheme, the α decay energies were taken first. From both the α decay spectra and the $\alpha-\gamma$ spectra, the main α decay peak of energy

Table 6.5: Table of the conversion coefficients for the 116, 200 and 316 keV γ transitions.

E_γ	α_{tot} (E1)	α_{tot} (M1)	α_{tot} (E2)	α_{tot} (M2)	γ_{eff}	$\alpha - \gamma$ counts	E1 counts	M1 counts	E2 counts	M2 counts
116	0.31	6.68	3.61	48.4	0.086	23	350	2054	1232.9	13211.6
200	0.08	1.42	0.45	6.81	0.101	88	941	2108.5	1263.4	6804.75
316	0.027	0.4	0.1	1.44	0.07	9	132	180	141.43	313.14

7053 keV is believed to be the ground state to ground state transition. Placing this in the decay scheme establishes the Q_α value of the system. To assign a spin to the ground state of ^{196}At, then based on the fact that the decay appears to be unhindered (δ^2_α=26.6(20) keV), then the same spin of I^π=(3^+) and configuration of $[\pi h_{9/2} \otimes \nu p_{3/2}]$ should be assigned. This assignment was also suggested in the work by Kalaninovà *et al.* [48]. The reduced width values for all of the α decays were calculated with the assumption of $\Delta L = 0$ and the results of an output file for ^{196}At are given in Appendix C.

Taking each of the fine structure α decays in turn, they, and their coincident γ rays can be placed into the decay scheme. The 6854 keV α decay is in coincidence with the 200 keV γ ray and by summing the Q_α and E_γ values, then within error, is equivalent to the full energy α decay peak. This therefore establishes an excited state at 200 keV. The 200 keV is also in coincidence with the 6746 keV, and 6644 keV α decays. Taking the 6746 keV α decay first, it has a difference from the 7053 keV peak of 307 keV. On the $\alpha - \gamma$ plot no coincidences were seen at this energy, as noted in Section 6.1 there are coincident events with a 116 keV and 316 keV. Since the 200 keV has already been placed in the scheme, the 316 keV establishes an excited state at 316 keV where both the 316 keV and the 116 keV originate. The 116 keV decays to the 200 keV state forming a cascade. There is also a 185 and 221 keV which are in coincidence with the 6746 keV α decay. The 185 keV has not yet been placed in the decay scheme due to uncertainty of where it should be. The 221 keV is also seen in coincidence with the 6644 keV. This establishes an excited state at 221 keV. If this state exists, then this requires the existence of a 95 keV transition from the 316 keV excited state. This has been tentatively added to the decay scheme.

Aside from the 200 and 221 keV γ rays, the 6644 keV was not seen to be coincidence with any other γ rays. However, the nature of the 6644 keV itself establishes an excited state at 409 keV. Therefore, a 188 and 209 keV have been tentatively placed in the decay scheme. It could also be expected that there will be a full energy γ transition of 409 keV, but this also has not been seen. The 6644 keV is also tentatively in coincidence with a weak 152 keV. This has not been placed in the decay scheme. It is hoped that with more statistics, the placing of these γ rays can not only be verified but that those which are tentative can be firmly said to be seen, and the expected γ rays are also seen.

As seen from the decay scheme, tentative spins/parities have been assigned to the excited states of ^{192}Bi. Based on the deduced γ-ray multipolarities for the 116

(M1+E2), 200 (M1+E2) and 316 (E2) keV transitions, a spin/parity of 2^+-4^+ is assigned to the 200 keV state, and a range of spins 1^{+-}–5^{+-} for the state at 316 keV. The specific choice for the 316 keV however will also depend on the value of the M1+E2 multipolarity assignment for the 116 keV decay. To assist in the assignments, the hindrance factors of the α decays that feed into these states can also be used.

The much smaller reduced α-decay width for the fine structure 6644 and 6854 keV α decays indicate their hindered nature, with hindrance factors of ∼22(6) and ∼74(1), respectively relative to the 7053 keV decay. Especially for the 6854 keV decay, its relatively large hindrance factor cannot be explained by only the presumed small angular momentum change of ΔL=2 between the (3^+) parent and $(2^+/4^+)$ daughter state at 200 keV. This suggests that a change of configuration may also be required. However the decay to the 316 keV state has a relatively small hindrance factor of 4.2(5), if a ΔL=0 decay is considered. This is close to the accepted definition of unhindered decays (HF<4). If instead a ΔL=2 decay was considered (due to deduced E2 multipolarity for the 316 keV transition), then an even smaller hindrance factor of HF = 2.5(3) would be obtained. The 6746 keV decay appears to only have a small configuration change between the parent and daughter states.

In order to check the placings of γ transitions it was also possible to calculate the intensity ratios of the γ rays. The decay of the 316 keV excited state in ^{192}Bi proceeds via the 316-keV E2 or the 116 keV mixed M1+E2 γ ray transitions. A theoretical ratio of I(116)/I(316)= 100 for the intensities of the 116 and 316 keV decays was estimated according to the Weiskopf half-life estimates from Firestone [64], assuming M1 and E2 multipolarities respectively. The calculated value from the data however was found to be ∼ 12 (see Appendix D) which also indicates that mixing is occurring.

The half-life value that was determined for ^{196}Po is consistent with its quoted value in literature. For the ^{196}At, the value that was used was that of the main ^{196}At peak. The half-lives for each of the fine structure peaks was calculated individually, with the values being of the same magnitude as the main peak.

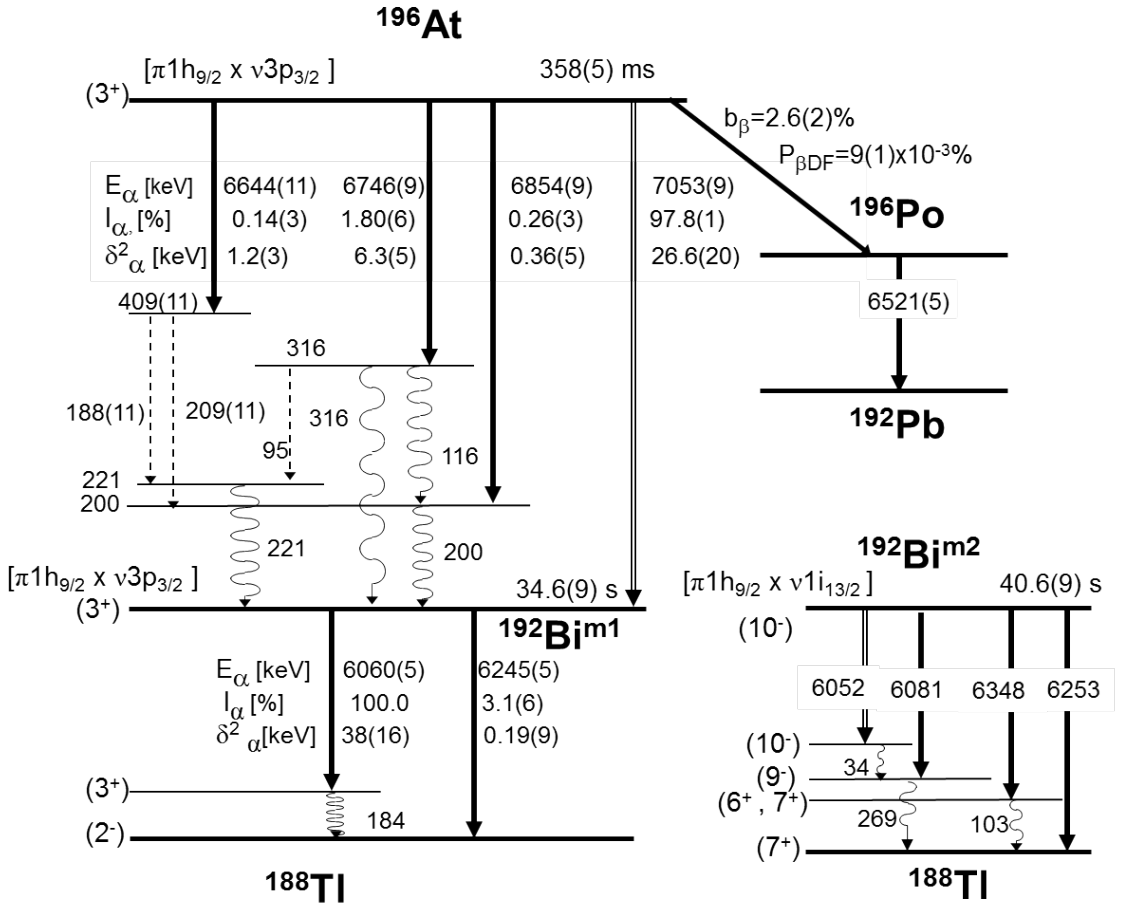

Figure 6.7: Decay scheme of ^{196}At deduced in this work. The yet unobserved 188(11) keV, 209(11) keV and 95 keV γ decays are shown by dashed lines. For consistency, the decay schemes of the two isomeric states in the daughter ^{192}Bi are also shown, including the tentative I^{π} values and configuration assignments taken from [122]. Due to the unknown relative excitation energy of the two α decaying states in ^{188}Tl, they are denoted as "m1" and "m2".

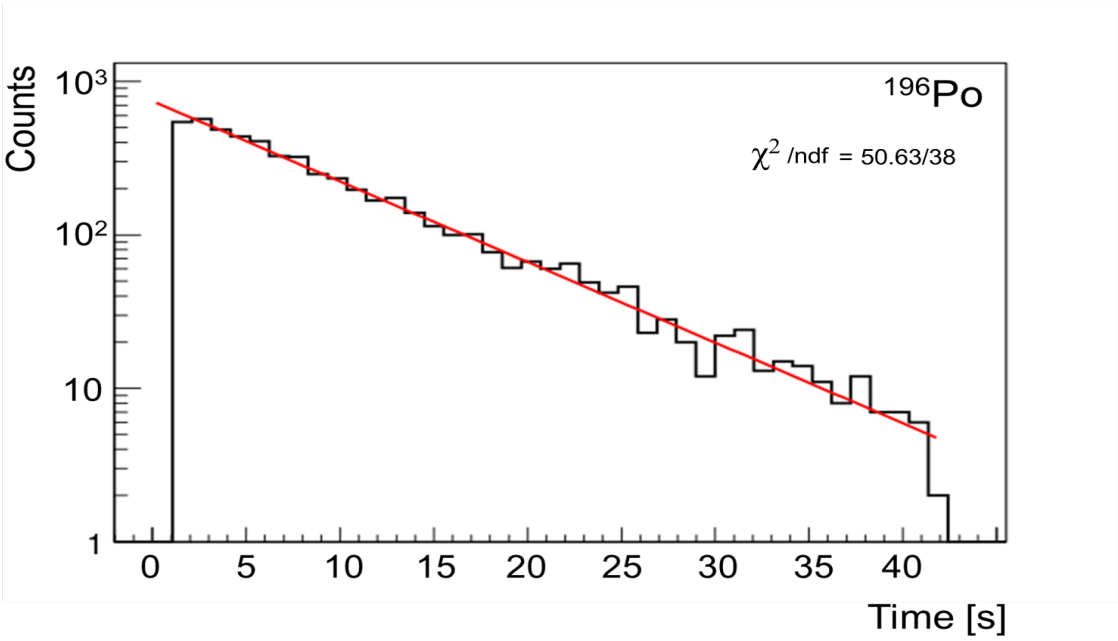

Figure 6.8: Half-life determination of ^{196}At. The data from Si3 and Si4 were used for the time distribution decay curve. The decay curve was fitted using an exponential resulting in a value of $T_{1/2}(^{196}\text{At}) = 5.8(1)$ s. Note that the decay measurement stops at $\sim$ 42 s, which corresponds to the length of the proton synchrotron booster supercycle in this experiment, at which point the WM moves again by introducing the newly-irradiated foil from the implantation position.

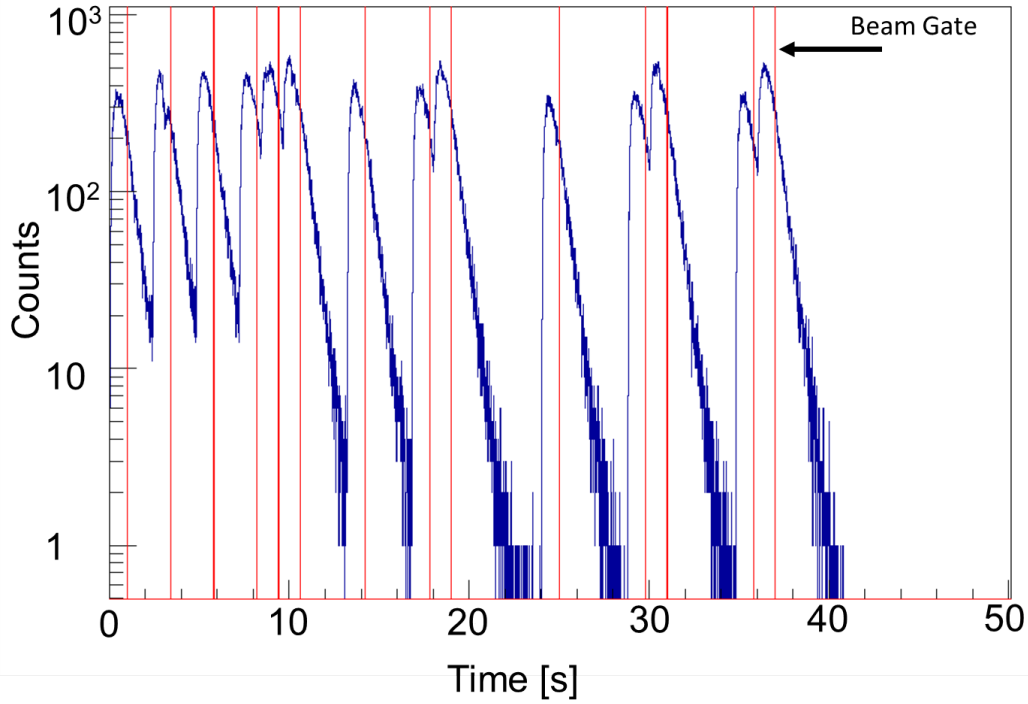

Figure 6.9: Timing structure used for determining ^{196}At half-life. This plot is a accumulation of all SCs within a file, providing they have the same SC pattern. The red line marks where the beam gate closes. At this point it is know that no more implantation can be occurring and it is only decay. This gives a starting point for the exponential fit of the decay.

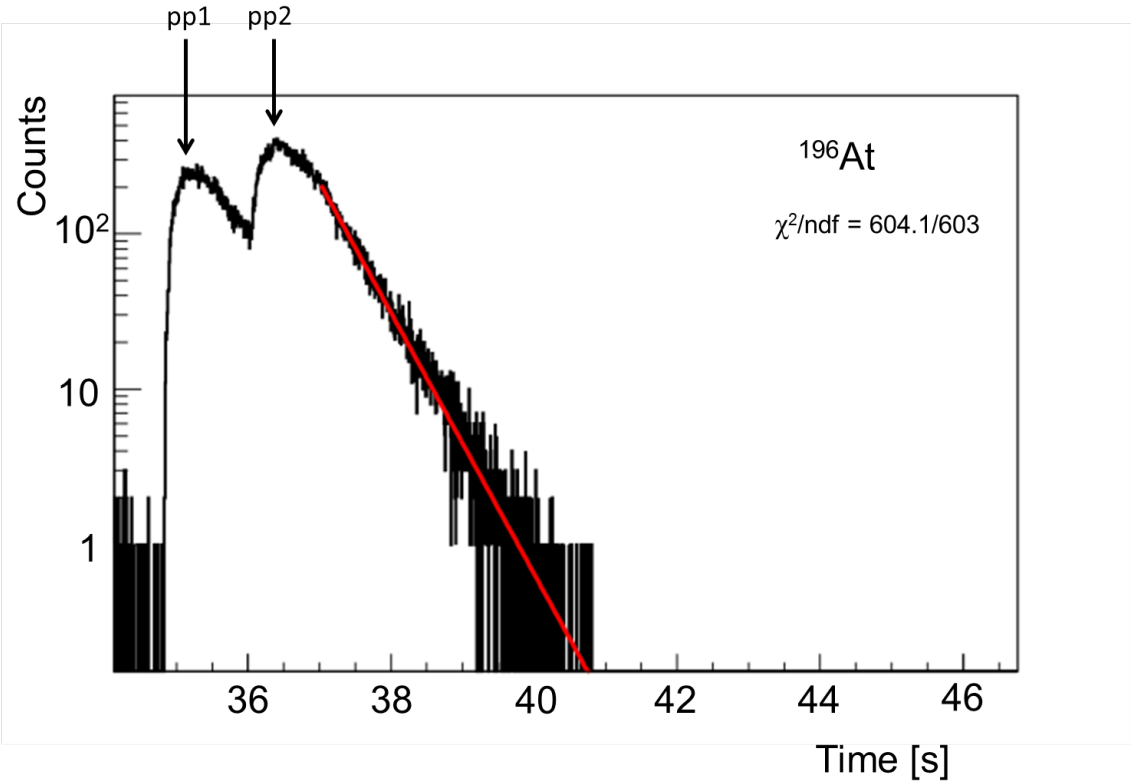

Figure 6.10: The time distribution for the 7053-keV α decay of ^{196}At, following the implantation during two consecutive proton pulses PP1 and PP2, separated by 1.2 seconds. The "decay part" of the time distribution within the time interval of 2.4–6 s was fitted with an exponential function, resulting in a value of $T_{1/2}(^{196}\mathrm{At}) = 358(5)$ ms. The data from Si1 and Si2 were used.

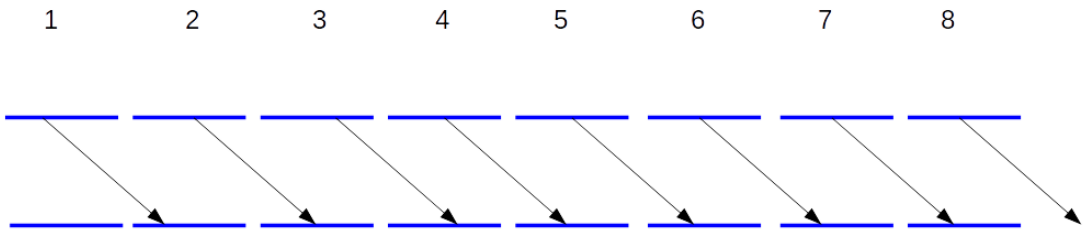

Figure 6.11: At the beginning of a supercycle, implantation will be occurring in the carbon foil at the implantation detectors. When the next supercycle begins, the decay from the previous supercycle will be occurring. In the diagram above, although implantation occurred during supercycle 4, the decay will actually occur during supercycle 5.

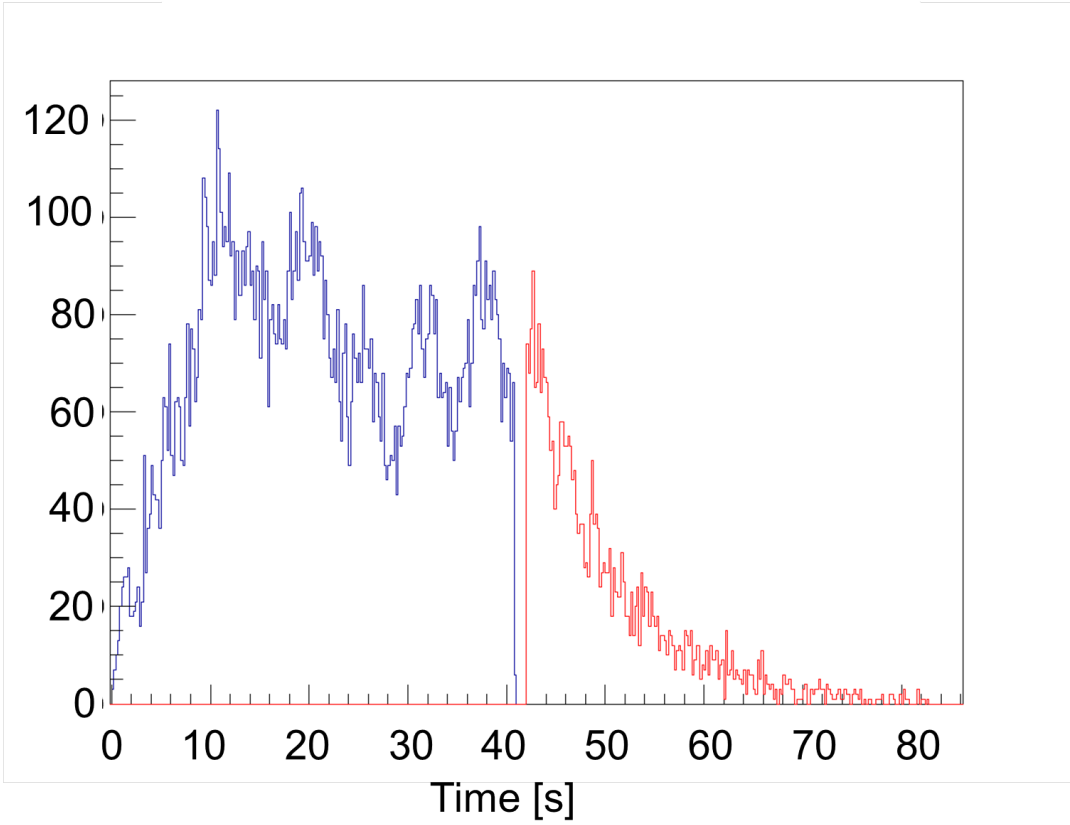

Figure 6.12: Alignment of decay plots to account for windmill movement, in this diagram the Si3 decay curve still needs to be scaled to the curve produced from Si2. The blue line is Si2 and the red line Si3.

Chapter 7

βDF of ^{196}At

7.1 βDF

The β-delayed fission of ^{196}At (fission of ^{196}Po after β decay of ^{196}At) has been observed in both the experiments at HRS and GPS. Only 14 fission events were observed in the HRS data and 284 events in the experiment at GPS. Therefore, in the following analysis only the data from GPS is discussed. The energy spectrum of single fission events that were observed in the GPS run, either in the Si1 or in Si2 detectors, in the energy range 30 MeV - 90 MeV is shown in Fig. 7.1. Out of 284 single fission events, 68 are coincident events, with both coincident fragments travelling back-to-back, measured by Si1 and Si2. Fission fragment mass distributions can only be deduced from the measured coincident events which have been calibrated using the Schmitt method as discussed in Chapter 5. This method was also applied in other studies carried out by the collaboration, in particular for ^{178,180}Tl [126, 28], ^{194,196}At and ^{202}Fr [77].

Before continuing with the results from ^{196}At, the results from ^{180}Tl are shown. These provide an ideal comparison for discussing the features of the βDF.

Approximately four times the statistics were collected for ^{180}Tl than for ^{196}At, including coincidence fission fragment–γ-ray data. The two-dimensional Si1-Si2 coincidence plot for βDF of ^{180}Tl in Fig. 7.2, shows two distinct clusters of points, clearly demonstrating the asymmetric fission of the daughter (after β decay) isotope ^{180}Hg. The TKE plot, Fig. 7.3 shows a single Gaussian shape with the most probable value of TKE(^{180}Hg)=133.20(14) MeV and FWHM of 15.0(9) MeV [28]. This proves that only one fission mode is present in ^{180}Hg in this case. The total fission fragment mass distribution, (black line) in Fig. 7.4 for ^{180}Hg, clearly shows an asym-

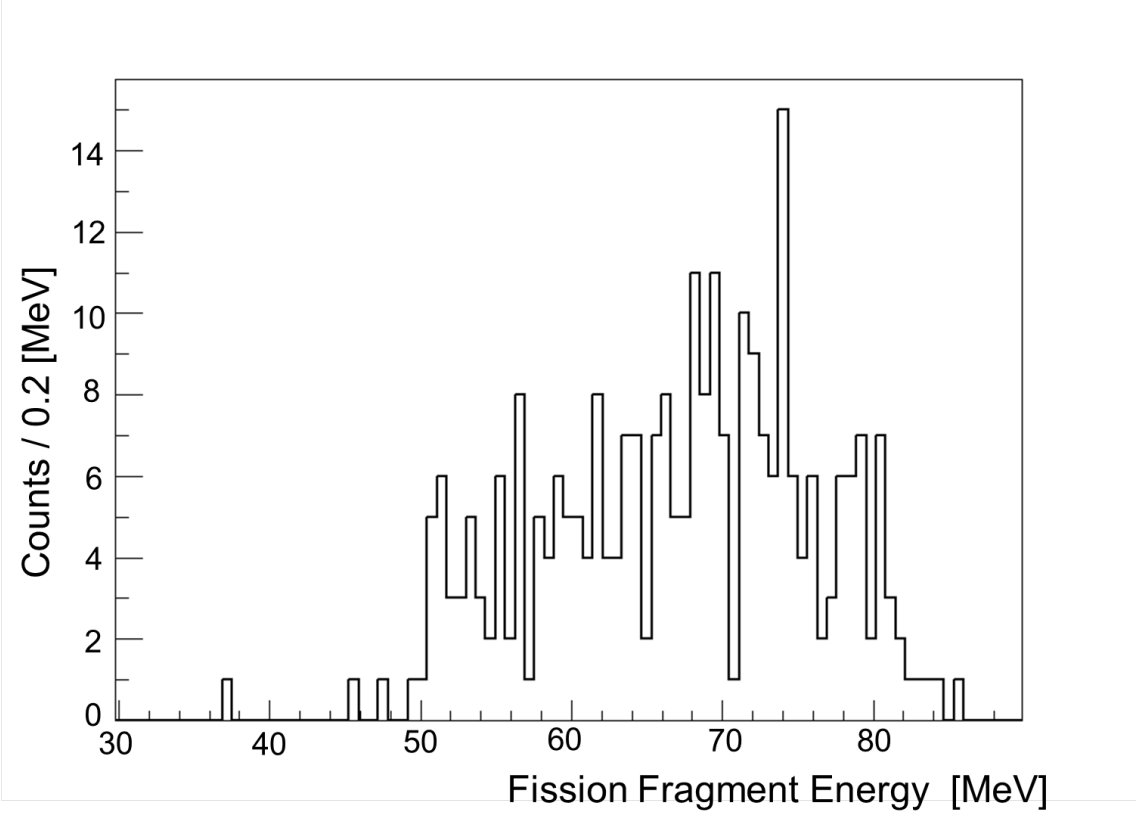

Figure 7.1: Calibrated energy spectrum of singles fission events in the βDF of ^{196}At, measured in the detectors Si1 and Si2.

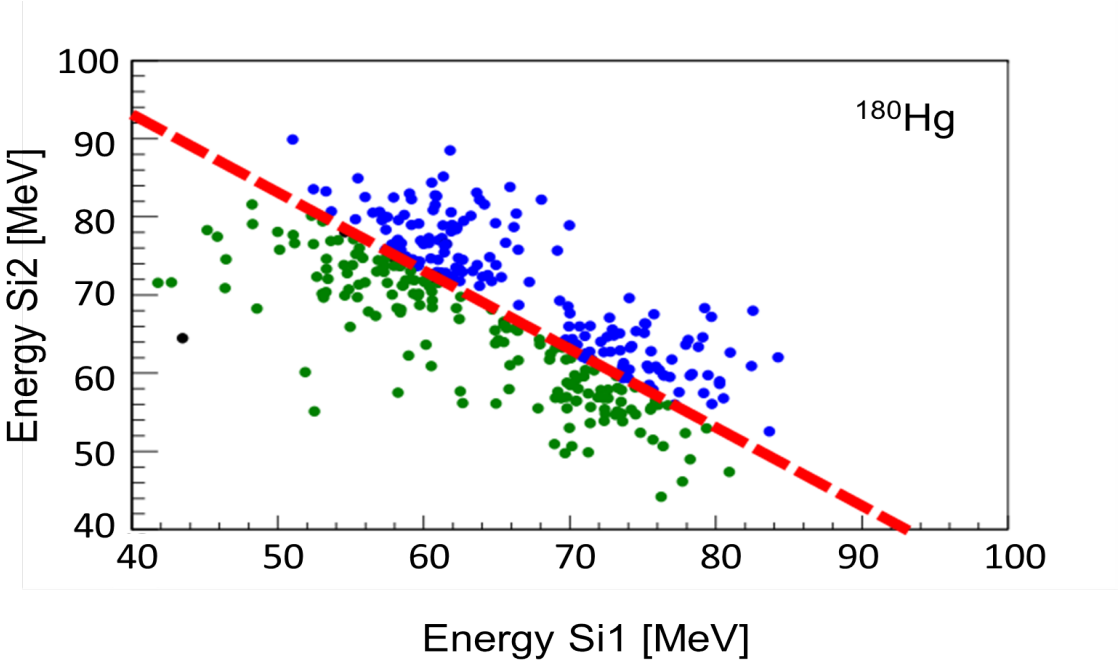

Figure 7.2: 2D coincident energy plot of ^{180}Hg. The red line marks the value of the TKE. The blue circles above the line are the fission fragments which have a TKE above the average, and the green circles are the fission fragments that have a TKE below the average. This split can further be used to see any correlations between the TKE and the shape of the mass distribution.

metric distribution, with the most probable heavy and light fission fragment masses of M_H= 100(1) and M_L = 80(1). In summary, all three plots clearly demonstrate that in the βDF of ^{180}Tl only a single (asymmetric) fission mode is present.

In contrast to ^{180}Tl it can be seen that, whereas the ^{180}Tl data show two distinct clusters in the 2D coincidence plot, a broad fission fragment area is observed for ^{196}At, as seen in Fig. 7.6. Also, instead of a single Gaussian-like TKE distribution observed for ^{180}Hg, the TKE distribution for ^{196}Po is much broader, suggesting that fission does not occur by a single fission mode. Fitting the whole broader distribution with a single Gaussian fit, gives the most probable value of TKE(^{196}Po)=147(1) MeV with FWHM of 24.2(9) MeV, see Fig. 7.5.

The points in Fig. 7.6 that have TKE values above and below the most probable TKE values are shown by the blue and green colours, respectively.

The black solid line in Fig. 7.7 shows that ^{196}At has a triple-humped mass distribution, with the most probable fission fragment masses, deduced from the Gaussian fit, being 88(2), 98(2) and 108(2), as seen in Fig. 7.7. Considering this

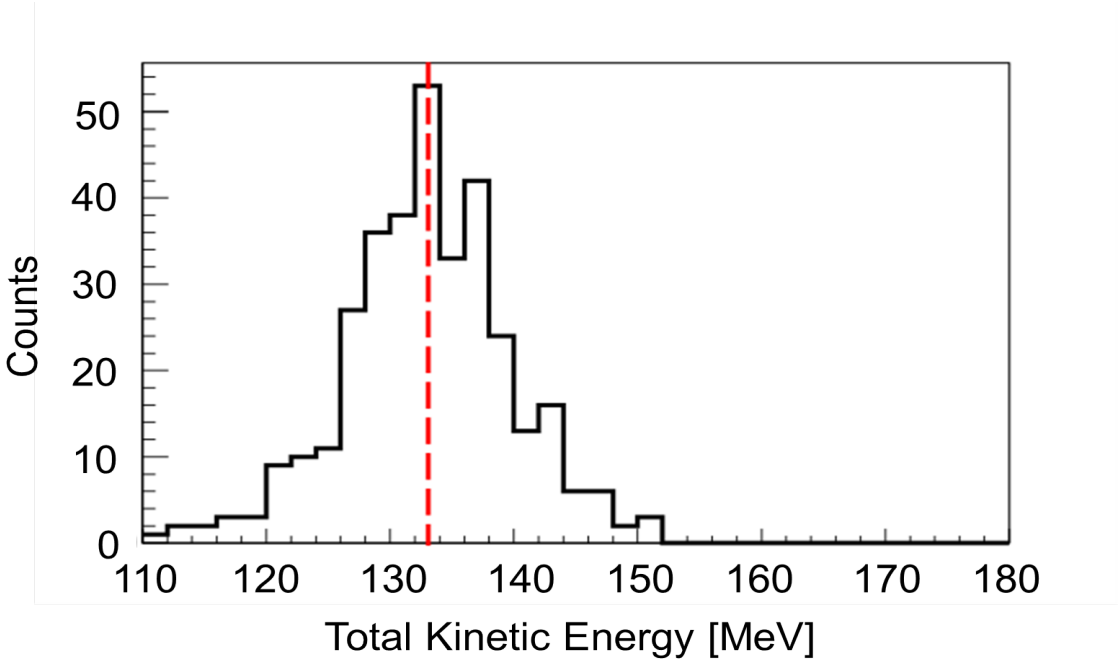

Figure 7.3: TKE of ^{180}Hg. The average TKE value is marked with the red dotted line.

information, along with the broader TKE distribution, gives convincing evidence that at least two distinct fission modes are present in the fission of ^{196}Po. The fission fragment masses of $M_L = 88$ and $M_H = 108$ represent the light and heavy peaks of the asymmetric mass distribution respectively, while the $M_S = 98$ corresponds to the symmetric mass distribution. As a second test, the χ^2 value was compared. Based on the fit, this gave a χ^2 value of 1.331 and number of degrees of freedom as 2. Using a standard χ^2 table, the $\chi^2_{0.05}$ value = 5.991. The fit χ^2 value is less than this, meaning this fit is likely to a 95% confidence level. As a comparison, Fig. 7.8 shows the same mass distribution, but in this case a single Gaussian has been fitted to the distribution. Using the χ^2 values again, then the single Gaussian distribution has a value of 50.58 and 20 degrees of freedom. This gives a $\chi^2_{0.05}$ value of 31.410 making this fit unlikely.

The difference in fission modes of ^{196}Po can further be investigated by examining the mass distributions for events with the TKE values above and below the most probable TKE. The distributions for ^{196}Po are shown by the blue dotted lines and solid green lines lines in Fig. 7.9. Notably, both the higher TKE and lower TKE mass distributions have the same two-humped structure seen in case of ^{180}Hg, which again

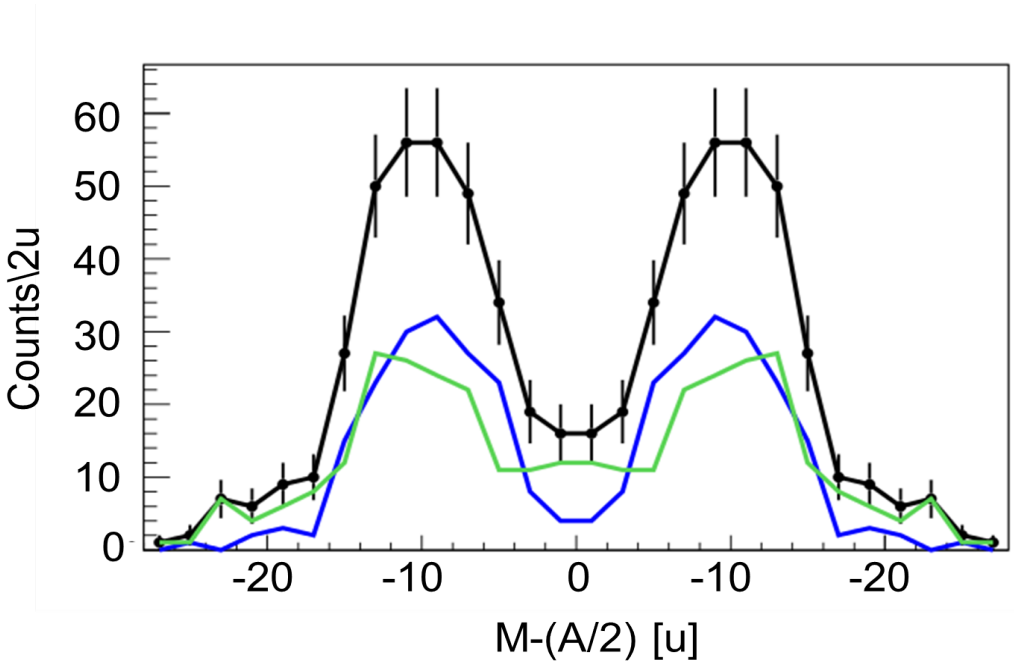

Figure 7.4: ^{180}Hg fission fragment mass distribution which shows a clear asymmetric mass distribution. The black solid line is the total mass distribution. The blue dotted and green solid lines are the mass distributions from the high and low TKE respectively. Since only one fission mode is present, it would be expected that the mass distributions would be the same shape.

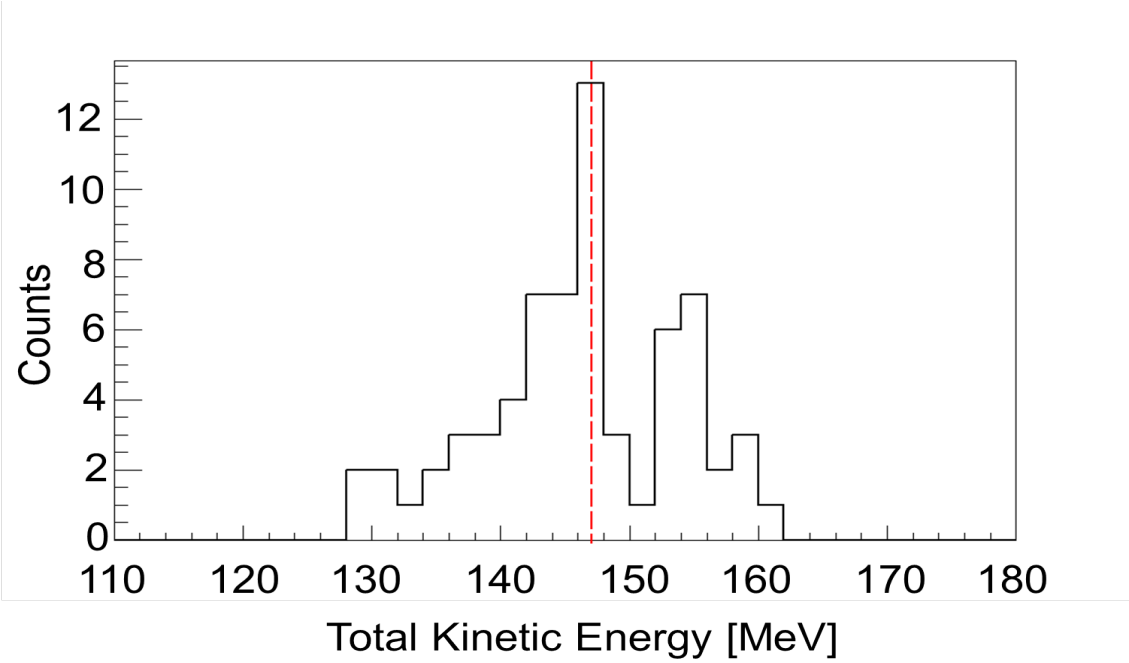

Figure 7.5: TKE of ^{196}Po with the average TKE of 147 MeV marked by the red dotted line.

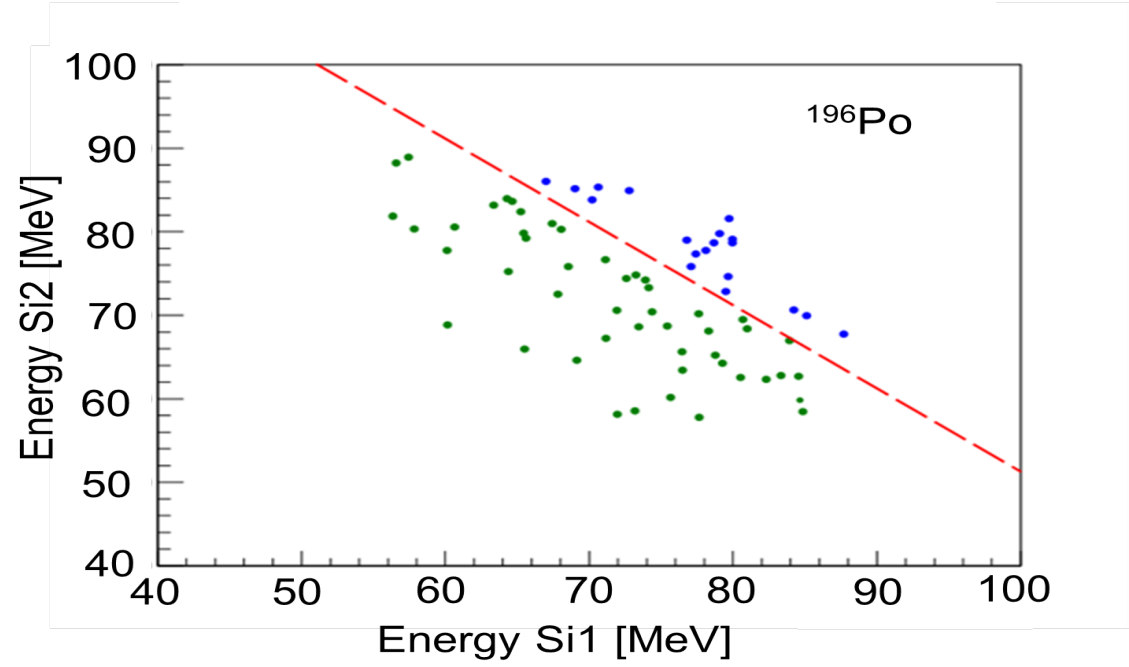

Figure 7.6: Coincident energy plot with points having an energy greater than 147 MeV marked in blue and those points less than 147 MeV marked in green.

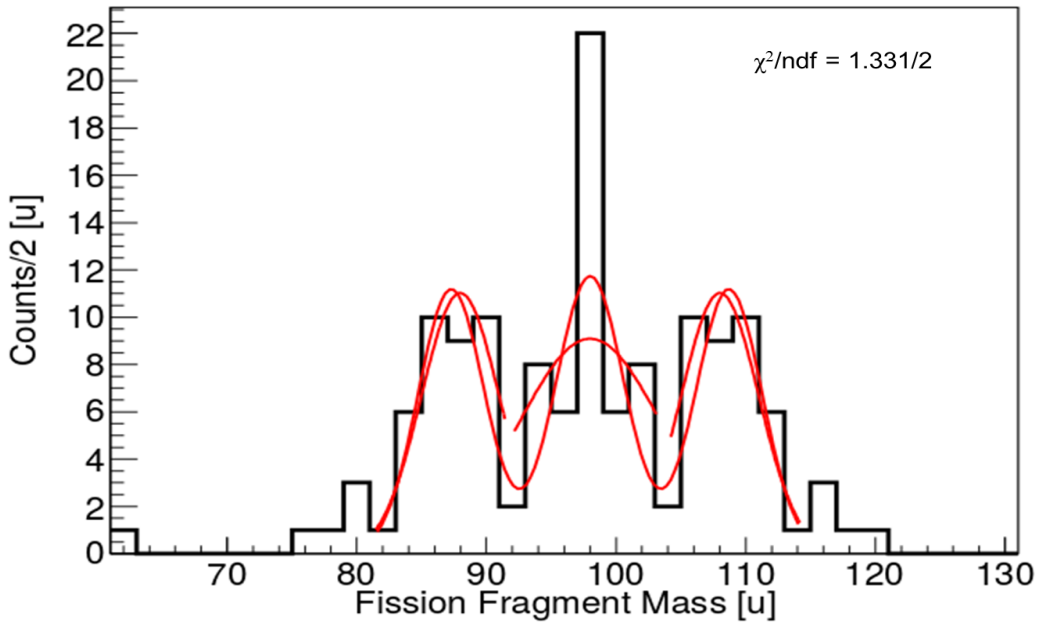

Figure 7.7: Fitted mass distribution of ^{196}Po. The Gaussian fit gives centroids of 88, 98 and 108.

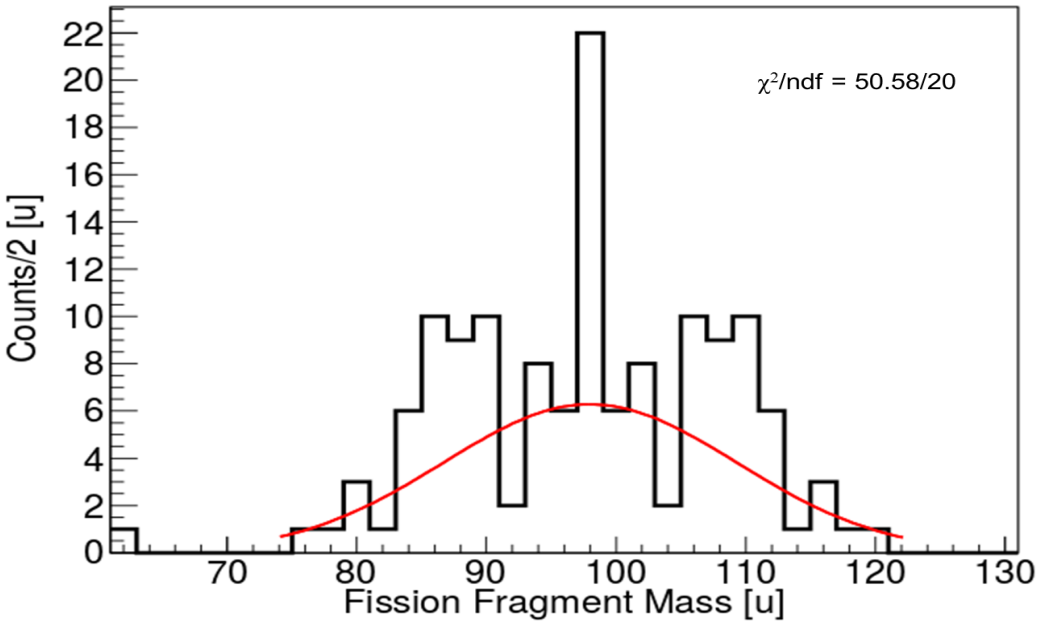

Figure 7.8: Single Gaussian fit of ^{196}Po mass distribution.

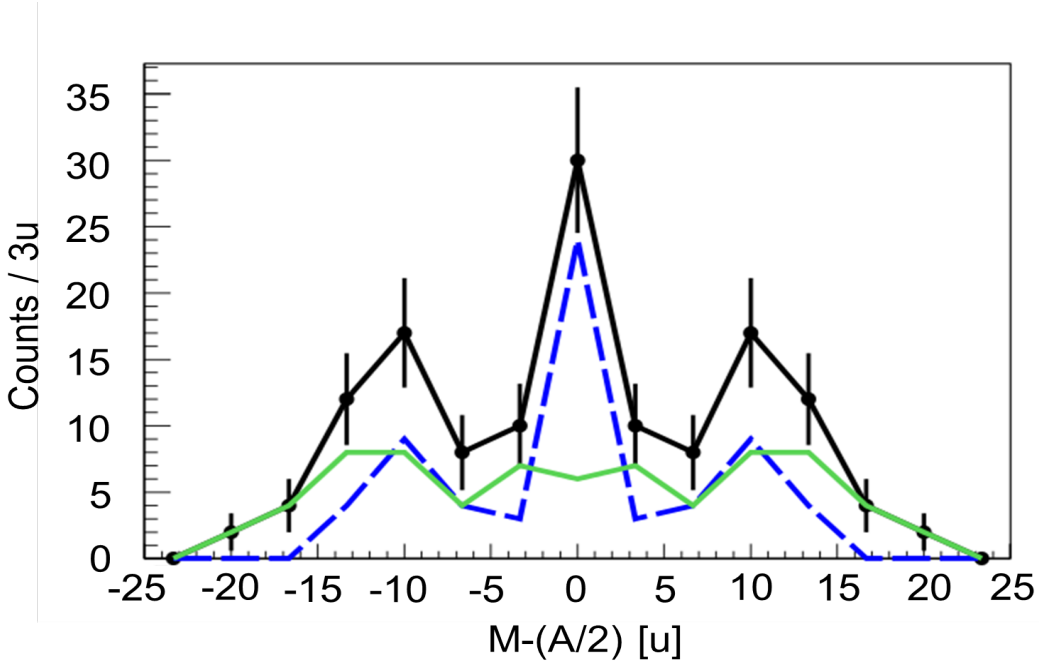

Figure 7.9: The mass distribution shown by the black line is for all observed events, while those shown by the solid green line and the dashed blue line correspond to events with the TKE values below and above the most probable TKE values, respectively, for ^{196}Po.

confirms that only a single asymmetric fission mode is present in this nuclide. In contrast to ^{180}Hg, the fission fragments of ^{196}Po with the higher TKE values, shown by the blue colour, indicate a mainly symmetric mass split. The mass distribution of events with the lower TKE values, shown by the green colour, appear to be a mix of symmetric and asymmetric modes. This slight mixing of the asymmetric mode to symmetric mass distribution (and *vice versa*) in the two distributions is probably due to the selection procedure for fission events, based on the most probable TKE value, leading to variations in the mass distributions.

In order to produce the calibration and the mass distribution plots, the starting mass number had to be assessed by considering the possibility of neutron emission before fission. The mass A = 196 was taken as the mass number of the fissioning ^{196}Po nucleus. It was used since the neutron separation energy, S_n (^{196}Po) = 10490(40) keV, is above the Q_{EC} (^{196}At) = 9570(30) keV preventing neutron emission from ^{196}Po after β-decay of ^{196}At. The emission of prompt neutrons from fission fragments was taken into account, and from energy considerations, the maximum number of neutrons that could be emitted is two per fission event. For the calibration

process however, it was assumed that no prompt neutrons were emitted.

It was not possible to deduce the Z values of the fission fragments with the current data. The most probable Z value was therefore deduced by assuming that the N/Z ratio for the fissioning parent is approximately conserved for the fission fragments as described by the unchanged charge distribution [127]. In this case for ^{196}Po, the N/Z ratio = 1.33. A second method by which the Z values could have been found would have been to use the minimum potential energy model [128]. It can be simplified to $Z_f/A_f = Z_1/A_1 = Z_2/A_2$, however once one Z value is found the other can be deduced by subtraction.

For the symmetric mass distribution, the most probable nuclide is ^{98}Mo which has a N/Z ratio = 1.33 and is stable. For the asymmetric mass distribution, the masses which contribute most to the peaks are $A = 88$ and $A = 108$. Using the same ratio method (N/Z), the Z values were deduced to be $Z_L = 38$ and $Z_H = 46$. This gives possible identification of the fragments as ^{88}Sr, which has a $N/Z = 1.32$ and ^{108}Pd , $N/Z = 1.35$. Taking the average of these two ratios gives 1.34. Both of these nuclei are stable.

The maximum number of neutrons that can be emitted in the fission of ^{196}Po can be estimated by comparing the calculated energy release $Q_{fis}(^{196}\text{Po})$ with the deduced average TKE. The calculated energy release values can be determined as,

$$Q_{fis}(A, Z) = \Delta M(A, Z) - \Delta M(A_1, Z_1) - \Delta M(A_2, Z_2) \tag{7.1}$$

, where $A = A_1 + A_2$, $Z = Z_1 + Z_2$, and ΔM is the mass excess of the respective nuclei. The maximum fission energy release (assuming no neutron emission) was calculated for the symmetric component as,

$$\begin{aligned} Q_{fis}(0n) &= \Delta M(^{196}Po) - \Delta M(^{98}Mo) - \Delta M(^{98}Mo) \\ &= -13483 - -88114.8 - -88114.8 \\ &= 162776.6keV \\ &= 162.78MeV \end{aligned} \tag{7.2}$$

. The maximum excitation energy of the two fission fragments can be calculated by,

$$\begin{aligned} E^*_{max,tot} &= Q_{EC} + Q_{fis}(0n) - TKE \\ &= 9570 + 162776.6 - 147000 \\ &= 25346.6keV \\ &= 25.35MeV \end{aligned} \quad (7.3)$$

. This available energy is shared between the two fission fragments, γ-rays and any emitted neutrons. Unfortunately due to the HPGe detectors being disconnected there is no γ energy information. It is therefore not possible to state how much energy the γ-rays will use. Looking at the neutron separation energy (S_n) of the fragments, it can be determined if it is possible for neutron emission to occur. Taking ^{98}Mo , the neutron separation energy is $S_n = 8.64$ MeV. Multiplying this by a factor of two, to account for the two fragments, gives a total energy of 17.28 MeV. Although lower than the maximum energy available, the remaining energy may not be enough to account for any γ-rays, or the kinetic energy of the neutrons. It is therefore extremely unlikely that two neutrons will be emitted, but it is possible that one neutron could be emitted.

For the possible fragments from the asymmetric mass distribution, the maximum fission energy energy release is calculated using a similar method giving,

$$\begin{aligned} Q_{fiss}(0)n &= \Delta M(^{196}Po) - \Delta M(^{88}Sr) - \Delta M(^{108}Pd) \\ &= -13483 - -87921.4 - -89524.4 \\ &= 163962.8keV \\ &= 163.96MeV \end{aligned} \quad (7.4)$$

. This gives the maximum available excitation energy of the fragments as

$$\begin{aligned} E^*_{max,tot} &= Q_{EC} + Q_{fiss}(0n) - TKE \\ &= 9570 + 163962.8 - 147000 \\ &= 26532.8keV \\ &= 26.53MeV \end{aligned} \quad (7.5)$$

. The neutron separation energies for the probable fission fragments are; S_n (^{88}Sr) = 11.11 MeV and S_n (^{108}Pd) = 9.22 MeV. This gives a total energy of 20.33 MeV which, when deducted from the total excitation energy, only leaves 6.2 MeV. It is therefore likely that only one neutron emission could occur.

When the TKE was drawn, it became apparent that there seemed to be a 'high' and a 'low' TKE. Fitting a Gaussian to the low and high sections gives values of 144.9(8) MeV for the low and 154.7(10) MeV for the high, leading to a difference of $\sim$ 10 MeV between the average TKE of each section, when the values are rounded. The split between the low and high appears to occur at $\sim$ 151 MeV. The χ^2 value for fitting these two peaks was 9.019 with 8 degrees of freedom, leading to a $\chi^2_{0.05}$ value of 15.507 making this likely. As a comparison for the single Gaussian fit, the χ^2 value was 22.25 with 14 degrees of freedom giving a $\chi^2_{0.05}$ value of 23.685.

Compared to the mass distributions for the high and low TKE using the values of 147 MeV, Fig. 7.9 the mass distributions for using 151 MeV as the limit, Fig. 7.10, produces a different mass distribution. This difference occurs in regard to the shape and number of counts in the asymmetric and symmetric fission mass distributions. Instead of mass distributions that are much more clearly split into symmetric and asymmetric for high TKE and low TKE respectively, the 151 MeV mass distribution are more mixed for both the high and low TKE.

For both the high and low TKE (using the 151 MeV split), the probable fission fragments were deduced for all the coincidence events, in addition to those noted above. Taking the high TKE first, the symmetric nuclide is identified to be ^{98}Mo. The same calculations were applied, but this time the $E^*_{max.tot}$ value = 21.34 MeV. Assuming that two neutrons in total are emitted, their energy will sum to be 17.28 MeV. Since the separation does not leave $\sim$8 MeV when subtracted from the total available, it is unlikely that two neutrons would be emitted.

Considering the low TKE value, the asymmetric pair is ^{88}Sr, ^{108}Pd. Although Fig. 7.10 does indicate a second pairing, in this section they are considered to be caused by the binning of the plot. This pairing of ^{88}Sr, ^{108}Pd has already been calculated, but with the change in TKE energy the total energy available is now $E^*_{max,tot}$ = 22.53 MeV. In this case $\sim$ 8 MeV is not available, which means two neutron emission is again not possible in this case. The mass and energy information for the two TKE values are summarised in Table 7.1.

For completeness, the TKE for 1 and 2 neutron emission have been briefly looked at. Using the same analysis as previously, the average over the whole TKE for 1n emission was taken to give a value of 147.5(14) MeV. For 2n emission, the mean

Table 7.1: The probable identity of the fission fragments based on the N/Z method and the total available energy in each case are summarised. The possible emission of either 1 or 2 neutrons is based on the neutron separation energy of the fission fragment

TKE (MeV)	Asymmetric or Symmetric	Fission Fragments	Available Energy (MeV)	Total S_n (MeV)	1n Emission	2n Emission
>147	symmetric	^{98}Mo	25.35	17.28	possible	unlikely
<147	asymmetric	^{88}Sr, ^{108}Pd	26.53	20.33	possible	unlikely
>151	symmetric	^{98}Mo	21.34	17.28	possible	unlikely
<151	asymmetric	^{88}Sr, ^{108}Pd	22.53	20.33	possible	unlikely

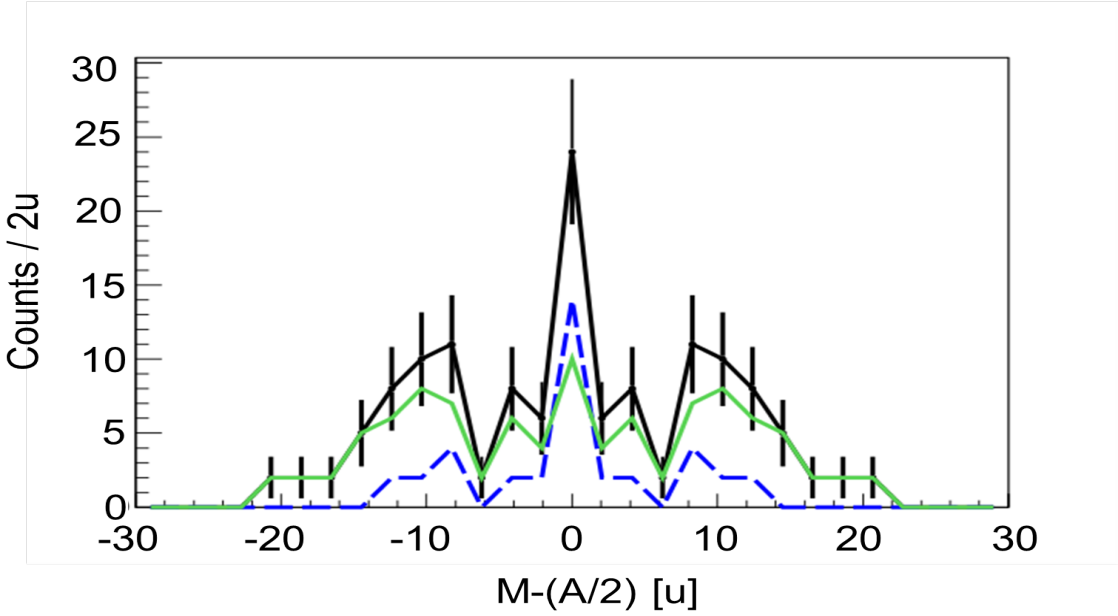

Figure 7.10: Mass distribution of ^{196}Po with TKE split at 151 MeV.

TKE is 147.8(16) MeV. A fit was performed on the peaks that can be considered to make up the low and high TKE regions. This gave values of 145.8(10) MeV for the low TKE peak of 1n emission, and 156.4(40) MeV for the high TKE peak. Doing the same for the 2n file gave 146.3(8) MeV for the low TKE peak and 156.4(8) MeV for the high TKE peak. The mass distributions for the low and high TKE regions for both 1n and 2n emission are given in Appendix E.

7.2 Probability of BDF

By definition, the probability of βDF can be calculated from:

$$P_{\beta DF} = \frac{N_{\beta DF}(^{196}At)}{N_{\beta}(^{196}At)} \tag{7.6}$$

, where $N_{\beta DF}$ is the number of observed fission events and $N_{\beta}(^{196}At)$ is the total number of ^{196}At nuclei that decay by β decay. Only the GPS data for N$_{\beta DF}$ and Nβ were used as the statistics were more numerous. However, due to contaminants in the ^{196}Po region for the GPS data, the ratio of counts of the 7053 keV ^{196}At peak and the 6521 keV ^{196}Po peak from the HRS run was used. As the branching ratios

will be constant, then the ratio of these peaks should also stay constant, allowing the number of counts in the 6521 keV peak in the GPS data to be calculated. The $P_{\beta DF}$ was deduced as $9(1)\times 10^{-5}$.

7.3 Discussion

Comparing the mass distribution with the example of ^{180}Hg given in Section 2.6.2 it is clear that ^{196}Po does not exhibit the clear asymmetric split of ^{180}Hg. This indicates that the fission of ^{196}Po produces a mixture of both asymmetric and symmetric fission. As a check , the FWHM of the TKE can be compared. For the ^{180}Hg plot the TKE (^{180}Hg)=133.2(14) MeV and a FWHM of 15.0(9) MeV [28], and for ^{196}Po the values were TKE(^{196}Po)=147(1) MeV with a FWHM of 24.2(9) MeV. This shows the ^{196}Po TKE spectrum is much broader, which suggests that more than one fission mode is present.

Investigation of the TKE and mass distribution indicated that the mass distributions produced from the low and high TKE, based on the average value of 147 MeV, produced a more defined symmetric/asymmetric mass split than the plots using the TKE split of 151 MeV. This suggests that the value of 147 MeV for the average TKE should be taken as the referred value. To confirm whether this is the case, two methods can be used. The simplest method is to change the binning of the mass distribution to determine if the symmetric/asymmetric split becomes more defined. A second method would be to increase the statistics which would either increase the prominence of the split or it would become one distribution, giving a clearer indication of what is happening.

Recently, the potential energy surface (PES) for the fission of ^{196}Po was calculated by using the microscopic Hartree-Fock-Bogoliubov (HFB) theory with the D1S Gogny interaction as seen in [129]. HFB is a ground state theory in which the mean field and pairing field influence each other. The PES showed a broad and flat plateau, with many weakly pronounced valleys and ridges, that did not exceed a 1–2 MeV energy difference. This was discussed by Ghys *et al.* [77] in which it was seen that pattern in the PES for ^{196}Po, without well-defined shell corrections, should lead to several fission paths. These fission paths could produce a mixture of symmetric and asymmetric mass distributions, which is more in agreement with this experiment's data.

Chapter 8

Preliminary Analysis and α Decay Results of ^{194}At

Part of the data set collected at both the May 2011 and May 2012 runs were ^{194}At. Unfortunately the amount of data collected for this nuclide is less than that for ^{196}At. Apart from one run, no HPGe detectors were connected. However, the γ statistics in the run are low. This therefore limits the information that can be learned from the data in this file. The data present can still be used to infer a situation, but cannot be said to be conclusive. This will restrict other areas of analysis, such as the decay scheme, as regards to what can be accomplished.

Previously, both an α decay and βDF studies, were performed by A.N. Andreyev *et al.* [38, 40]. The data for both these studies came from an experiment performed at the Separator for Heavy Ion Products (SHIP) at GSI, Darmstadt. They used the ^{141}Pr(^{56}Fe,3n)^{194}At reaction. The 400 μg/cm^2 thick ^{141}Pr targets were mounted on a target wheel. After separation by the SHIP velocity filter, the evaporation residues were implanted into a 16 strip position-sensitive silicon detector (PSSD). To measure any $\alpha - \gamma$ coincidences, a large volume four-fold segmented clover germanium detector was installed behind the PSSD. There were also three time-of-flight detectors in front of the PSSD to allow the reaction products to be separated from any scattered beam particles. In the work presented in this thesis, the ^{194}At was studied at ISOLDE in a similar manner to ^{196}At (as described in the preceding Chapters).

8.1 Alpha Decay

To calibrate their spectra, Andreyev *et al.*, used the lines of other nuclei produced in the reaction through other reaction channels. Although this method has been used for the previous nuclide ^{196}At, it was deemed not suitable in this case. As seen in the paper by Andreyev *et al.*, they found ^{194}At to have an isomer. This leads to two α decay energies for ^{190}Bi which, without knowing the α decay that is present, means they cannot be used. The energies for the two bismuth α decays are also very close in energy, leading to the possibility of both being present, but not being clearly separated. It is is also apparent that in this work fewer peaks are being seen than in the work by Andreyev. This also leads to uncertainty as to which peaks are being seen. This is also why the values of the ^{194}At peaks are not reliable to use. As a trial, the values for the main peaks were used as calibration values and it was found, that even if one of the peaks matched, then none of the others did. This also gave weight to the argument to not use this method of calibration.

A different calibration method was therefore utilised for this data. In this experiment the isotopes of astatine were produced in sequence as the experiment progressed. Initially, the calibration for the ^{196}At data was used. This however appeared to not fit the energies of the ^{194}Po and ^{190}Bi peaks (which although not used for the calibration, are still used as guidance values). It therefore seemed likely that the calibration had shifted during the run of ^{195}At. A calibration of these data was performed and the values of the energy peaks corresponded, within error, to the NNDC [114] values. Using this new calibration, ^{194}At was recalibrated, and produced values for the ^{190}Bi and ^{194}Po that were within the error margin of previously determined values [130, 131].

The calibrated α-decay energy spectrum is shown in Fig. 8.2, with the energies of the peaks marked. Comparing the values of those believed to be ^{194}At with the values determined by Andreyev *et al.*, it can be seen that they do not match, see the decay scheme in Fig. 8.1. It was also noted that the energies of two of the ^{194}At peaks were very similar in value to those seen in the analysis of ^{196}At. To clarify if they were indeed ^{194}At peaks, the half-lives were deduced. This will be fully described in Section 8.2.

The half-lives were found to be different, implying that the peaks did belong to ^{194}At. From Fig. 8.2, the energies of the ^{194}At peaks are 7051(11) keV,7106(11) keV and 7157(10) keV, ^{194}Po 6850(11) keV and ^{190}Bi 6446(10) keV. Comparing once again to Andreyev, it can be seen that there were more lines present than in this

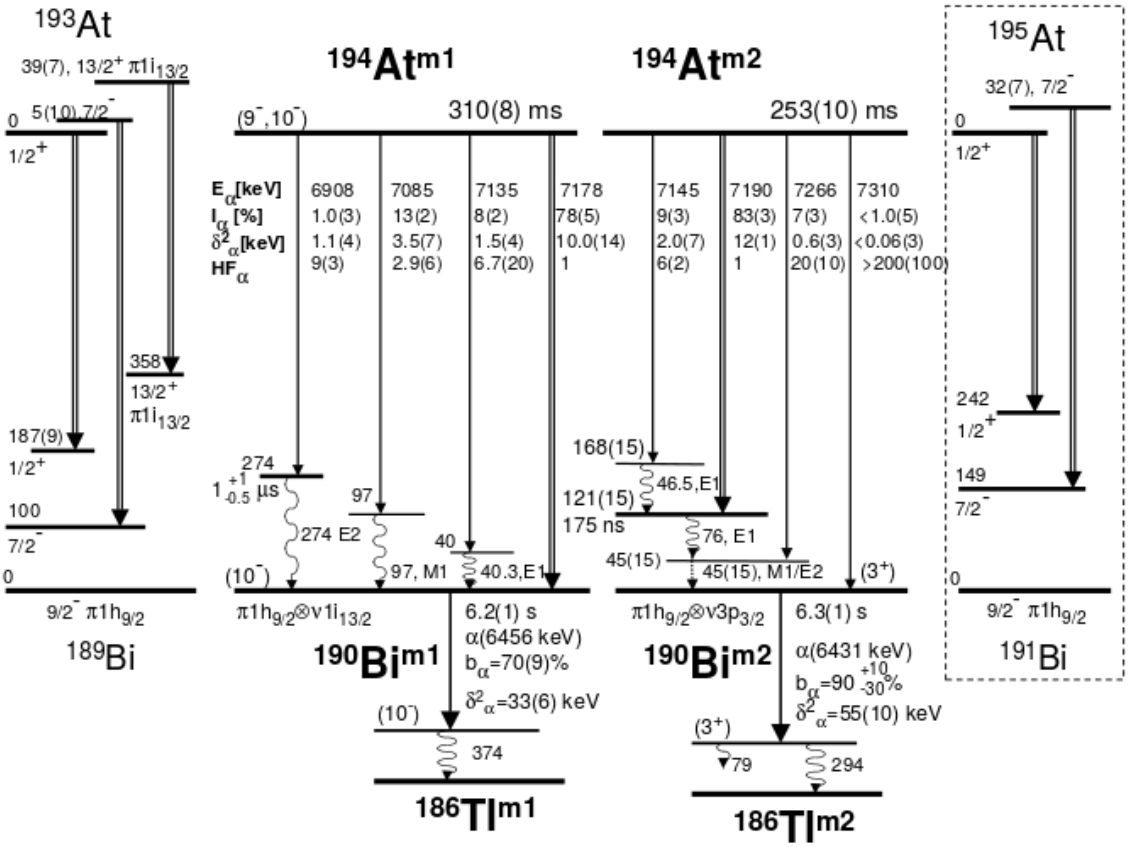

Figure 8.1: ^{194}At decay scheme produced by Andreyev *et al.* [38]

.

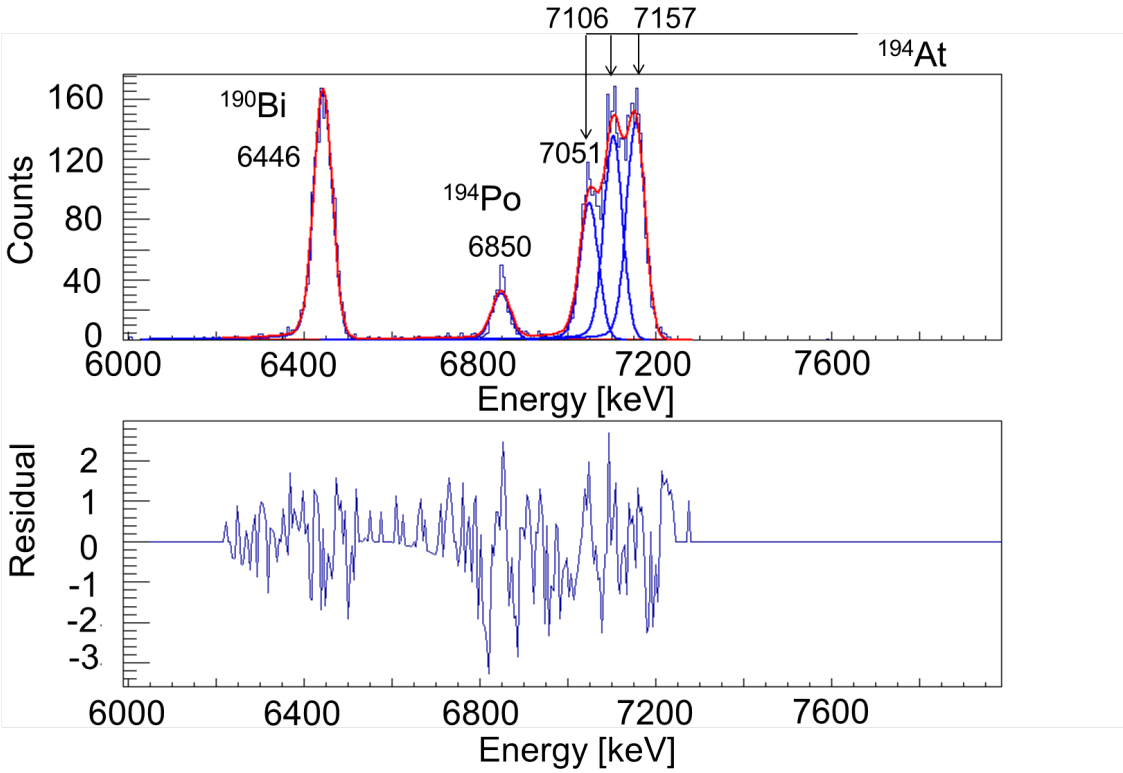

Figure 8.2: Fit of the ^{194}At α-decay spectrum with the energies of the peaks marked.

thesis work. It is likely that this is in part due to a crucial difference between the two experiments. At ISOLDE, there is almost a total absence of α + e summing effects compared to the experiment at SHIP. This is because at SHIP, the nuclei are implanted into a position sensitive silicon detector (PSSD) which causes the summing effects, from conversion electrons, to be more problematic. These effects include the creation of new peaks, shifting peaks or causing them to broaden. In the ISOLDE experiment, the nuclei are implanted into a carbon foil (which is thinner), reducing the summing effects and therefore producing clearer spectra.

Although not part of this work, an experiment was performed in September 2014 using laser selectivity to study the hyper fine structure (HFS) for ^{194}At. This had the advantage that isomer separation becomes possible. HPGe detectors were also connected to give γ data. It is expected that the analysis of the data will shed more light on the decay of ^{194}At.

8.2 Half-lives

The half-lives of ^{194}Po and ^{194}At were calculated using the grow and decay method since they decayed within the implantation detector. Due to smaller statistics, the peaks were not as defined as those for ^{196}At. This meant the error on most of the peaks is large. Taking the half-life of ^{194}Po first, the value in literature is 0.392(4)s from the study by Wauters *et al.* [131]. It was found that the timing structure in the runs used for this work, did not produce well defined decay curves, see Fig. 8.3. Due to this, deciding where the limits of the fit should be was not as obvious as in the case of ^{196}At. To produce a peak that had (when the y-axis was logged) a 'straight' line decay, the binning had to be altered. In Fig. 8.4 a 'zoomed in' area of Fig. 8.3 is shown, which has been fitted. The half-life was determined to be 0.590(177) s, which is a greater value than that quoted in [131], and has a χ^2/ndf value of 0.09701/1.

The individual values of the three ^{194}At peaks are only given, since without knowing to which isomer the peaks belong, an overall value cannot be taken. The three half-life values are 0.433(107) s, 0.727(80)s and 0.470(163) s for the 7051 keV, 7106 keV and 7157 keV α-decay energy peaks respectively. An example of one of the fits is given in Fig. 8.5.

The ^{190}Bi half-life however, could be calculated by fitting an exponential function to the decay curve, since the ^{190}Bi decayed at the decay detectors position. This gave a half-life value of 5.4(4) s, see Fig. 8.6. This can be compared to the values

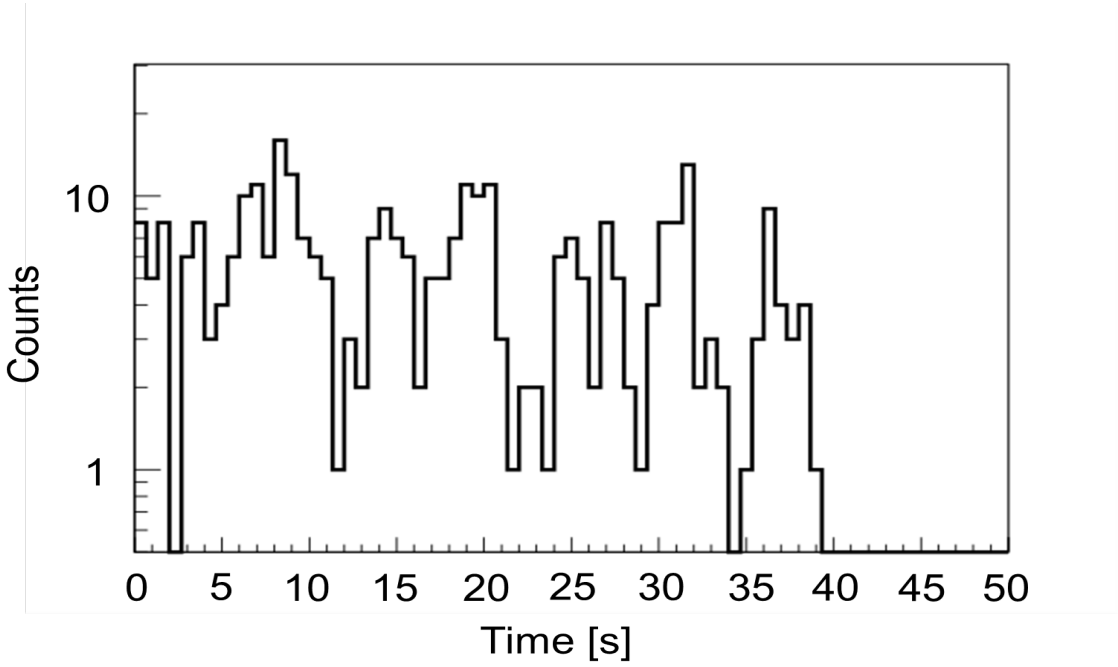

Figure 8.3: Timing grow and decay peaks that were produced to determine the half-life of ^{194}Po.

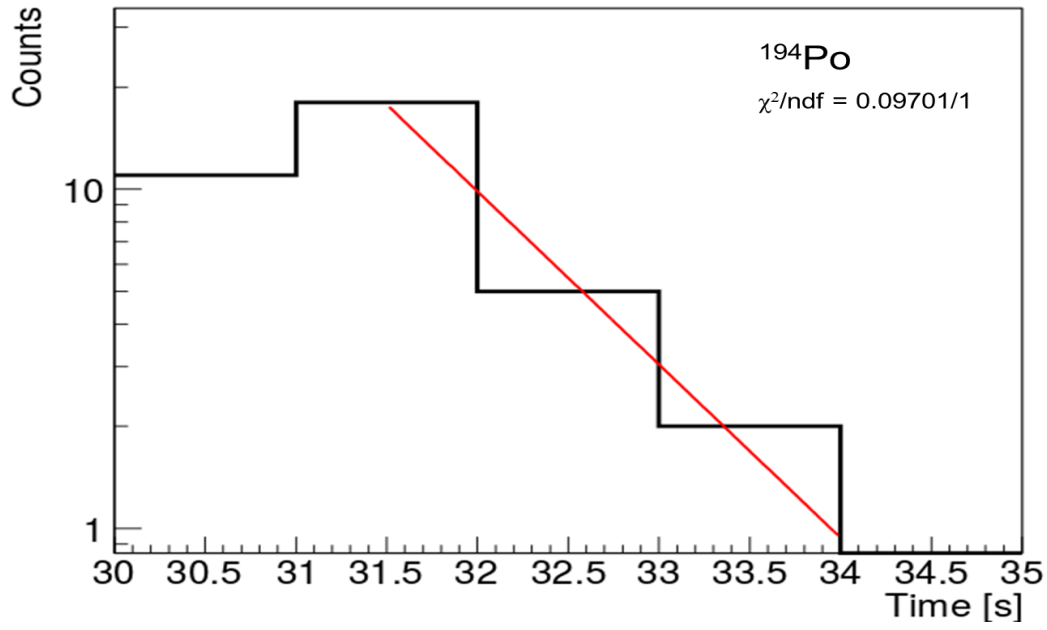

Figure 8.4: Fitted peak to determine the ^{194}Po half-life. As can be seen the number of bins is small. This was required in order to make a fit of the peak.

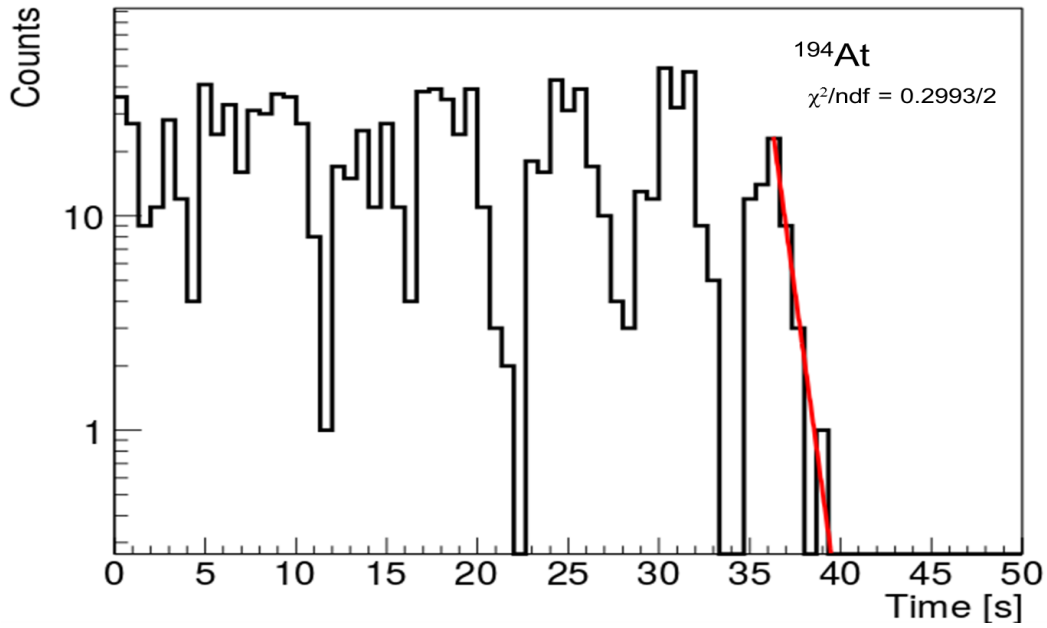

Figure 8.5: Half-life fit of the 7157 keV α decay peak. Although the peaks were slightly more defined, the low statistics still caused uncertainty for the limits of the fit.

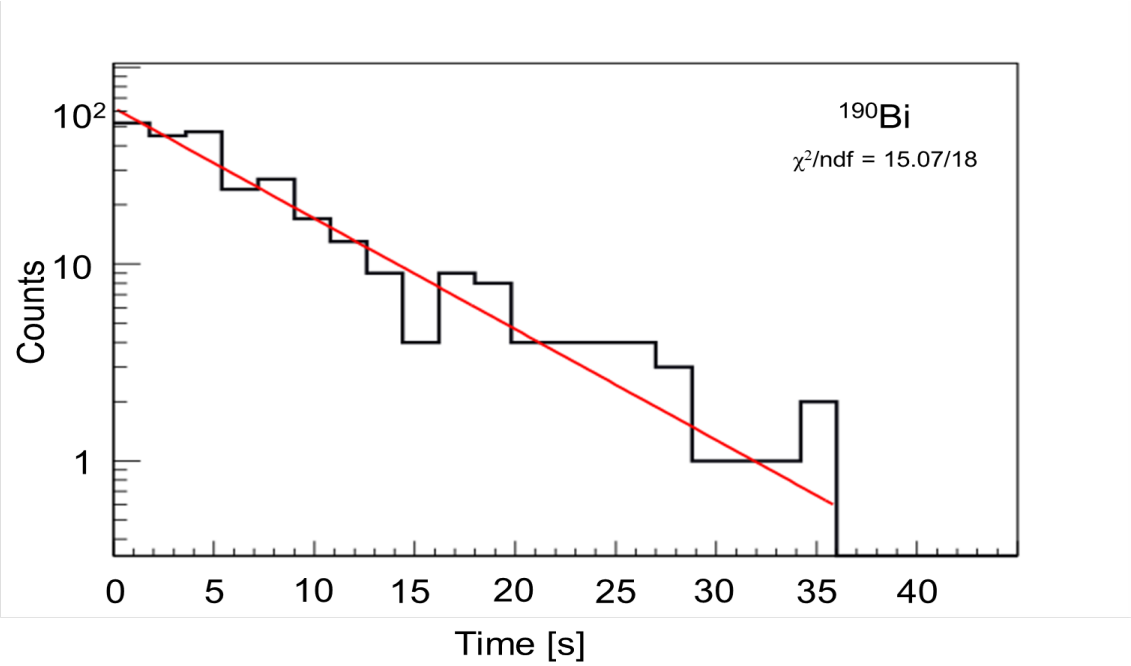

Figure 8.6: Half-life determination of ^{190}Bi by fitting the decay seen in the decay detectors. This gave a value of 5.4(4) s.

by Andreyev *et al.* which were 6.2(1) s and 6.3(1) s for the two isomers seen in that study [38].

8.3 Branching Ratios

The same method was used to calculate the branching ratio of ^{194}At as in the analysis of ^{196}At. The method, however, is simplified in this case, as ^{194}Po appears to fully decay at the implantation detector position due to its shorter half-life of 0.757 ms. This means that no corrections need to be included for the movement of the windmill. The total number of counts of ^{194}Po does not need to be determined by considering the timings of the supercycles. Since all the polonium decays at the implantation position, no counts need to be accounted for at the decay detectors position. Therefore no SC constraints need to be applied. It is not possible, however, to determine if any ^{194}Po is present, with no lasers tuned for astatine ionisation, as there are no dedicated files for this. This can therefore not be included in the calculation, and it needs to be assumed that all counts of ^{194}Po are from the β decay of the ^{194}At. The branching ratio was therefore calculated from,

$$b_\beta = \frac{N_\beta(^{194}At)}{N_\beta(^{194}Po) + N_\alpha(^{194}At)} \tag{8.1}$$

This gives a value of $b_\beta(^{194}\text{At}) = 8(1)\%$. From the study by Andreyev *et al.* [40], they calculated a value of ~ 8.3 % for the β branching of both isomers. This value is in agreement with the calculated value in this work.

8.4 Discussion

As mentioned in Section 8.1 the number of α-decay peaks seen in this work is less than those seen by Andreyev *et al.*. One reason, as previously mentioned, is the α + e summing which would be much more prevalent at SHIP. A second reason for this could be, that in this work, only one of the isomers is being populated. In order to determine if this is the case, more data would be required, including $\alpha - \gamma$ spectra. An experiment was run in 2014 in which the laser spectroscopy of ^{194}At was carried out. This will provide γ information, HFS measurements and possibly greater statistics. The data from this experiment will help to clarify the issues in this work, but the data is not part of this thesis and so will be analysed at a later date. Another method by which it can be seen if one or two isomers are present is to look at the FWHM of the peaks [78]. This gives a FWHM of 45 keV, 39 keV and 49 keV (lowest energy astatine peak first) for ^{194}At, 36 keV for ^{194}Po and 51 keV for ^{190}Bi. These values would suggest that the peaks with larger FWHM values could potentially be two peaks that cannot be resolved by the silicon detectors. The energy values of the ^{194}At energy peaks are also different from those in previous literature. These values tend to be greater than those found in this work.

Regarding the half-life value for ^{194}Po, further work will need to be pursued, ideally with greater statistics. From the analysis carried out in this thesis, it is apparent that the method used to calculate the half-life does not produce reliable results with low statistics. The half-lives of the ^{194}At peaks, although closer to the values that have been seen previously, also have a large error for two of the peaks. This again indicates that the fitting method needs to be improved for low statistics. In his paper, Andreyev *et al.* have placed two ^{190}Bi peaks in the decay scheme, each with a half-life of ~ 6 s. In this work only a single peak is seen, which could indicate only one isomer is being excited, or the two peaks are not resolved. Therefore only one half-life value was deduced, which is lower than the values seen previously.

To fully present an α-decay study of ^{194}At, more data will be required, especially

$\alpha-\gamma$ coincidence data which would allow a decay scheme to be built for this nuclide.

Chapter 9

Preliminary βDF Results of ^{194}At

9.1 βDF

The fission data for ^{194}At was calibrated using the Schmitt calibration as described in Chapter 5. βDF was observed in both the HRS and GPS runs. From the HRS data, 6 single fission events were seen, of which two are coincident events. In the GPS run, 382 single fission events were seen, out of which 107 are coincident fission events. Due to the greater number of statistics, only the GPS data are considered. The total energy spectrum of the fission events seen in Si1 and Si2 is shown in Fig. 9.1 over the energy range 30–90 MeV. To determine the mass distribution, only the coincident events are used. Following the same analysis method as used for ^{196}At, the fissioning polonium mass was taken to be $A = 194$. This was determined after looking at the neutron separation energy, which is $S_n = 10720(40)$ keV and the Q_{EC} (^{194}At) = 10293 (30), stopping any neutron emission after the β decay from ^{194}At to ^{194}Po. For the calibration process, it was assumed that no neutrons were emitted. To determine whether it was energetically possible for prompt neutrons to be emitted from the fission fragments, a comparison was made of the total kinetic energy with the energy released. From this it is possible to deduce how many, if any, neutrons were emitted. Before this calculation could be carried out, more information was required about the identity of the fission fragments and the TKE of the system.

The TKE was plotted and a Gaussian fitted to give the mean energy. This gave a value of 146(1) MeV. The fit is shown in Fig. 9.3. The 2D coincidence energy plot is shown in Fig. 9.2. Comparing this to the 2D energy plots from ^{180}Hg and ^{196}Po, it is similar to the latter. This indicates that ^{194}Po fissions with both a symmetric and asymmetric mass distribution.

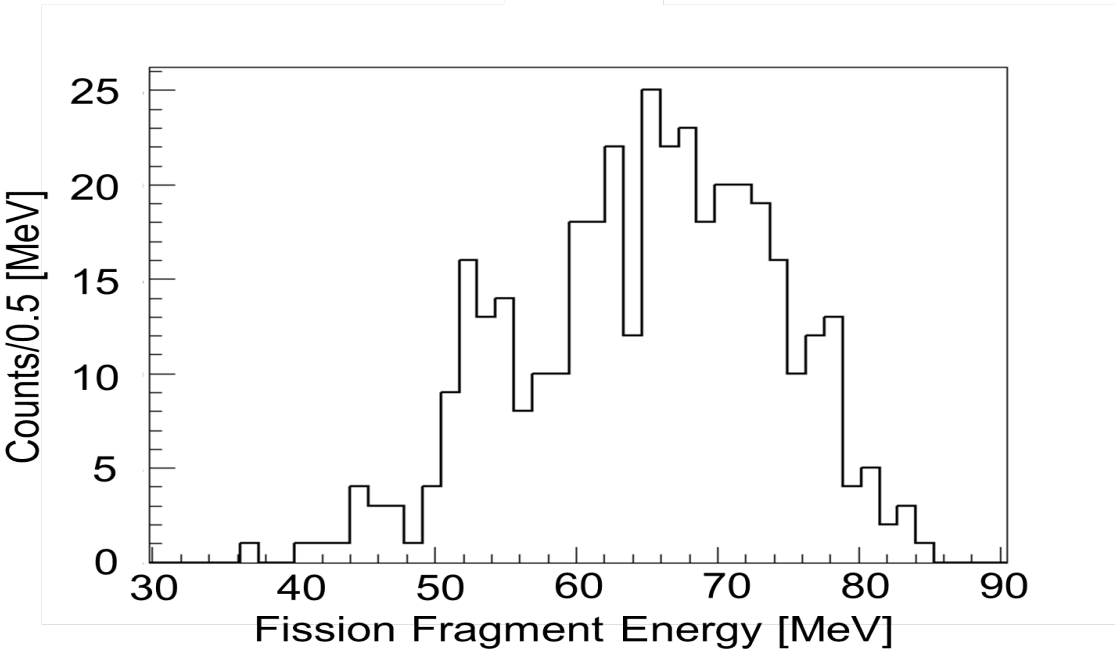

Figure 9.1: ^{194}At fission events energy spectrum showing the combined events from Si1 and Si2.

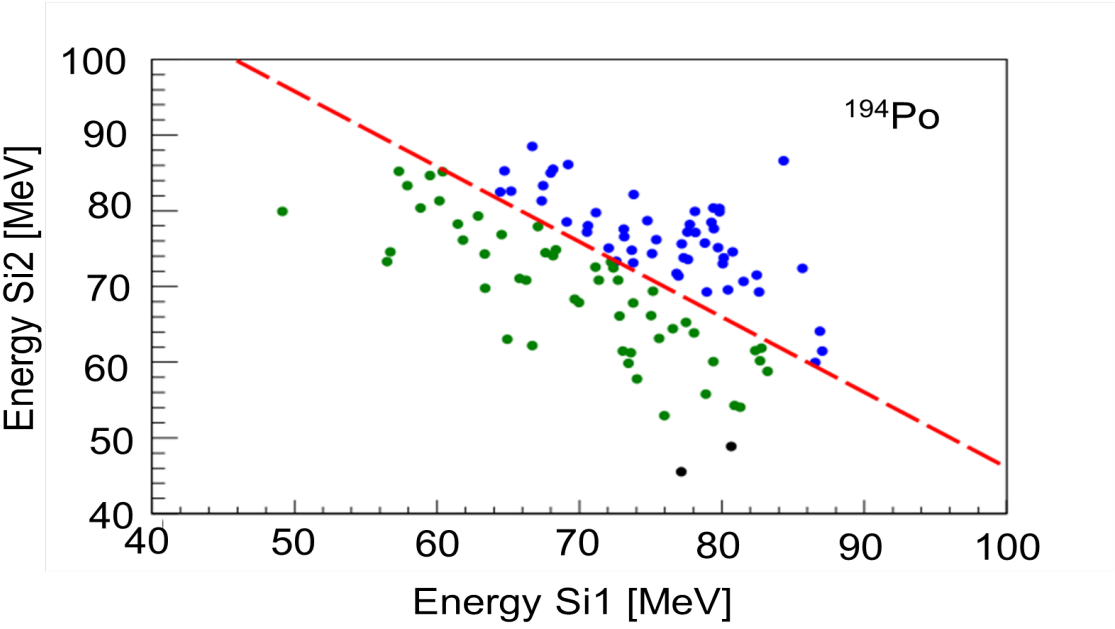

Figure 9.2: 2D coincidence plot for ^{194}Po which when compared to ^{180}Hg and ^{196}Po, is much more similar to the latter.

To try and ascertain which fission fragments were present, the mass distribution was then plotted. This mass distribution plot, seen in Fig. 9.4 appears to show five peaks. It is likely that this is caused by the binning applied. It should be noted however, that attempts to change the binning to give an asymmetric and symmetric mass distribution, as seen in the case of ^{196}At, were unsuccessful. By fitting the peaks, FWHM were obtained. From these it was seen that, the symmetric distribution has a FWHM $\sim$ 7(2) u, The asymmetric pair of peaks beside the symmetric peak have a FWHM $\sim$ 6(3) u and $\sim$ 6(2) u respectively. The second asymmetric pair have a FWHM $\sim$ 3(1) u and $\sim$ 3(1) u respectively. This shows that the one asymmetric pair of fission fragments has a FWHM of almost half the symmetric peak. The other asymmetric pair however, have a FWHM almost the same as the symmetric peak. This could suggest that due to the binning the apparent two asymmetric pairs could actually just be one asymmetric distribution. If however the speculation is made that the five peaks are actually present, then this could be evidence of both isomers fissioning. In that case, what is being seen is that both fission bi-modally, giving rise to a symmetric mass distribution and an asymmetric distribution. Since the symmetric distribution will be constrained to a mass by the nature of the mode, this could account for the peak being wider than the other peaks. The two asymmetric distributions would therefore represent each of the isomers. Further analysis for five peaks is given in Appendix F.

Applying a Gaussian fit to the three peaks, would give masses for the symmetric peak of 97(2) and the asymmetric peaks as 84(2) and 110(2).

As seen before for ^{196}Po, the mass distribution can be compared using a multiple Gaussian fit, Fig. 9.4 and a single Gaussian fit, Fig. 9.5. With the multiple Gaussian fit, as shown in Fig. 9.4, the χ^2/ndf value is 21.74/21, which when compared with the χ^2 tables, it is less than the 95 % confidence level making this fit likely. For a single Gaussian fit, the χ^2/ndf value is 2.647/3, which is also less than the 95 % confidence level of 7.815, which would make this fit also likely. This shows that for the mass distribution of ^{194}Po, even though it is suggesting that multi-modes are present, greater statistics are needed in order to fully confirm this.

Taking the symmetric mass distribution, the energetics of the distribution can be calculated. Using the formula,

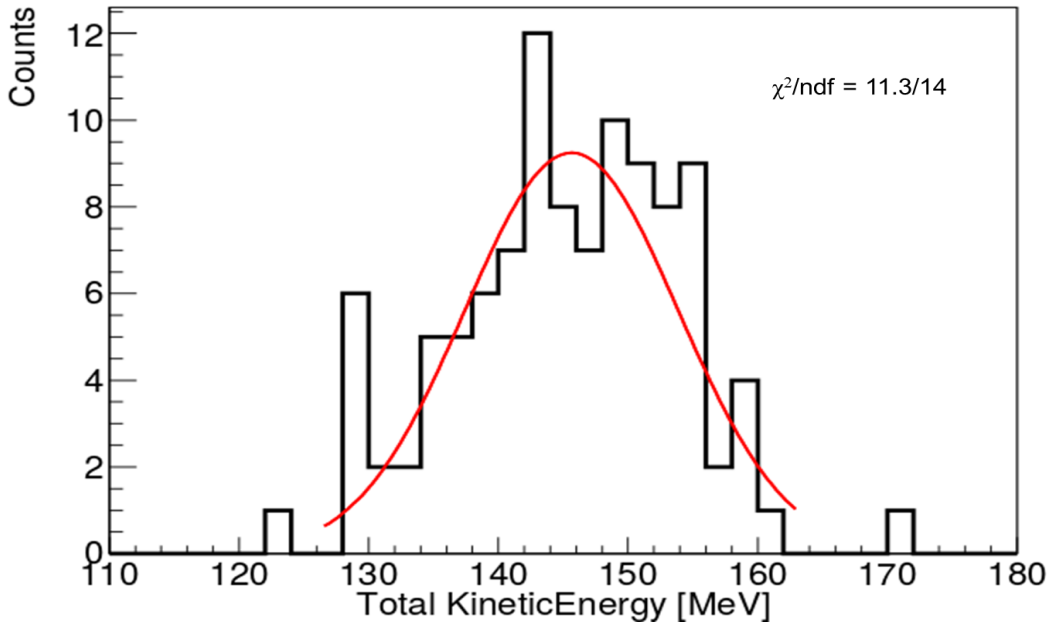

Figure 9.3: TKE fit of ^{194}At to determine the average TKE from fission. The average TKE value was determined to be 145.6 MeV.

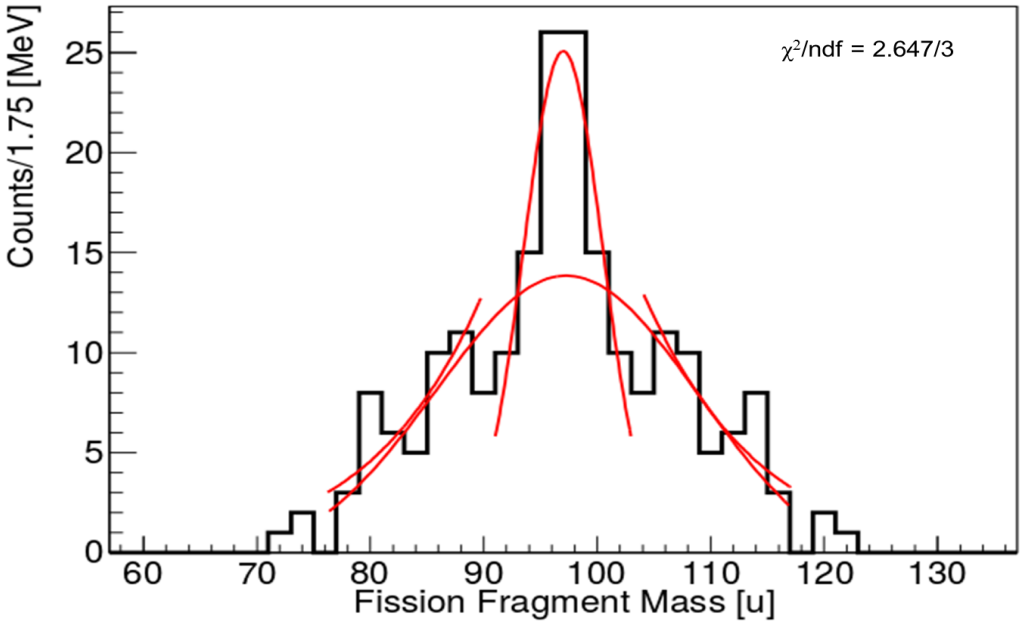

Figure 9.4: Mass distribution of ^{194}At fitted with multiple Gaussian fits.

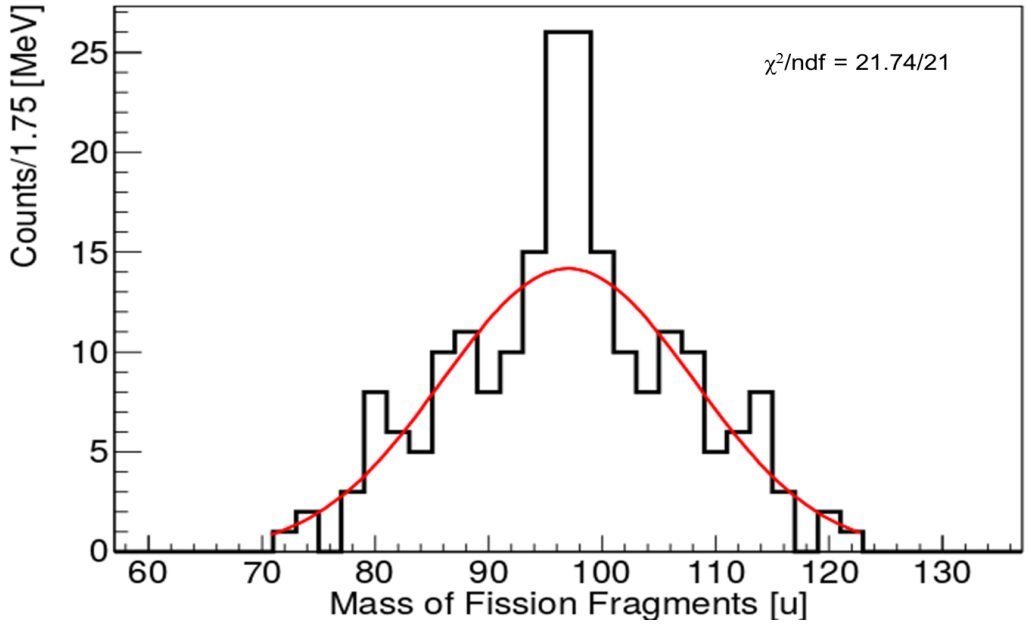

Figure 9.5: Mass distribution of ^{194}Po fitted with a single Gaussian.

$$\begin{aligned} Q_{fiss}(0n) &= \Delta M(^{194}\text{Po}) - \Delta M(^{97}\text{Mo}) - \Delta M(^{97}\text{Mo}) \\ &= -11005 - -87543.6 - -87543.6 \\ &= 164.082 MeV \end{aligned} \quad (9.1)$$

The maximum energy available is calculated as,

$$\begin{aligned} E^*_{max.tot} &= Q_{EC} + Q_{fiss}(0n) - TKE \\ &= 10.293 + 164.082 - 145.6 \\ &= 28.78 MeV \end{aligned} \quad (9.2)$$

The neutron separation energy for ^{97}Mo is 6.82 MeV. Assuming that a neutron is emitted from each fission fragment, then the energy required is 13.64 MeV. This still leaves 15.14 MeV for the emission of any γ rays, making two neutron emission possible. Since there were no HPGe detectors connected, it is not possible to see if there are any γ rays emitted and at which energies.

For the asymmetric mass distribution of ^{194}At, the assumption that the fission fragments will have the same N/Z ratio (1.31) as the fissioning parent is again applied. The fission fragments were identified as potentially being ^{84}Rb and ^{110}Ag. Carrying out the same calculations as above, it is found that in the case of ^{84}Rb, then 20.90 MeV is available. The neutron separation energy S_n for ^{84}Rb is 8.76 MeV and for ^{110}Ag the neutron separation energy S_n is 6.81 MeV. Taking these values, it is seen that there is not enough energy available to allow for two neutron emission.

9.2 Probability of βDF

To calculate the probability of βDF, the same formula from ^{196}At was used. In this case however, only an estimate of the probability can be made. Since it cannot be confirmed if both isomers are present, then it cannot be said if both isomers or only one will fission. Therefore, the total number of ^{194}At counts will need to be used in the calculation. Again the polonium peak is not well defined in the GPS data due to contaminants, so the ratio was taken of the ^{194}Po to the total number of ^{194}At in the HRS run. This ratio was then used with the GPS file in order to calculate the number of polonium counts in the α-decay energy peak. This gave a $P_{\beta DF}$ value of 0.86(3) %. In the βDF study by Andreyev *et al.* [40] they calculated an estimated value of the $P_{\beta DF}$, assuming that in one case, only one isomer fissions, and in the second case, that both isomers fission. For only one isomer fissioning, their value was $\sim$ 1.6% which is around twice the value calculated in this work. When they assumed that both isomers fissioned, then the value was $\sim$ 0.8 % (assumption was also made that the two isomers had the same β branching of $\sim$ 8.3 %). This value for both isomers fissioning is in good agreement with the $P_{\beta DF}$ calculated in this work.

9.3 Discussion

The 2D coincidence plot clearly shows that the βDF of ^{194}At is a mix of asymmetric and symmetric fission. As was the case with ^{196}At, the plot does not have defined regions, indicating that only one fission mode is present.

The probability calculated for ^{194}At is much larger than that for ^{196}At. A greater probability would be expected for ^{194}At, as by referring back to Fig. 2.17 then it can be seen that the trend is increasing for the more proton rich astatine isotopes.

This calculated probability however, is not truly reflective of the ^{194}At, since it is not possible to determine from the data used in this work whether both isomers are present or not, or if one, or both, lead to βDF. It can be speculated that both of the isomers do fission, based on the work by Andreyev *et al.* [40]. The values for both the β branching and $P_{\beta DF}$ were determined by a qualitative estimate and are in good agreement with the estimated values in this thesis, which were deduced from experimental data.

Chapter 10

Conclusions

To conclude, this work has produced an updated decay scheme for ^{196}At. Two previously unseen fine structure decays have been observed, with confirmation of a third fine structure peak that was observed in a previous study. Using the limited $\alpha-\gamma$ coincidence data available, new γ transitions have been seen with multipolarities assigned. The new excited states in ^{192}Bi have tentatively been assigned spins and parities. The β branching ratio of ^{196}At has been determined with a value of 2.6(1) %. The half-lives of ^{196}Po and ^{196}At were calculated and found to be in agreement within the error of previous studies. Half-life values were also deduced for the fine structure peaks of ^{196}At. Due to the limited statistics in the weaker fine structure peaks, the error on these values tended to be much larger. The overall half-life of ^{196}At was deduced as 358(5) ms.

The βDF of ^{196}At has also been investigated at ISOLDE. It is concluded that the decay of ^{196}Po is multi-modal, with both asymmetric and symmetric mass distributions present, as shown by the triple-humped structure of the mass distribution. This triple-humped fit was further confirmed by examining the χ^2 values of the fit to determine that a single Gaussian fit was unlikely. The plot does show a mirror plane at A = 98, but this is due to the condition $m_2^* = A_f - m_1^*$ from the calibration of the fission fragments. Further investigation of these modes, and the TKE, have shown that the symmetric fission can be associated with the high TKE, and the asymmetric with low TKE. The fission fragments were determined to be ^{98}Mo for the symmetric fission, and ^{88}Sr, ^{108}Pd for the asymmetric fission by utilising the N/Z ratio that was calculated from the fissioning parent. The value of the TKE was further investigated to attempt to determine if the 'split' seen in the TKE plot was an artefact of the binning.

When using this energy as the boundary between low and high TKE, instead of the mean, it was found that the mass distribution changed. While the mass distribution for the mean value gave a mass distribution that had a clear symmetric mass and asymmetric masses at high and low TKE, the distributions at the split were more mixed in nature for the high and low TKE. However, the mean value of TKE was used in analysis. A comparison of the χ^2 values however, suggest that fitting the TKE as two Gaussians would be the more likely outcome. To rule out the TKE consisting of two separate energy distributions, or confirm, a further experiment would need to take place that recorded a larger number of statistics for analysis. In order to provide a complete study, any future experiments should attempt to record γ data. Not only would this assist in the placing of γ rays in the decay scheme, but could also allow the study of fission-γ coincidences.

Preliminary work was also conducted with ^{194}At. From this, the energies of the α decay peaks were determined to be different from those in a previous study. It is likely that the diffence in energy values could be caused by α + e summing. The number of peaks seen in this work compared to the previous study was also reduced. It was not possible, in this case, to determine if both, or only one, of the isomers is populated. Due to there being no HPGe detectors attached, with the exception of one run, no $\alpha-\gamma$ coincidences work was possible. This limited the analysis work that could be carried out. It is hoped however that a subsequent study which, although focussed on laser spectroscopy, will provide additional data so a full analysis of ^{194}At can be performed.

A preliminary βDF study was also carried out on ^{194}At. Again, due to it not being known if both, or one isomer was, fissioning, it was not possible to carry out a full study of the βDF. Therefore, although properties of the βDF were calculated, these should be treated as estimated properties. The estimated β branching and $P_{\beta DF}$ did concur with those deduced by qualitative estimation in a previous study. Based on the assumptions made in it, then it can be suggested that both of the isomers may fission. The fission of ^{194}Po was also observed to be multi-modal, with symmetric and asymmetric fission modes, associated with the high and low TKE respectively. In this case however, it can be speculated that there appeared to be a greater number of distinct fission fragment pairings produced in the asymmetric mass distribution for ^{194}Po than for ^{196}Po.

For both of these nuclides, further study needs to be carried out if the properties are to be fully understood. This has been partially carried out with the laser spectroscopy study of ^{194}At, which forms, along with this work, part of a larger

collaboration studying the properties of nuclides located in the lead region of the nuclear chart.

Appendix A

α-Decay Energy Spectra Produced After Calibration

The fitted α decay spectrum with the energy values and identities of the peaks is shown in Fig A.1. Errors are included on the peak values.

The α decay spectrum from the GPS run can be seen in Fig A.2. Marked on it are the contaminant peaks which have been identified as heavier astatine isotopes, in particular $^{197-201}$At. It can be noted however, that the energies of these astatine isotopes are similar in value to the fine structure peaks seen in the HRS spectrum. In order to confirm that they were indeed fine structure peaks, $\alpha - \gamma$ analysis was required.

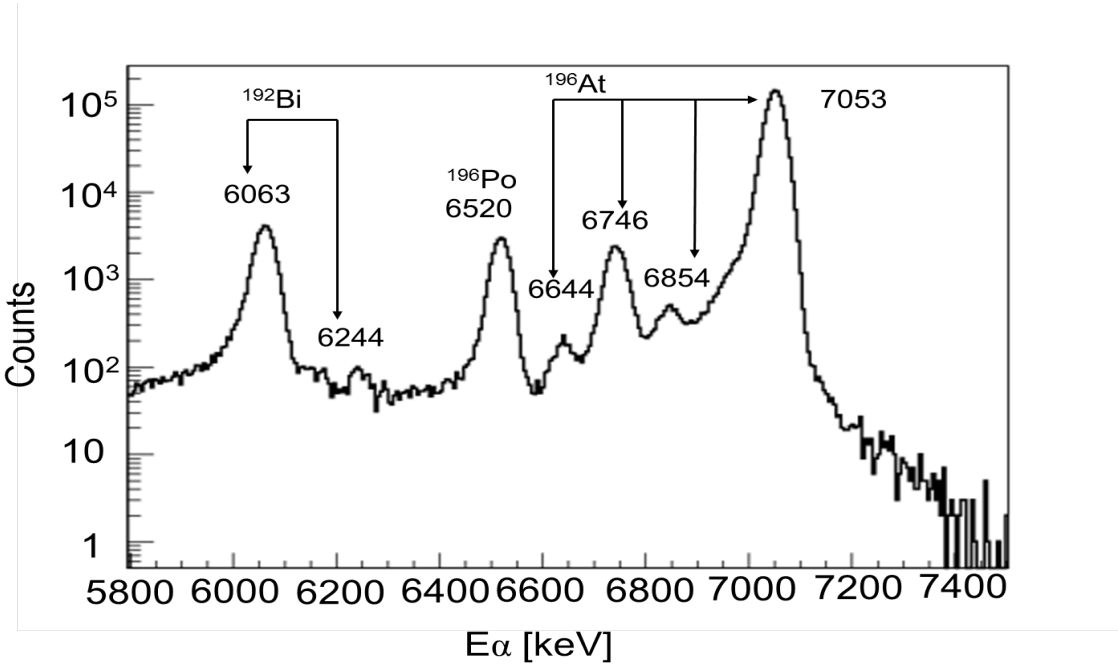

Figure A.1: Alpha decay energy spectrum of ^{196}At. Marked on the plot are the energies and identities of each of the peaks.

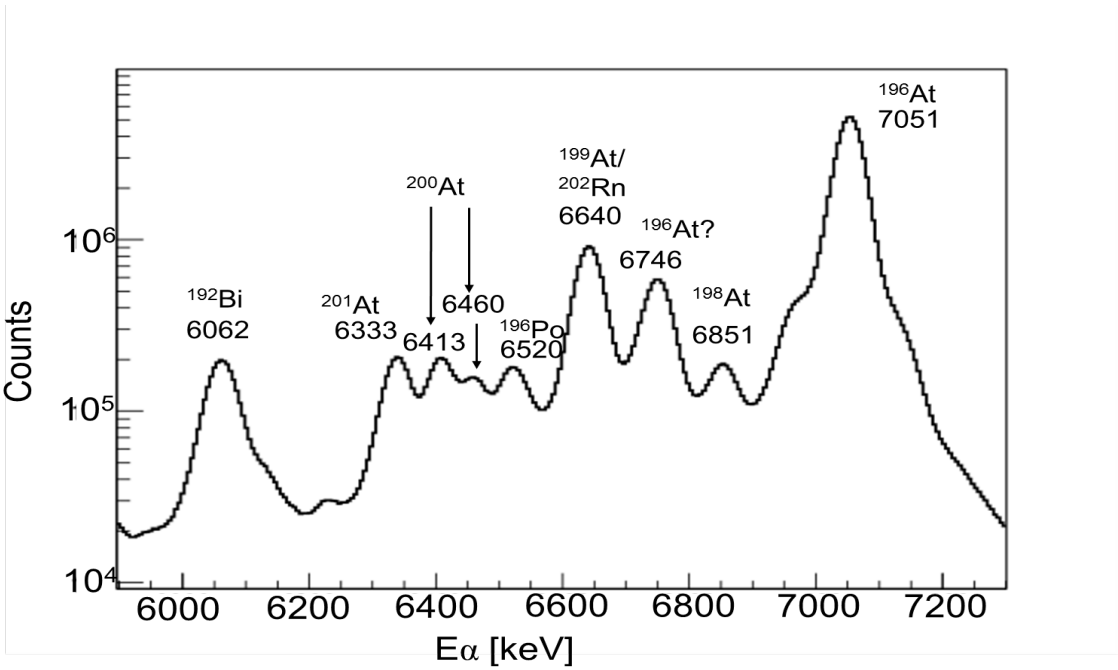

Figure A.2: α-decay energy spectrum from GPS. It can be seen that there is contamination from other astatine masses.

Appendix B

Time interval dependence on the number of $\alpha - \gamma$ coincidences seen

The two figures below are examples of how the number of $\alpha - \gamma$ events change depending on the time interval that is applied.

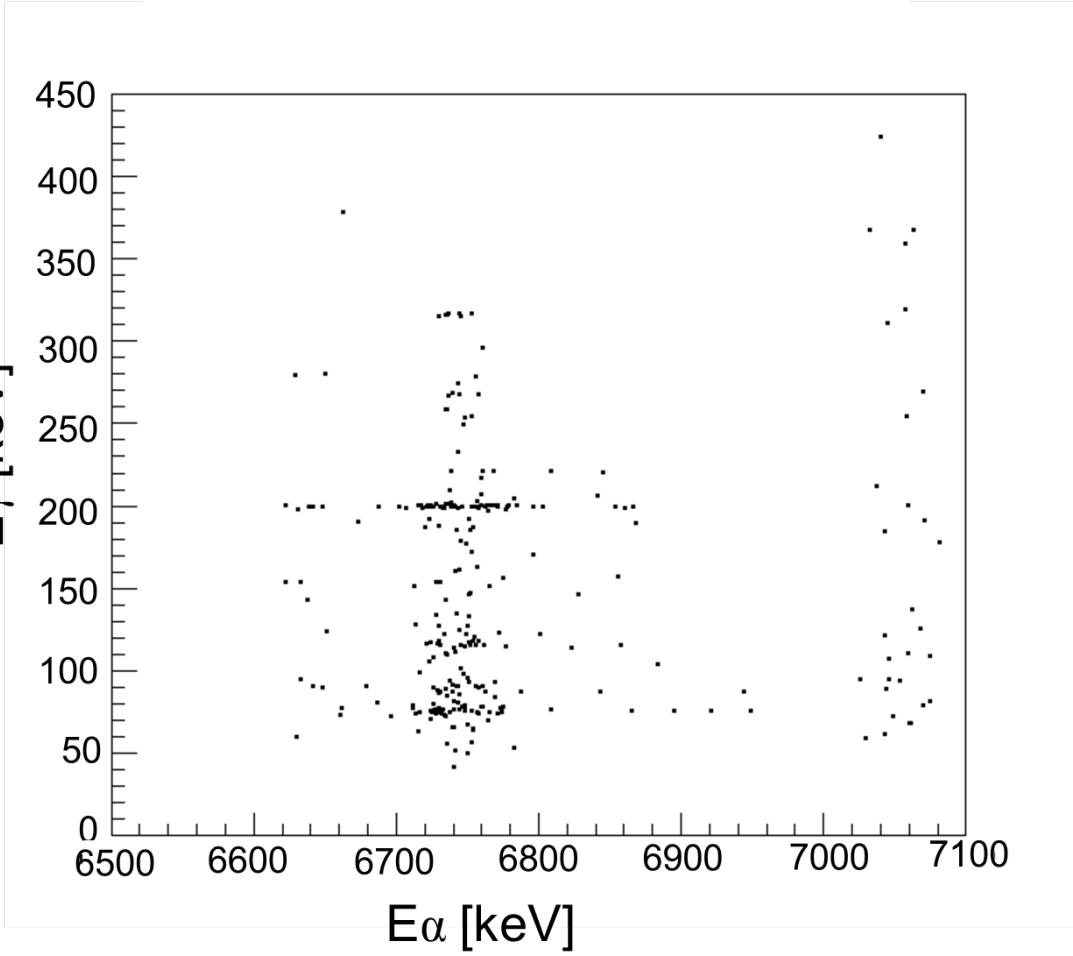

Figure B.1: $\alpha - \gamma$ coincidences with the time interval of $0 < t < 1000$ ms. In this case all events are apparent. This means that not all events seen are real, however it does ensure that no X ray counts are lost due to the unstructured time profile that they have compared to γ rays.

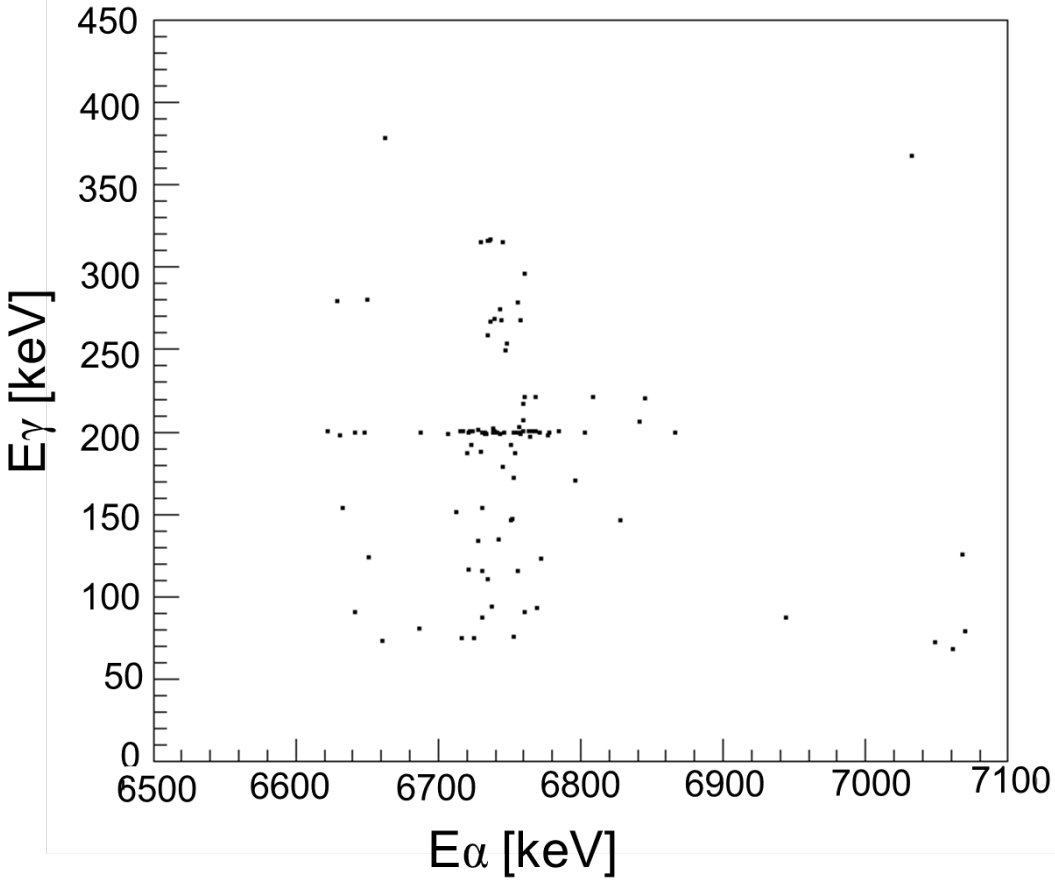

Figure B.2: $\alpha - \gamma$ coincidences with the time interval of $0 < t < 200$ ms. It is seen that not many events are present, indicating that many genuine events have been removed.

Appendix C

Reduced α width output file for ^{196}At

Table C.1: Reduced α width output of ^{196}At, where N and A are the neutron and mass number, E is the energy of the α decay peak, $T_{1/2}$ the half-life, b_{ba} and db_{ba} is the full α decay branch and error, I_{rel} and dI_{rel} is the relative intensity and error of each peak, A_{br} and dA_{br} is the relative branching of each α decay and L is the angular momentum.

N	A	E (MeV)	T1/2 (s)	b_{ba}	db_{ba}	I_{rel}	dI_{rel}	reduced width (keV)	A_{br}	dA_{br}	L
111	196	7.053	.35800	97.40	.1400	97.800	.10000	26.6168 +/- 1.966	95.2572	.16803	0
111	196	6.854	.35800	97.40	.1400	.260	.03000	.3644 +/- .051	.2532	.02922	0
111	196	6.746	.35800	97.40	.1400	1.800	.06000	6.3396 +/- .544	1.7532	.05849	0
111	196	6.644	.35800	97.40	.1400	.140	.03000	1.2031 +/- .284	.1364	.02922	0

Appendix D

Calculation of the Intensity ratio between the 116 and 316 keV γ transitions

D.1 Calculation of I_0 for the 116 keV and 316 keV γ transitions.

D.1.1 Using Si2 only

Assume the 116 keV is a M1.

$$I_0 = \frac{\mathrm{I}_{observed} \times \mathrm{I}_{conv}}{\varepsilon_\gamma}$$
$$= \frac{16 \times (1 + 6.668)}{0.08625}$$
$$= 1422.47 \quad \text{(D.1)}$$

Assume the 316 keV is E2.

$$I_0 = \frac{\mathrm{I}_{observed} \times \mathrm{I}_{conv}}{\varepsilon_\gamma}$$
$$= \frac{7 \times (1 + 0.1034)}{0.065}$$
$$= 118.82 \quad \text{(D.2)}$$

Ratio between these numbers gives, $1422.47/118.82 = \sim 12$.

D.1.2 Using both Si1 and Si2

Assumptions are the same as before and in the same order.

$$I_0 = \frac{\mathrm{I}_{observed} \times \mathrm{I}_{conv}}{\varepsilon_\gamma}$$
$$= \frac{23 \times (1 + 6.668)}{0.08625}$$
$$= 2044.8 \quad \text{(D.3)}$$

$$I_0 = \frac{\mathrm{I}_{observed} \times \mathrm{I}_{conv}}{\varepsilon_\gamma}$$
$$= \frac{9 \times (1 + 0.1034)}{0.065}$$
$$= 152.78 \quad \text{(D.4)}$$

Ratio between these numbers gives, $2044.8/152.78 = \sim 13$.

Appendix E

^{196}At βDF Fission Fragment Calculations

Below are the calculations from the low TKE asymmetric fission for the fission fragment pairings not calculated in the main text.

^{94}Zr, ^{102}Ru

$$\begin{aligned} Qfiss(0n) &= \Delta M(^{196}\text{Po}) - \Delta M(^{94}\text{Zr}) - \Delta M(^{102}\text{Ru}) \\ &= -13483 - -87270.9 - -89102.9 \\ &= 162890.8keV \\ &= 162.89MeV \end{aligned} \quad \text{(E.1)}$$

$$\begin{aligned} E^*_{max,tot} &= Q_{EC} + Q_{fiss}(0n) - TKE \\ &= 9570 + 162890.8 - 144900 \\ &= 27560.8keV \\ &= 27.56MeV \end{aligned} \quad \text{(E.2)}$$

The neutron separation values are S_n: ^{94}Zr = 8.22 MeV and ^{102}Ru = 9.22 MeV, total = 17.44 MeV.

It is therefore possible for two neutrons to be emitted leaving enough energy for any γ emission.

^{84}Kr, ^{112}Cd

$$\begin{aligned} Qfiss(0n) &= \Delta M(^{196}\text{Po}) - \Delta M(^{84}\text{Kr}) - \Delta M(^{112}\text{Cd}) \\ &= -13483 - -82439.335 - -90575.8 \\ &= 159532.14keV \\ &= 159.53MeV \end{aligned} \quad \text{(E.3)}$$

$$\begin{aligned} E^*_{max,tot} &= Q_{EC} + Q_{fiss}(0n) - TKE \\ &= 9570 + 159532.135 - 144900 \\ &= 24202.135keV \\ &= 24.2MeV \end{aligned} \quad \text{(E.4)}$$

The neutron separation values are S_n: ^{84}Kr = 10.52 MeV and ^{112}Cd = 9.39 MeV, total = 19.91 MeV.

It is therefore unlikely that two neutrons would be emitted. At most, only one would be emitted.

^{90}Sr, ^{106}Pd

$$\begin{aligned} Qfiss(0n) &= \Delta M(^{196}\text{Po}) - \Delta M(^{90}\text{Sr}) - \Delta M(^{106}\text{Pd}) \\ &= -13483 - -85948.9 - -89907.4 \\ &= 162373.3keV \\ &= 162.37MeV \end{aligned} \quad \text{(E.5)}$$

$$\begin{aligned} E^*_{max,tot} &= Q_{EC} + Q_{fiss}(0n) - TKE \\ &= 9570 + 162373.3 - 144900 \\ &= 27043.3keV \\ &= 27.04MeV \end{aligned} \quad \text{(E.6)}$$

The neutron separation values are S_n: ^{90}Sr = 7.81 MeV and ^{106}Pd = 9.56 MeV, total = 17.37 MeV.

It is therefore possible that two neutrons would be emitted in this case.

Appendix F

Mass distributions for ^{196}Po Assuming 1 Neutron and 2 Neutron Emission

The mass distributions for 1n and 2n emmission are shown in Fig. F.1 and Fig. F.2 respectively. The plots have been drawn in the same manner as those in the main text, with the total mass distribution as the black solid line, the high TKE as the blue dashed line and the low TKE as the solid green line.

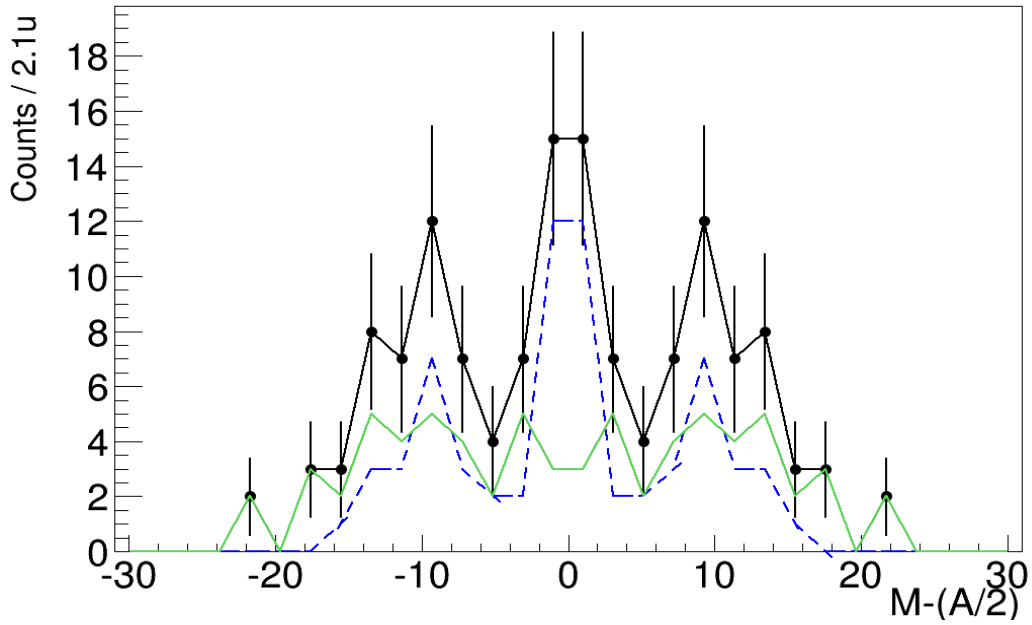

Figure F.1: 1n fission fragment mass distribution. The high TKE shows a mainly symmetric mass distribution and the low TKE an asymmetric mass distribution.

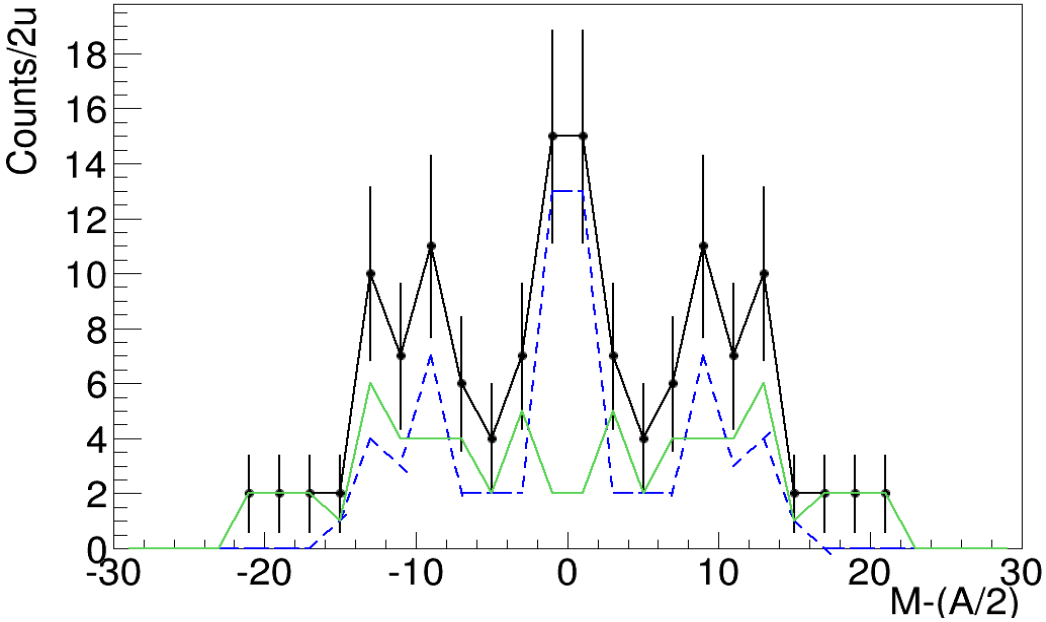

Figure F.2: 2n fission fragment mass distribution. The high TKE is a symmetric mass distribution while the low TKE is an asymmetric mass distribution.

Appendix G

^{194}At βDF Fission Fragment Calculations for the Asymmetric peaks

From Fig. G.2, the TKE distributions by mass were drawn. The dominating red line is the symmetric mass distribution. It has the highest TKE distribution. The asymmetric peaks were then drawn in their pairs to see how the TKE distributions varied. As can be seen in Fig. G.2, there is a slight difference in TKE distribution of these peaks. The pale blue and pink over-lapped lines refer to peaks 5 and 1, of masses 114 and 80 respectively. The green and dark blue over-lapped lines are peaks 2 and 4 with masses of 87 and 107 respectively. A Gaussian fit was also applied to these five main peaks as seen in Fig. G.1. The masses of the asymmetric fission fragments are 80(1), 87(1), 107(1) and 114(1) MeV. The symmetric mass fragment is at 97(1) MeV and is most likely to to be ^{97}Mo.

The fission fragments were identified as ^{80}Br, ^{113}In and ^{87}Sr, ^{107}Pd. The same calculations as in the main text were carried out for each pair.

For ^{80}Br, ^{113}In then the maximum available energy is 154.25 MeV. The neutron separation energies $S_n(^{80}\text{Br})$ and $S_n(^{113}\text{In})$ are 7.89 MeV and 9.45 MeV respectively. If two neutrons were to be emitted, then only 1.6 MeV would be left, therefore only 1 neutron at most can be emitted. For ^{87}Sr, ^{107}Pd then the maximum available energy is 162.25 MeV the neutron separtation energy $S_n(^{87}\text{Sr})$ and $S_n(^{107}\text{Pd})$ are 8.43 MeV and 6.54 MeV. Taking these values it is seen that there is enough energy available to allow for two neutron emission.

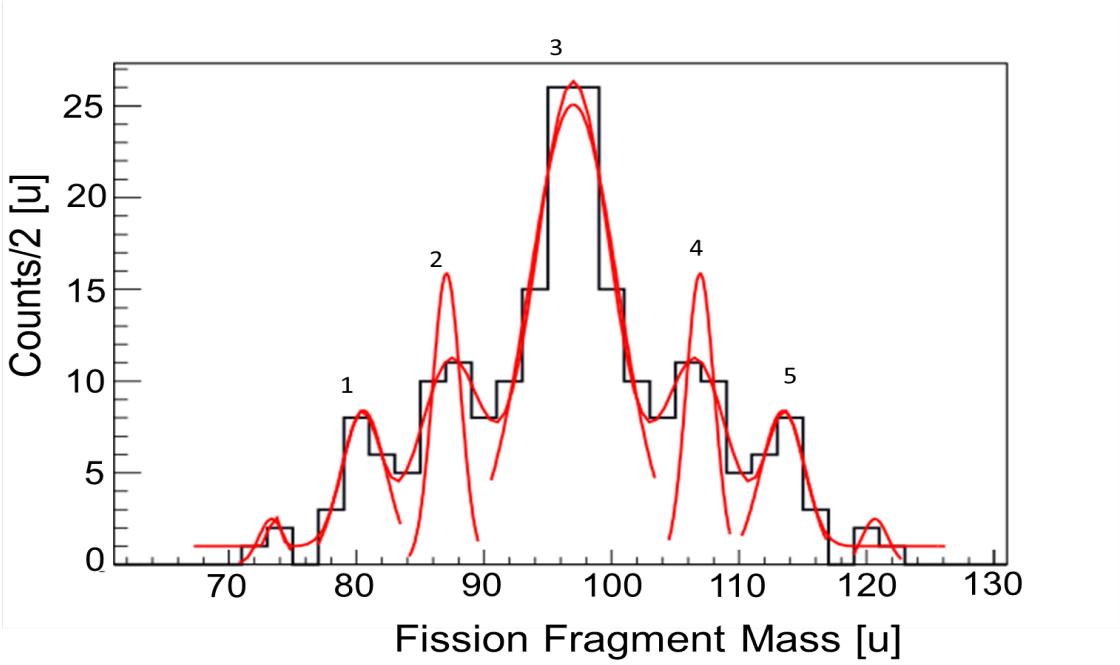

Figure G.1: Fitted mass spectrum for ^{194}Po. Marked on the plot are the peak numbers which are referred to in the text.

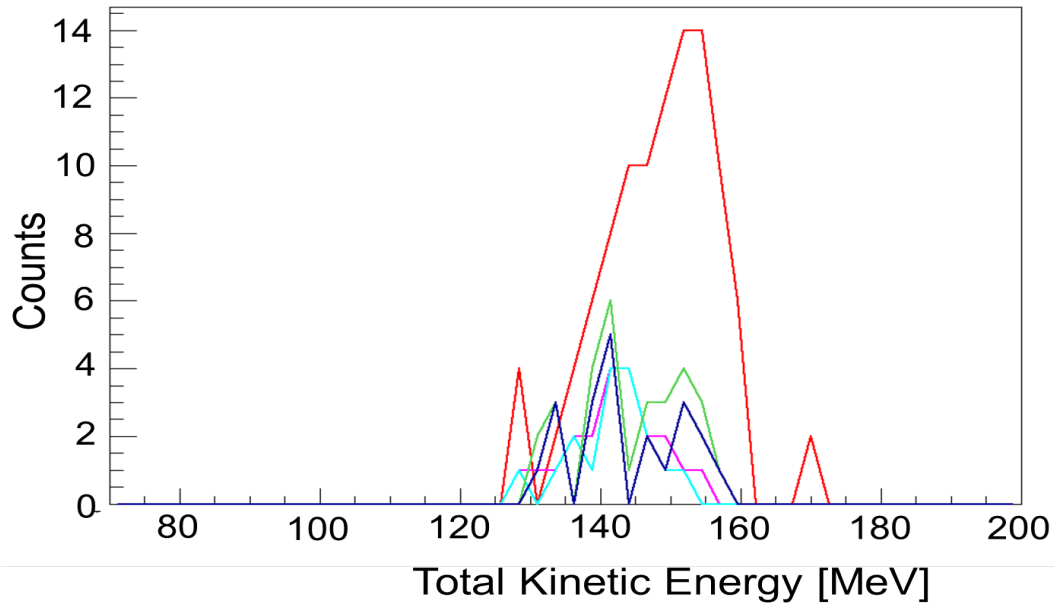

Figure G.2: TKE for each of the mass distribution peaks plotted on the same axes. The red is the symmetric TKE (peak 3), asymmetric pair one is pale blue and pink (peak 5 and 1) and asymmetric pair two is green and dark blue (peak 2 and peak 4).

References

[1] Wilbur D. Scott, Nat Chem **5**, 246 (2013), 10.1038/nchem.1580.

[2] D. R. Corson, K. R. MacKenzie, and E. Segrè, Phys. Rev. **58**, 672 (1940).

[3] http://crocker.ucdavis.edu/historical-highlights/.

[4] http://people.physics.anu.edu.au/ ecs103/chart/index.php, 2014.

[5] http://chemed.chem.purdue.edu/genchem/history/rutherford.html.

[6] J. Lilley, *Nuclear Physics: Principles and Applications* (Wiley, Chichester, 2001).

[7] A. N. Andreyev *et al.*, Phys. Rev. Lett. **110**, 242502 (2013).

[8] O. Hahn and F. Strassmann, Naturwissenschaften **27**, 11 (1939).

[9] H. G. Graetzer, American Journal of Physics **32**, 9 (1964).

[10] L. Meitner and O. R. Frisch, Nature **143**, 239 (1939).

[11] O. Hahn, Scientific American **198**, 76 .

[12] I. Noddack, Angewandte Chemie **47**, 653 (1934).

[13] E. Fermi, Nature **133**, 898 (1934).

[14] H. G. Graetzer and D. L. Anderson, *The Discovery of Nuclear Fission: A Documentary History* (Van Nostrand Reinhold Company, 450 West 33rd Street, New York, N.Y., 10001, 1971).

[15] E. G. Segrè, Physics Today **42**, 38 (1989).

[16] K. Petrzhak and G. Flerov, First publ. in Usp. Fiz. Nauk, Publ. in Zh. Eksp. Teor. Fiz. 10, 1013 (1940) **25**, 241 (1941).

[17] S. M. Polikanov *et al.*, Zh. Eksp. Theor. Fiz., [Sov. Phys. JETP, 15 (1962), 1062] **42**, 1464 (1962).

[18] V. I. Kuznetsov, N. K. Skobelev, and G. N. Flerov, Yad. Fiz. **4**, 279; [Sov. J. Nucl. Phys. **4**, (1967), 202] **66**, 279 (1966).

[19] V. I. Kuznetsov, N. K. Skobelev, and G. N. Flerov, Yad. Fiz. **5**, 271; [Sov. J. Nucl. Phys. **5**, (1967), 191] **5**, 271 (1967).

[20] K.-H. Schmidt *et al.*, Nuclear Physics A **665**, 221 (2000).

[21] K.-H. Schmidt, J. Benlliure, and A. Junghans, Nuclear Physics A **693**, 169 (2001), radioactive Nuclear Beams.

[22] L. Csige *et al.*, Phys. Rev. C **87**, 044321 (2013).

[23] J. E. Escher *et al.*, Rev. Mod. Phys **84**, 353 (2012).

[24] A. N. Andreyev, M. Huyse, and P. Van Duppen, Rev. Mod. Phys. **85**, 1541 (2013).

[25] H. Hall and D. C. Hoffman, Annual Review of Nuclear and Particle Science **42**, 147 (1992).

[26] V. I. Kuznetsov and N. K. Skobelev, Physics of Particles and Nuclei **30**, 666 (1999).

[27] Y. A. Lazarev *et al.*, EPL (Europhysics Letters) **4**, 893 (1987).

[28] J. Elseviers *et al.*, Phys. Rev. C **88**, 044321 (2013).

[29] J. Elseviers *et al.*, Phys. Rev. C **84**, 034307 (2011).

[30] A. N. Andreyev *et al.*, Phys. Rev. Lett. **105**, 252502 (2010).

[31] Moller P., Madland D. G., Sierk A. J., and Iwamoto A., Nature **409**, 785 (2001), 10.1038/35057204.

[32] T. Ichikawa, A. Iwamoto, P. Möller, and A. J. Sierk, Phys. Rev. C **86**, 024610 (2012).

[33] P. Möller and J. Randrup, 5th ASRC Workshop on Fission, 2012.

[34] F.-K. Thielemann, J. Metzinger, and H. Klapdor, Zeitschrift für Physik A Atoms and Nuclei **309**, 301 (1983).

[35] I. Panov *et al.*, Nuclear Physics A **747**, 633 (2005).

[36] S. Yashita, Ph.D. thesis, University of California, Berkeley, 1984.

[37] M. Leino, J. Aeystoe, and T. Enqvist, Acta Physica Polonica B **26**, 309 (1995).

[38] A. N. Andreyev *et al.*, Phys. Rev. C **79**, 064320 (2009).

[39] M. Nyman *et al.*, Phys. Rev. C **88**, 054320 (2013).

[40] A. N. Andreyev *et al.*, Phys. Rev. C **87**, 014317 (2013).

[41] W. Treytl and K. Valli, Nuclear Physics A **97**, 405 (1967).

[42] K. Morita *et al.*, Zeitschrift für Physik A Hadrons and Nuclei **352**, 7 (1995).

[43] T. Enqvist *et al.*, Z. Phys. A **354**, 1 (1996).

[44] Y. Pu *et al.*, Z. Phys. A **357**, 1 (1997).

[45] M. B. Smith *et al.*, J. Phys. G: Nucl. Part. Phys. **26**, 787 (2000).

[46] H. De Witte *et al.*, The European Physical Journal A - Hadrons and Nuclei **23**, 243 (2005).

[47] J. Uusitalo *et al.*, Phys. Rev. C **87**, 064304 (2013).

[48] Z. Kalaninová *et al.*, Phys. Rev. C **89**, 054312 (2014).

[49] Y. A. Lazarev *et al.*, Inst. Phys. Conf. Ser. **132**, 739 .

[50] E. Rutherford *et al.*, Proceedings of the Royal Society of London. Series A **123**, 373 (1929).

[51] C. Weizsäcker, Zeitschrift für Physik **96**, 431 (1935).

[52] H. A. Bethe and R. F. Bacher, Rev. Mod. Phys. **8**, 82 (1936).

[53] N. Bohr and J. A. Wheeler, Phys. Rev. **56**, 426 (1939).

[54] K. S. Krane, *Introductory Nuclear Physics*, 2nd edition ed. (John Wiley and Sons, New York; Chichester, 1988).

[55] K. Heyde, *Basic Ideas and Concepts in Nuclear Physics: An Introductory Approach*, 3rd edition ed. (Institute of Physics, Bristol, 2004).

[56] K. H. Schmidt, Fission: A complete laboratory, 2011.

[57] D. J. Rowe and J. L. Wood, *Fundamentals of Nuclear Models* (World Scientific Publishing Co, Singapore, 2010).

[58] V. Liberati, Ph.D. thesis, University of the West of Scotland, 2013.

[59] S. V. Nilsson and I. Ragnarsson, *Shapes and Shells in Nuclear Structure* (Cambridge University Press, Cambridge, Great Britain, 1995).

[60] Private Communication M. Reed, Surrey.

[61] A. Das and T. Ferbel, *Introduction to Nuclear and Particle Physics*, 2nd edition ed. (World Scientific, New Jersey; London, 2003).

[62] R. F. Casten, *Nuclear Structure from a Simple Perspective* (Oxford Univ. Press, New York, NY, 1990).

[63] T.-M. Goon, Ph.D. thesis, The University of Tennessee, Knoxville, 2004.

[64] R. B. F. *et al.*, *Table of Isotopes, 8th Edition*, John Wiley and Sons.

[65] G. Gamow, Zeitschrift für Physik **51**, 204 (1928).

[66] R. W. Gurney and E. U. Condon, Nature **122**, 439 (1928).

[67] J. O. Rasmussen, Phys. Rev. **113**, 1593 (1959).

[68] D. Bucurescu and N. V. Zamfir, Rom. J. Phys. **57**, 69 (2012).

[69] http://oregonstate.edu/instruct/ch374/ch418518/Chapter%207%20Alpha%20Decay-rev.pdf.

[70] W. Loveland, D. Morrissey, and G. Seaborg, *Modern Nuclear Chemistry* (Wiley, New Jersey, 2005).

[71] K. S. Krane, Atomic Data and Nuclear Data Tables **18**, 137 (1976).

[72] http://bricc.anu.edu.au/.

[73] R. Vandenbosch and J. R. Huizenga, *Nuclear Fission* (Academic Press, London, 1973).

[74] P. Möller and A. Sierk, International Journal of Mass Spectrometry **349–350**, 19 (2013), 100 years of Mass Spectrometry.

[75] V. Strutinsky, Nuclear Physics A **95**, 420 (1967).

[76] N. N. Bogoliubov, Dokl. Akad. Nauk SSSR **119**, 244 (1958).

[77] L. Ghys *et al.*, Phys. Rev. C **90**, 041301 (2014).

[78] L. Ghys, Ph.D. thesis, KU Leuven, 2015.

[79] V. E. Viola, K. Kwiatkowski, and M. Walker, Phys. Rev. C **31**, 1550 (1985).

[80] J. Terrell, Phys. Rev. **113**, 527 (1959).

[81] K.-H. Schmidt and B. Jurado, http://www.khs-erzhausen.de/, 2014.

[82] V. Pashkevich, Nuclear Physics A **169**, 275 (1971).

[83] M. G. Itkis, V. N. Okolovich, and G. N. Smirenkin, Nuclear Physics A **502**, 243 (1989).

[84] P. Möller, J. R. Nix, W. D. Myers, and W. J. Swiatecki, Atomic Data and Nuclear Data Tables **59**, 185 (1995).

[85] P. Möller *et al.*, Phys. Rev. C **91**, 024310 (2015).

[86] M. Wang *et al.*, Chinese Physics C **36**, 1603 (2012).

[87] W. D. Myers and W. J. Świątecki, Phys. Rev. C **60**, 014606 (1999).

[88] E. Kugler, Hyp. Int. **129**, 23 (2000).

[89] http://isolde.web.cern.ch, 2014.

[90] E. Kugler *et al.*, Nuclear Instruments and Methods in Physics Research Section B: Beam Interactions with Materials and Atoms **70**, 41 (1992).

[91] Y. Blumenfeld, T. Nilsson, and P. V. Duppen, Physica Scripta **2013**, 014023 (2013).

[92] U. Köster, V. Fedoseyev, and V. Mishin, Spectrochimica Acta Part B: Atomic Spectroscopy **58**, 1047 (2003), lAP-2002 INTERNATIONAL CONFERENCE ON LASER PROBING.

[93] J. Benlliure, in *Spallation Reactions in Applied and Fundamental Research* (Springer Berlin Heidelberg, Berlin, 2006), Vol. 700, pp. 191–238.

[94] P. Van Duppen, in *Isotope Separation On lIne and Post Acceleration* (Springer Berlin Heidelberg, Berlin, 2006), Vol. 700, pp. 37–77.

[95] H. L. Ravn and B. W. Allardyce, in *Treatise on Heavy-Ion Science*, edited by D. A. Bromley (Plenum Press, New York, 1989), Vol. 8, pp. 363–439.

[96] M. J. Copley and T. E. Phipps, Phys. Rev. **45**, 344 (1934).

[97] http://www.lnl.infn.it/ spes_target/ENG/ion-sources.php, 2014.

[98] R. Kirchner and E. Roeckl, Nuclear Instruments and Methods **133**, 187 (1976).

[99] S. Sundell and H. Ravn, Nuclear Instruments and Methods in Physics Research Section B: Beam Interactions with Materials and Atoms **70**, 160 (1992).

[100] A. Teigelhöfer *et al.*, Hyperfine Interactions **216**, 65 (2013).

[101] V. N. Fedosseev, Y. Kudryavtsev, and V. I. Mishin, Physica Scripta **85**, 058104 (2012).

[102] S. Rothe, Ph.D. thesis, Johannes Gutenberg-UniversitÃt, 2012.

[103] B. Marsh *et al.*, Nuclear Instruments and Methods in Physics Research Section B: Beam Interactions with Materials and Atoms **317, Part B**, 550 (2013), xVIth International Conference on ElectroMagnetic Isotope Separators and Techniques Related to their Applications, December 2–7, 2012 at Matsue, Japan.

[104] C. Geisse *et al.*, Nuclear Instruments and Methods in Physics Research Section B: Beam Interactions with Materials and Atoms **26**, 120 (1987).

[105] Borge, María José G., EPJ Web of Conferences **66**, 11005 (2014).

[106] http://www.srim.org/.

[107] http://www.ortec-online.com/Products-Solutions/RadiationDetectors/Si-Charged-Particle-Detectors-Si-for-Research.aspx, 2014.

[108] J. Elseviers, Master's thesis, IKS KU Leuven, 2009.

[109] http://www.canberra.com/products/detectors/pdf/passivated_pips_C39313a.pdf, 2014.

[110] G. Knoll, *Radiation detection and measurement* (Wiley, New York, 2000).

[111] W. Leo, *Techniques for Nuclear and Particle Physics Experiements*, 2nd edition ed. (Springer-verlag, Berlin, 1994).

[112] G. Wilson, Private Communication, 2014.

[113] Application-Note-AN40-Heavy-Ion-Spectroscopy-Silicon-Surface-Barrier-Detectors.pdf, http://www.ortec-online.com/download/, 2014.

[114] ENSDF, Evaluated Nuclear Structure Data File, http://www.nndc.bnl.govensdf/ (2013).

[115] J. O. Rasmussen, Phys. Rev. **115**, 1675 (1959).

[116] H. W. Schmitt, W. E. Kiker, and C. W. Williams, Phys. Rev. **137**, B837 (1965).

[117] E. Weissenberger *et al.*, Nucl. Instrum. Methods A **248**, 506 (1986).

[118] L. Ghys, Private Communication, 2012.

[119] J. P. Balagna, G. P. Ford, D. C. Hoffman, and J. D. Knight, Phys. Rev. Lett. **26**, 145 (1971).

[120] S. Sels, Master's thesis, KU Leuven, 2013.

[121] L. Ghys, Private Communication, 2014.

[122] P. Van Duppen *et al.*, Nucl. Phys. A **529**, 268 (1991).

[123] A. Siivola, Nuclear Physics A **101**, 129 (1967).

[124] P. V. Duppen *et al.*, Physics Letters B **154**, 354 (1985).

[125] J. Wauters *et al.*, Phys. Rev. C **47**, 1447 (1993).

[126] V. Liberati *et al.*, Phys. Rev. C **88**, 044322 (2013).

[127] S. Mukherji, Nuclear Physics A **129**, 297 (1969).

[128] C. Wagemans, *The Nuclear Fission Process* (CRC Press, Boca Raton, FL, 1991).

[129] J. D. McDonnell *et al.*, Phys. Rev. C **90**, 021302 (2014).

[130] M. Huyse *et al.*, Physics Letters B **201**, 293 (1988).

[131] J. Wauters *et al.*, Phys. Rev. C **47**, 1447 (1993).